PHOTOCATALYTIC CARBON DIOXIDE REDUCTION IN LIQUID MEDIA

A THESIS SUBMITTED TO
THE GRADUATE SCHOOL OF NATURAL AND APPLIED SCIENCES
OF
MIDDLE EAST TECHNICAL UNIVERSITY

BY

BAHAR İPEK

IN PARTIAL FULFILLMENT OF THE REQIREMENTS
FOR
THE DEGREE OF MASTER OF SCIENCE
IN
CHEMICAL ENGINEERING

APRIL 2011

Approval of the thesis:

PHOTOCATALYTIC CARBON DIOXIDE REDUCTION IN LIQUID MEDIA

submitted by **BAHAR İPEK** in partial fulfillment of the requirements for the degree of **Master of Science in Chemical Engineering Department, Middle East Technical University** by,

Prof. Dr. Canan Özgen ____________
Dean, Graduate School of **Natural and Applied Sciences**

Prof. Dr. Deniz Üner ____________
Head of Department, **Chemical Engineering**

Prof. Dr. Deniz Üner ____________
Supervisor, **Chemical Engineering Department, METU**

Examining Committee Members

Prof. Dr. Gürkan Karakaş __________________
Chemical Engineering Dept., METU

Prof. Dr. Deniz Üner __________________
Chemical Engineering Dept., METU

Prof. Dr. Ali Çulfaz __________________
Chemical Engineering Dept., METU

Prof. Dr. Saim Özkar __________________
Chemistry Department, METU

Prof. Dr. Meral Yücel __________________
Biology Department, METU

Date: 21.04.2011

I hereby declare that all information in this document has been obtained and presented in accordance with academic rules and ethical conduct. I also declare that, as required by these rules and conduct, I have fully cited and referenced all material and results that are not original to this work.

Name, Last name : Bahar İpek

Signature :

ABSTRACT

PHOTOCATALYTIC CARBON DIOXIDE REDUCTION IN LIQUID MEDIA

İpek, Bahar
M.Sc., Department of Chemical Engineering
Supervisor: Prof. Dr. Deniz Üner

April 2011, 135 pages

The aim of this study is to investigate and reveal challenges in photocatalytic CO_2 reduction tests performed in liquid media. Effect of test conditions in photocatalytic studies are often underestimated with an assumption of negligible mass transfer limitations in observed rate results. In this study, effect of mass transfer limitations in liquid phase photocatalytic tests was revealed with stirring rate and gas hold-up time experiments performed with Pt/TiO_2 and Cu/TiO_2 catalysts. In addition, apparent activation energies of 12 and 19.5 kJ/mol found with Pt/TiO_2 and Cu/TiO_2 catalysts respectively indicate diffusion limitations which favor back oxidation reactions resulting in low reduction yields.

Photocatalytic CO_2 reduction reaction is named as Artificial Photosynthesis even though present artificial system does not have sophisticated transport and membrane systems which natural systems have. Similarities and differences between artificial and natural photosynthesis are studied in order to present ideas to improve present photocatalytic rates.

Kinetic and microkinetic modeling of catalytic methanol production from CO_2 hydrogenation on Cu surfaces were performed in order to have an idea about kinetic limitations at photocatalytic systems. Calculations were performed at temperatures and pressures at which photocatalytic studies are conducted. The results indicated that water has an inhibitory effect on methanol formation rates and higher pressures could be implemented in photocatalytic systems for higher rates. Another implication drawn from degree of rate control calculations is that H formation step plays an important role underlying the importance of water splitting in CO_2 reduction reactions.

Keywords: Artificial photosynthesis, Carbon dioxide reduction

ÖZ

SIVI FAZDA FOTOKATALİTİK KARBONDİOKSİT İNDİRGENMESİ

İpek, Bahar
Yüksek Lisans, Kimya Mühendisliği Bölümü
Tez Yöneticisi: Prof. Dr. Deniz Üner

Nisan 2011, 135 sayfa

Bu çalışmanın amacı, sıvı fazda gerçekleştirilen fotokatalitik karbondioksit indirgeme testlerinde karşılaşılabilen sorunları araştırmak ve gözler önüne sermektir. Fotokataliz çalışmalarında test koşullarının sonuçlara etkisi, ortamda kütle aktarımı kısıtlamalarının olmadığı varsayımıyla sıklıkla hafife alınmaktadır. Bu çalışmada, Pt/TiO_2 ve Cu/TiO_2 katalizörleriyle gerçekleştirilen karıştırma hızı ve gazın sıvı içinde kalma süresi deneylerinin yardımıyla sıvı fazda gerçekleştirilen fotokatalitik deneylerde kütle aktarım hızının önemli etkisi gözler önüne serilmiştir. Deneylerde 12 ve 19.5 kJ/mol olarak bulunan düşük aktivasyon enerji değerleri testlerin difuzyon hızıyla sınırlandığını gösterir niteliktedir. Difuzyon hızı sınırlandırmalarının, reaksiyon veriminin düşmesine sebep olan ters reaksiyonları tetiklediği düşünülmektedir.

Doğal fotosentezin sahip olduğu gelişmiş taşıma ve zar sistemlerine sahip olmamakla birlikte fotokatalitik karbondioksit indirgenmesi Suni Fotosentez olarak adlandırılır. Doğal ve suni fotosentez arasındaki benzerlikler ve farklılıklar, güncel fotokataliz hızlarının gelistirilebilmesi amacıyla irdelenmiştir.

Karbondioksitin bakır yüzeyler üzerinde indirgenerek metanole dönüşmesinin kinetik ve mikrokinetik modellemesi, fotokatalitik sistemlerde hız belirleyen basamakların açığa çıkarılması amacıyla yapılmıştır. Hesaplamalar fotokataliz sıcaklık ve basınçlarında yapıldığında, suyun metanol üretimi hızı üzerindeki negatif, basıncın ise pozitif etkisi gözlemlenmiştir. Reaksiyon basamaklarının hıza etkisi araştırıldığında ise, karbondioksit indirgenmesinde H atomlarının ve de dolaylı olarak su ayrıştırma aşamasının önemi vurgulanmıştır.

Anahtar Kelimeler: Suni fotosentez, Karbondioksit indirgenmesi

To My Family

ACKNOWLEDGEMENTS

The author wishes to express her deepest gratitude to her supervisor Prof. Dr. Deniz Üner for her guidance, advice, insight and encouragements throughout the research and life.

The author wishes to express her appreciation to her family for their endless support and encouragements throughout life. Without their support and love, the realization of her goals would not be possible.

The author would like to express her intimate thanks to Murat Torun for his endless patience and support in every stage of the research and for always being there to share the life.

The author would like to thank former and present CACTUS research group members for their companionship and suggestions in the laboratory.

The technical assistance of Mrs. Gülten Orakçı, Mr. İsa Çağlar and the other Personnel of Chemical Engineering Workshop are gratefully acknowledged.

The author would like to thank to Prof. Dr. Ali Çulfaz and Mrs. Berna Güney for realization of XRD measurements and to Central Laboratory personnel for TEM measurements.

This study was supported by The Scientific and Technological Research Council of Turkey (TUBITAK) with research grant numbers: 107M447 and CAYDAG 106Y075.

The author would also like to acknowledge the financial support of TUBITAK BIDEB 2228 for M.S. research.

TABLE OF CONTENTS

ABSTRACT iv

ÖZ vi

DEDICATION viii

ACKNOWLEDGEMENTS ix

TABLE OF CONTENTS x

LIST OF TABLES xiii

LIST OF FIGURES xv

LIST OF SYMBOLS xviii

CHAPTERS

1. INTRODUCTION 1

2. LITERATURE SURVEY 6

    2.1 PHOTOCATALYSIS 6

2.1.1 Preventing Charge Recombination 7

2.1.2 Thermodynamic Favorability of the Reactions 8

    2.2 PHOTOSYNTHESIS 12

2.2.1 Overview 12

2.2.2 Reactions 13

2.2.2.1 Light Dependent Reactions 13

2.2.2.2 Light Independent Reactions 17

2.2.3 Transport Processes 20

2.2.4 Similarities and Differences between Photosynthesis and Artificial Photosynthesis 24

    2.3 CO_2 PHOTOREDUCTION ON TiO_2 25

2.3.1 Challenges in CO_2 Photoreduction with H_2O in Three-Phase Systems 29

2.3.1.1 Mass Transfer Considerations in Liquid Media Photocatalytic Testing 31

2.3.2 Effect of Micromixing Conditions on Reaction Rates 34

    2.4 KINETIC CONSIDERATIONS 36

2.4.1 Photocatalytic CO_2 Reduction Reaction Mechanism 36

2.4.2 Catalytic Contributions to Photocatalysis 39

2.4.3 Catalytic CO_2 Hydrogenation with Copper Based Catalysts 41

3. MATERIALS AND METHODS 44

3.1 CATALYST PREPARATION ... 44
3.1.1 Mixing Rate and Effect of Temperature Experiments ... 44
3.1.2 Photocatalytic CO_2 Reduction Experiments ... 44
3.1.2.1 First Set ... 44
3.1.2.2 Second Set ... 46
3.1.2.3 Third Set ... 47
3.1.2.4 Fourth Set ... 47
3.2 CATALYST CHARACTERIZATION ... 50
3.3 CATALYST TESTING ... 50
3.3.1 Mixing Rate and Effect of Temperature Experiments ... 50
3.3.2 Photocatalytic CO_2 Reduction Experiments ... 52
3.4 KINETIC AND MICROKINETIC MODELLING OF METHANOL FORMATION ... 53
3.4.1 Calculation of Methanol Formation Rates with the Steady State Kinetic Model Proposed by Vanden Bussche et al. ... 53
3.4.2 Calculation of Methanol Formation Rates with the Static Kinetic Model Proposed by Ovesen et al. ... 55
3.4.2.1 Calculation of Molecular Partition Functions ... 58
3.4.3 Microkinetic Modeling of CO_2 Hydrogenation using Finite Difference Method and Pseudo Steady State Approximation ... 61
3.4.3.1 Activation Energy Barrier Calculations for Each Step ... 62
3.4.3.2 Calculation of Pre-Exponentials ... 64
3.4.3.3 Finite Difference Method ... 65
3.4.3.4 Pseudo Steady State Approximation ... 66
3.4.4 Revealing Rate Determining Steps ... 67
4. RESULTS AND DISCUSSION ... 68
4.1 Cu/ TiO_2 CATALYST CHARACTERIZATION RESULTS ... 68
4.1.1 BET Surface Area Measurements ... 68
4.1.2 XRD Analysis ... 69
4.1.3 TEM Measurements ... 70
4. 2 MASS TRANSFER LIMITATION EXPERIMENTS ... 72
4.2.1 Effect of Stirring Rates ... 73
4.2.2 Effect of Gas Hold-up Time ... 75
4.2.3 Effect of Temperature ... 76
4.3 PHOTOCATALYTIC CO_2 REDUCTION ACTIVITY RESULTS ... 79

4.3.1 Photocatalytic Testing of First Set of Catalysts 80
4.3.2 Photocatalytic Testing of Second Set of Catalysts.. 82
4.3.3 Photocatalytic Testing of Third Set of Catalysts... 83
4.3.4 Photocatalytic Testing of Fourth Set of Catalysts... 84
4.3.5 Comparison of Results with Literature Results 86
4.4 KINETIC AND MICROKINETIC ANALYSIS 87
4.4.1 Catalytic Methanol Formation Rates Calculated with the Kinetic Model of Vanden Bussche et al [95]. 87
4.4.2 Catalytic Methanol Formation Rates Calculated with the Static Kinetic Model Proposed by Ovesen et al [98]. 89
4.4.3 Microkinetic Modeling of CO_2 Hydrogenation using Finite Difference Method and Pseudo Steady State Approximation 93
4.4.4 Rate Determining Step Investigation on Copper Based Catalysts 102
5. CONCLUSIONS 105
6. RECOMMENDATIONS 107
REFERENCES 108

APPENDICES

A. REDOX COMPONENTS IN PHOTOSYNTHESIS 119
A.1 TYROSINE 119
A.2 PLASTOQUINONE 120
A.3 PLASTOCYANIN 120
A.4 FERRODOXIN 121
A.5 CHLOROPHYLL A AND CHLOROPHYLL B 122
B. PHOTOCATALYTIC TEST RESULT CALCULATIONS 123
B.1 MASS TRANSFER LIMITATION EXPERIMENTS 123
B.2 PHOTOCATALYTIC CO_2 REDUCTION EXPERIMENTS 130
C. XPS MEASUREMENTS OF Cu/ TiO_2 CATALYSTS 134

LIST OF TABLES

TABLES

Table 1.1 Total Primary Energy Supply (TPES) by fuel in 2008 2

Table 2.1 Half cell reactions and their electrooxidation or reduction potentials at pH=7 vs NHE 9
Table 2.2 Overall reactions and standard Gibbs free energies normalized per mole of O_2 produced 11
Table 2.3 CO_2 photoreduction normalized rates from literature 26
Table 2.4 Estimated CO_2 photoreduction L-H parameters, Wu et al. [59] 38
Table 2.5 Estimated CO_2 photoreduction L-H parameters, Ren et al. [77]. 38
Table 2.6 Catalytic methanol synthesis results from literature at different conditions... 42

Table 3.1 GC/TCD Operation Parameters 52
Table 3.1 GC/FID Operation Parameters 53
Table 3.3 Elementary Steps in the Kinetic Model of Methanol Synthesis 56
Table 3.4 Rate constants for Cu (111) used in the kinetic model 57
Table 3.5 Thermodynamic parameters used in partition function calculations 59
Table 3.6 Elementary reaction steps used in microkinetic modelling 62
Table 3.7 Heats of chemisorptions and total bond energies for reaction species given on Cu (111) 63

Table 4.1 BET surface areas of Cu/TiO_2 catalysts 68
Table 4.2 Initial hydrogen evolution rates with changing temperature values 78
Table 4.3 Calculated rates for first set of catalysts 82
Table 4.4 Initial methanol production rates for tested catalysts 86

Table 4.5 Initial methanol formation rates (in mol/gcat/s) with F_{CO20} = 0.0135 mol/s, F_{CO0}= 0.0675 mol/s, F_{H20}= 0.189 mol/s 88
Table 4.6 Initial methanol formation rates (in mol/gcat/s) with F_{CO20} = 0.0108 mol/s, F_{CO0}= 0.0648 mol/s, F_{H20}= 0.189 mol/s, F_{H2O0}= 0.0054 mol/s 88
Table 4.7 Translational (z_t), vibrational (z_v) and rotational (z_r) partition functions for species involved in methanol synthesis mechanism 90
Table 4.8 Initial Initial methanol formation rates (mol/gcat/s) with F_{CO20} = 0.0108 mol/s, F_{CO0}= 0.0648 mol/s, F_{H20}= 0.189 mol/s and F_{H2O0}= 0.0054 mol/s 91
Table 4.9 Calculated activation energy barriers and pre exponential factors in microkinetic modeling 94
Table 4.10 Entropy and Gibbs free energy values calculated for each step of reaction 95
Table 4.11 Steady state surface concentrations and initial methanol formation rates 99
Table 4.12 Methanol formation rates (mol/g_{cat}/s) at different reaction conditions found with different kinetic models 101
Table 4.13 The degree of rate control values with respect to r_f10 found by finite difference method at t= 5.18*10^{-7} s 102
Table 4.14 The degree of rate control values with respect to r10net found by steady state assumption at X_{CO2}=0.00005 103

Table B.1 Raw data obtained from stirring rate experiments a. 900 rpm, b. 350 rpm 123
Table B.2 Raw data for effect of gas hold-up time with 0.5 wt % Pt/TiO_2 125
Table B.3 Raw data for effect of temperature experiments with 1 wt % Pt/TiO_2 127
Table B.4 Raw data for effect of temperature experiments with 1 wt % Cu/TiO_2 129
Table B.5 Raw data obtained from photocatalytic CO_2 reduction experiment performed with first set of catalysts 130
Table B.6 Raw data obtained from photocatalytic CO_2 reduction experiment performed with second set of catalysts 132
Table B.7 Raw data obtained from photocatalytic CO_2 reduction experiment performed with fourth set of catalyst 133

Table C.1 The element molar ratio of catalysts found by XPS 134

LIST OF FIGURES

FIGURES

Figure 1.1 Illustrating scheme of photocatalytic CO_2 reduction 3
Figure 1.2 Comparison of photosynthesis and photocatalytic CO_2 reduction with illustrating schemes 4

Figure 2.1 Illustrating scheme of electron/hole pair generation and realization of redox reactions 7
Figure 2.2 Schematic illustrations of band structures of semiconductors and redox potentials of the reactions 10
Figure 2.3 Z scheme electron transfer in terms of redox potentials 14
Figure 2.4 Schematic illustration of electron and proton transport processes and ATP synthesis in light dependent reactions 15
Figure 2.5 Extension of classical S state cycle of the manganese- calcium complex..... 16
Figure 2.6 The Calvin Cycle 18
Figure 2.7 Reaction sequence of carboxylation of RuBP by RubisCO 19
Figure 2.8 Conversion of 3- Phosphoglycerate to triose phosphate............................... 19
Figure 2.9 Distribution of photosynthetic complexes in thylakoid membrane and the corresponding Z scheme... 21
Figure 2.10 PS II electron transport pathways and transfer times with midpoint potentials of electron carriers 23
Figure 2.11 PS I electron transport pathways and transfer times with midpoint potentials of electron carriers 23
Figure 2.12 Schematic illustration of CO_2 purge to system... 29
Figure 2.13 Schematic illustration of mass transfer limitations in a slurry reactor 31
Figure 2.14 Schematic illustration of stagnant zones in a slurry reactor 32

Figure 2.15 Schematic illustration of water boundary layer and diffusion of reactants and products 33
Figure 2.16 Segregated and maximum mixedness flow models 35

Figure 3.1 Preparation procedure of first set of catalysts 45
Figure 3.2 Preparation procedure of second set of catalysts 46
Figure 3.3 Preparation procedure of third set of catalysts 48
Figure 3.4 Preparation procedure of fourth set of catalysts 49
Figure 3.5 Schematic illustration of the set-up 51

Figure 4.1 XRD analysis of a: TiO_2 and b: 10 wt %Cu/TiO_2 70
Figure 4.2 TEM image of 2 wt % Cu/ Degussa P25 prepared via incipient wetness method 71
Figure 4.3 TEM image of 2 wt % Cu/TiO_2 prepared via sol- gel technique 72
Figure 4.4 Effect of stirring rates on photo catalytic hydrogen evolution with 0.5 wt % Pt/TiO_2 73
Figure 4.5 Decreasing boundary layer thickness with increasing mixing rates 74
Figure 4.6 Effect of hydrogen hold-up time on photocatalytic hydrogen evolution amounts (a) normalized with respect to catalyst amount (b) not normalized with respect to catalyst amount with CH_3OH/ H_2O: 1/125 and C_{cat}: 1 g/L 75
Figure 4.7 Effect of temperature on photo catalytic hydrogen evolution with 1 wt % Pt/TiO_2 in 250 ml water and 2 ml methanol 77
Figure 4.8 Effect of temperature on photo catalytic hydrogen evolution with 1 wt % Cu/TiO_2 in 250 ml water and 2 ml methanol 77
Figure 4.9 Effect of temperature on photocatalytic hydrogen evolution and ln rate vs 1/T demonstration with Pt/ TiO_2 catalyst 79
Figure 4.10 Photocatalytic methanol production amounts of first set of catalysts with respect to time 80
Figure 4.11 Reaction rates of first set of catalysts with respect to time 81
Figure 4.12 Photocatalytic methanol production amounts of second set of catalysts with respect to time 83

Figure 4.13 Photocatalytic methanol production amounts of 3 wt % Cu/ Degussa P25 and 3 wt % Cu/ TiO_2 85
Figure 4.14 Comparison of reaction rates of first set 3 wt % Cu/Degussa P25 and fourth set 3 wt % Cu/TiO_2 85
Figure 4.15 Demonstration of calculated rates in ln rate vs 1/T scale. 92
Figure 4.16 Vacant site coverage values with respect to time at 75 bar, 523 K on a Cu based catalyst 96
Figure 4.17 CO_2 coverage values with respect to time at 75 bar, 523 K 96
Figure 4.18 CO coverage values with respect to time at 75 bar, 523 K 97
Figure 4.19 H coverage values with respect to time at 75 bar 523 K. 97
Figure 4.20 HCOO coverage values with respect to time at 75 bar, 523 K 98
Figure 4.21 Equilibrium CO_2 conversion and constant rate conversion values at 75 bar. 100

Figure 6.1 Schematic illustration of suggested reactor for CO_2 reduction 108

Figure A.1 Structural formula of tyrosine 119
Figure A.2 Structural formula of plastoquinone 120
Figure A.3 Demonstration of copper site in plastocyanine with four amino acids bound to copper molecule 120
Figure A.4 Demonstration of Fe_2S_2 ferrodoxin 121
Figure A.5 Structural formulas of Chloropyhll a and Chlorophyl b 122

Figure C.1 XPS spectra of Cu/ Degussa P25 catalysts prepared by incipient wetness method 135

LIST OF SYMBOLS

a_b	Specific gas- liquid contact area, m^2 bubbles /m^3 reactor
a_p	Specific external interface of solids, m^2 catalyst/ m^3 liquid
A	Electron acceptor
B	Rotational constant of a gas molecule, cm^{-1}
c	Speed of light, $3*10^8$ m/s
D	Electron donor
D_{ab}	Molecular diffusion coefficient, m^2/s
D_b	Binding energies of bonds broken, kJ/mol
D_f	Binding energies of bonds formed, kJ/mol
F_i	Molar flow rate of species i, mol/s
h	Planck constant, $6.63*10^{-34}$ J.s
I	Light intensity, $W.cm^{-2}$
I_A	Moment of inertia, $kg.m^2$
k	Reaction rate constant
k_B	Boltzmann constant, $1.38*10^{-23}$ J/K
k_G	Gas side mass transfer coefficient, m/ s
k_L	Liquid side mass transfer coefficient, m/ s
k_s	Liquid to solid mass transfer coefficient, m/ s
K_i	Langmuir adsorption equilibrium constants for species i, bar^{-1}
m	Molecular weight of gases, g/ mol
N_i	Moles of species i in a batch reactor, mol
Q_r	Heats of chemisorption of reactants, kJ/mol

Q_p	Heats of chemisorption of products, kJ/mol
P	Pressure, bar
T	Temperature, K
α	Power intensity of light
η	Internal efficiency factor
θi	Coverage of species i
ν	Frequency, cm^{-1}
$\chi_{rc,i}$	Degree of rate control of step i

CHAPTER 1

INTRODUCTION

Human related activities, mainly fossil fuel combustions, are responsible for 9 GT of carbon emissions/year to the atmosphere; 4 GT of which can not be removed by photosynthesis or by oceanic uptake. Carbon dioxide concentration in the atmosphere has increased from 270 ppm to 385 ppm during last 200 years, mainly due to fossil fuel combustion for power generation, public electricity and heat production [1].

Strategies implemented to prevent further increase of CO_2 emissions could be studied in three main aspects; (i) reducing produced CO_2 amount by increasing energy efficiency, (ii) storage of CO_2 by absorption or adsorption, (iii) usage of CO_2 in industry. First alternative could be accomplished by increasing energy efficiency of the existing plants or by implementing new plants with higher efficiencies. Changing primary energy source to alternative fuels like biodiesel and bioethanol, has caused debates regarding the negative effect of grain consumption in biofuel production resulting in soaring food prices. Although implementation of renewable energy resources like wind, geothermal, PVs, hydroelectric, wave, tidal and nuclear is attracting increasing attention, their utilization is still too low for energy generation (Table 1.1).

Table 1.1 Total Primary Energy Supply (TPES) by fuel in 2008 [2]

Fuels	**Fuel Shares of TPES (%)**
Oil	33.2
Coal	27
Gas	21
Combustible renewables and waste	10
Nuclear	5.8
Hydro	2.2
Other (Geothermal, solar, wind, etc.)	0.7

Storage of CO_2 could be realized by carbon capture and sequestration methods like absorption into chemical solvents like amine based solvents, or by adsorption onto solid sorbents like metal organic framework compounds. Although with innovations in material science CO_2 can be stored onto MOF 177 with an adsorption capacity of 33.5 mmol/ g [3], storing CO_2 onto sorbents could only solve the problem temporarily. New materials and systems should be implemented in order to not only store CO_2, but also convert it into valuable chemicals; like fuels.

CO_2 is used in industry in beverages, in enhanced oil recovery, as solvents in its supercritical state, in food preservation technologies; and also in carboxylic acid, organic carbonate, urea and methanol production with a total annual consumption rate of 120 MT CO_2 / year [4].

Besides catalytic and electrochemical CO_2 conversion methods, there is also photocatalytic method in which CO_2 is reduced with H_2O into variable chemicals with utilization of solar energy, in the presence of a semiconductor (Figure 1.1).

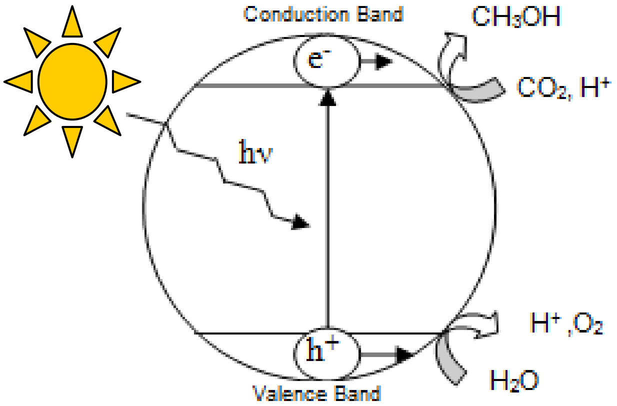

Figure 1.1 Illustrating scheme of photocatalytic CO_2 reduction

Overall reactions and possible products in photocatalytic CO_2 reduction can be seen below:

$$CO_2 + H_2O \rightarrow HCOOH + 1/2O_2$$
$$CO_2 + H_2O \rightarrow CO + H_2 + O_2$$
$$CO_2 + 2H_2O \rightarrow CH_3OH + 3/2O_2$$
$$CO_2 + 2H_2O \rightarrow CH_4 + 2O_2$$

This process is also named as 'Artificial Photosynthesis' due to its resemblance to photosynthesis with the same reactants and the same source of energy: solar energy. However, photosynthesis is a much more complex process resulting in a more complex product, $(CH_2O)_6$.

Another resemblance between photosynthesis and photocatalytic CO_2 reduction is the reaction steps; in both processes, firstly H_2O is oxidized to O_2 with electromagnetic irradiation and CO_2 is reduced with produced H^+s (in form of NAPDH in photosynthesis) (Figure 1.2).

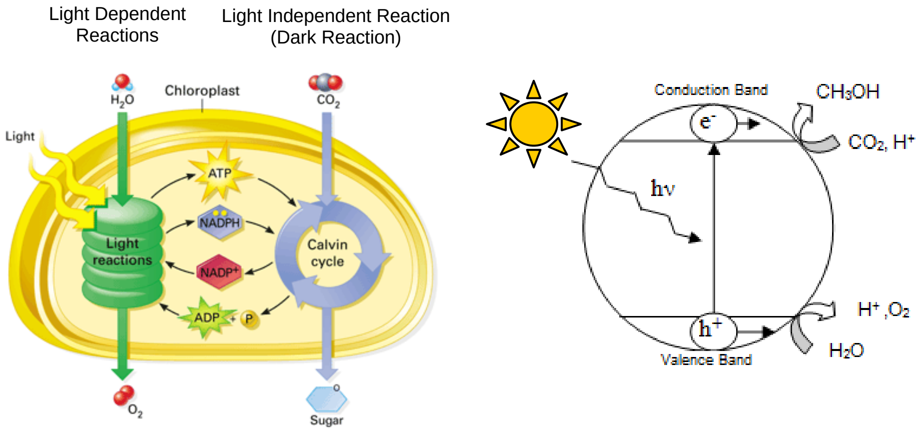

Figure 1.2 Comparison of photosynthesis and photocatalytic CO_2 reduction with illustrating schemes [5]

In literature survey chapter, a section with the title *Photosynthesis* is given to elucidate reaction and transport mechanisms in photosynthesis, compared with those in photocatalysis with the aim of revealing the position of photocatalytic CO_2 reduction with respect to photosynthesis and in which aspects it could be amended.

Photocatalysis offers an alternative to conventional catalysis with the ability of converting solar energy into chemical energy. However, reported photocatalytic reaction rates so far are not favorable for the commercialization of the process.

The studies conducted on photocatalytic CO_2 reduction focus on material development for efficient visible light utilization or enhanced charge kinetics on surface and process development such as utilization of hole scavengers. A broad overview of mentioned developments is given in literature survey section. In addition, photocatalytic rates are not reported in standardized reaction systems. Different reactors with different reaction media, mixing intensities, catalyst concentrations and liquid volumes could result in improper comparison of activity results with different bases. Yet, reported activity results do not seem to be improved in order of magnitudes.

Similarity of the reported results necessitates questioning of transport processes occurring in a photocatalytic reactor. Liquid phase photocatalytic studies draw special attention due to probable mass transfer limitations in observed rates arising from interfacial transport processes. Therefore, investigation of transport phenomena in photocatalytic systems is an objective of this study.

Presence of dark steps in photocatalytic CO_2 reduction is suggested in this study with the evidences from literature. Similarity in mechanisms of catalytic CO_2 hydrogenation and CO_2 reduction reactions were assumed because of the utilization of copper based catalysts in both reactions. Therefore, kinetic and microkinetic analysis of catalytic CO_2 hydrogenation on copper based catalysts were performed in order to get a hint about rate limiting steps in photocatalytic CO_2 reduction reaction.

The objective of this study is to elucidate the role of operational parameters and to understand chemical details of photocatalytic carbon dioxide reduction reaction in order to improve present photocatalytic systems and carbon dioxide reduction yields.

CHAPTER 2

LITERATURE SURVEY

2.1 PHOTOCATALYSIS

Harnessing solar energy in chemical bonds is viable by photocatalysis. In photocatalysis, electrons and holes are generated upon electromagnetic irradiation provided that the energy of the irradiated light is equal or greater than the band gap energy of the utilized semiconductor. Once electrons and holes are created, they can experience either migration to the surface and being trapped at the trap sites or alternatively recombine at the surface or in the bulk volume of the semiconductor (Figure 2.1) [6]. After charge carriers; electrons and holes, are trapped at the trap centers, they reduce/oxidize surface adsorbed species if surface adsorbates possess appropriate redox potentials for a thermodynamically allowed reaction.

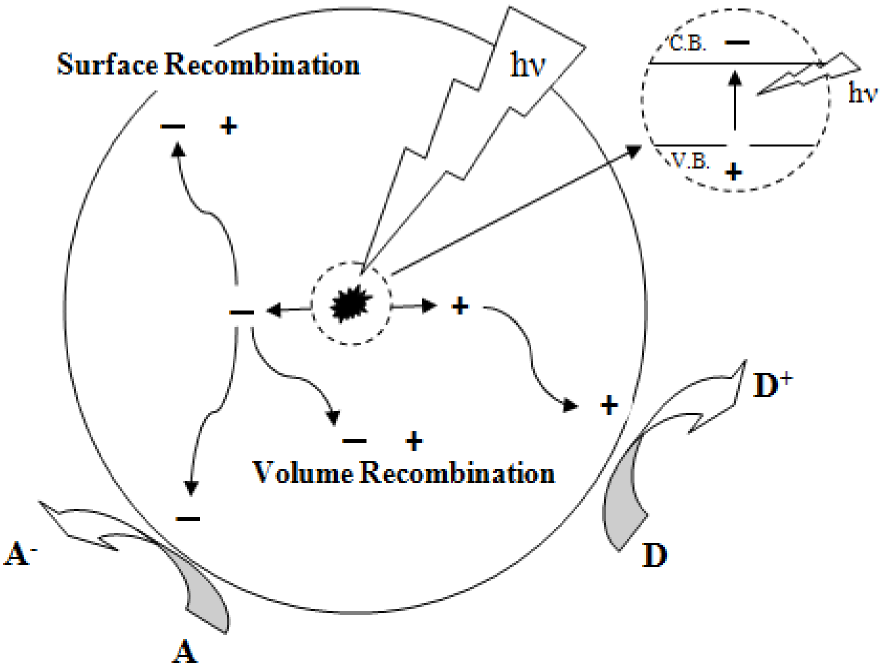

Figure 2.1 Illustrating scheme of electron/hole pair generation and realization of redox reactions

Semiconductors, having a band gap, ensure a life-time for generated electrons and holes; however, this lifetime is limited to 10^{-7} s, which is the characteristic time of recombination (for bare TiO_2) [7]. That is to say, charge carriers; electrons and holes, should be trapped at the trap sites for efficient utilization in redox reactions. Anpo et al., found a highly excited electronic state of TiO_2 catalyst; $(Ti^{+3}\ O^{-})^{*}$, with Electron Spin Resonance (ESR) upon irradiation which labels Ti^{+3} as trapped electron centers and O^{-} as trapped hole centers [8-10].

2.1.1 Preventing Charge Recombination

Metal addition to semiconductors is widely used in photocatalytic studies, which are reported to decrease the rate of recombination and increase photocatalytic yields [11-20]. When metals are brought into contact with semiconductors, electrons populate on metals if Fermi level of the metal is lower than the conduction band of the semiconductor. Hence, metals act like ‘charge carrier traps’, increasing lifetime of electron hole pairs with charge separation effect, known as ‘Schottky Barrier Effect’. Although metal loadings are generally reported to increase the photocatalytic activity, an optimum loading value is reported, suggesting that higher loadings decrease photoexcitation capacity of the semiconductor by masking the surface [15, 18].

Charge separation effect of metals was supported by giving ESR data [16, 21, 22]. Anpo et al. and Sa et al. investigated Ti^{+3} signals with ESR and observed that while Ti^{+3} signals increase with increasing UV irradiation time on TiO_2, they show negligible increase with metal added TiO_2. They attributed those results to localization of electrons at Ti^{+3} sites when there is no metal (only TiO_2), and transfer of photogenerated electrons from TiO_2 to metal with Pt/TiO_2 or Ag/TiO_2, resulting in charge separation with good efficiency.

Another modification that can hinder recombination of generated electrons and holes is formation of solid-solid interfaces in composite photocatalysts having different band gap energies. To illustrate; commercial TiO_2 catalysts; Degussa P-25, is composed of anatase and rutile crystal phases of TiO_2, having band gap energies of 3.2 eV and 3.0 eV respectively. Mixed phase TiO_2, tends to exhibit higher photocatalytic activity than pure phases, because it allows transfer of the photogenerated electron from rutile to anatase, resulting in charge separation [7, 23]. Electron transfer from a smaller band gap to a larger band gap crystal is explained by additional trapping sites of anatase which have energies 0.8 eV less than conduction band of anatase [23, 24].

2.1.2 Thermodynamic Favorability of the Reactions

In photocatalysis, surface adsorbed species should have appropriate redox potentials with respect to flat band positions of the semiconductor for thermodynamic favorability of the reactions. In other words, semiconductors should have conduction bands located at a more negative potential than the reduction potential of CO_2 to hydrocarbons, and valence bands located at a more positive potential than the oxidation potential of H_2O. In Table 2.1 oxidation and reduction reactions taking place in photocatalytic CO_2 reduction are listed with their electrooxidation or reductionpotentials at pH=7, vs NHE.

Table 2.1 Half cell reactions and their electrooxidation or reduction-potentials at pH=7 vs NHE

Reactions	**E^0 (V)**
$2H_2O + 4h^+ \rightarrow O_2 + 4H^+$	+ 0.82
$CO_2 + 2H^+ + 2e^- \rightarrow HCOOH$	- 0.61
$CO_2 + 2H^+ + 2e^- \rightarrow CO+H_2O$	-0.52
$CO_2 + 4H^+ + 4e^- \rightarrow HCHO+H_2O$	-0.48
$CO_2 + 6H^+ + 6e^- \rightarrow CH_3OH+H_2O$	-0.38
$CO_2 + 8H^+ + 8e^- \rightarrow CH_4+2H_2O$	-0.24

In Figure 2.2, flat band positions of the semiconductors used in photocatalytic CO_2 reduction reactions and also redox potentials of the reactions are given.

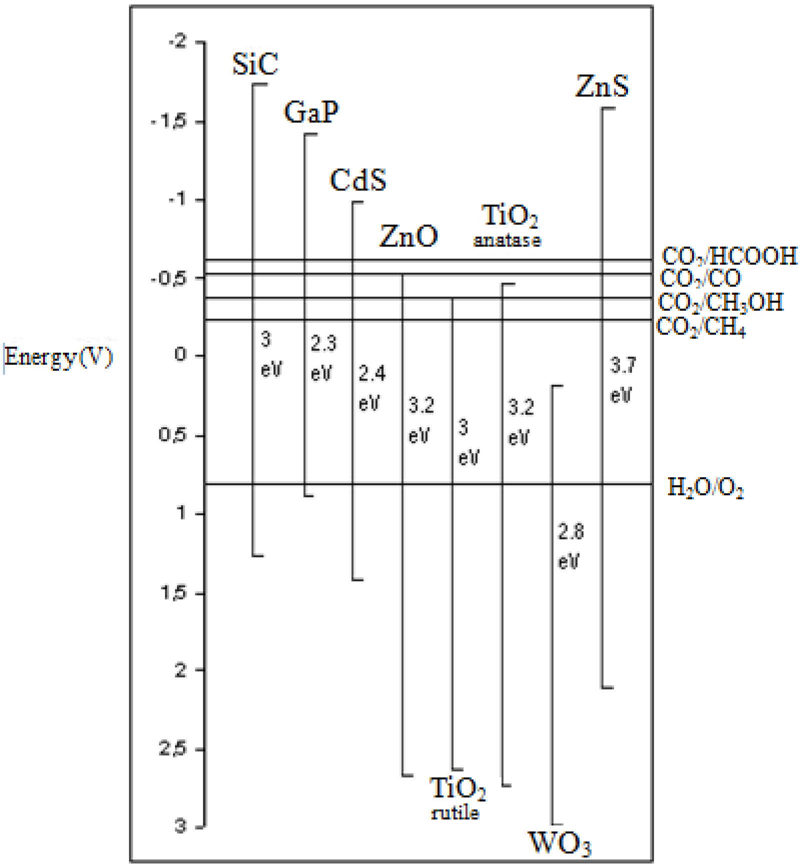

Figure 2.2 Schematic illustrations of band structures of semiconductors and redox potentials of the reactions (eV vs NHE at pH 7) [43]

In literature, the most commonly observed reduction products are CH_4 and CH_3OH, indicating favorability of multi-electron transfer processes. That indication becomes reasonable when standard Gibbs free energies of reactions are calculated per mole of O_2 produced (Table 2.2).

Table 2.2 Overall reactions and standard Gibbs free energies normalized per mole of O_2 produced

Reactions	**ΔG^0 (kJ/mol O_2)**
$H_2O_{(g)} \rightarrow 1/2O_{2(g)} + H_{2(g)}$	457.2
$CO_{2(g)} + H_2O_{(g)} \rightarrow HCOOH_{(l)} + 1/2O_{2(g)}$	523.2
$CO_{2(g)} + H_2O_{(g)} \rightarrow CO_{(g)} + H_{2(g)} + O_{2(g)}$	485.8
$CO_{2(g)} + 2H_2O_{(g)} \rightarrow CH_3OH_{(g)} + 3/2O_{2(g)}$	459.7
$CO_{2(g)} + 2H_2O_{(g)} \rightarrow CH_{4(g)} + 2O_{2(g)}$	400.5

In order to provide thermodynamic favorability, large band gap semiconductors are mostly utilized in photocatalytic CO_2 reduction reactions. It is stated that as band gap energies of the semiconductors increase, both oxidizing and reducing power of photocatalysts increase [25]. However, one disadvantage of utilization of large band gap semiconductors is that, they can be activated only under UV illumination; if their band gap energies are larger than 3 eV, according to Equation (1).

$$\text{Band gap energy (eV)} = 1240 / \lambda \text{ (nm)} \qquad (1)$$

Visible light utilization is a goal of present photocatalytic studies. There are modification studies going on for effective sunlight utilization like particle size modification, dye sensitization [26], and anion doping [27].

Chemical stability, non-toxicity and low cost render TiO_2 most commonly preferred semiconductor in photocatalytic studies. Ideally, a semiconductor photocatalyst should be chemically and biologically inert, photocatalytically stable, easy to produce and to use and efficiently activated by sunlight [7]. Therefore, TiO_2 can be considered as an ideal photocatalyst except that it cannot absorb visible light.

TiO_2 is commonly used in photocatalysis either doped with metals or with support materials like MCM-41, MCM-48 [14], porous silica thin films [28], SBA-15 [20, 25], and zeolites [30]. Support materials are reported to increase surface area and also increase selectivity of products upon alteration of Ti coordination [14].

In this section, recent developments in photocatalysis and photocatalytic CO_2 reduction studies were given with an emphasis on charge recombination.

2.2 PHOTOSYNTHESIS

2.2.1 Overview

Photosynthesis is the world's most abundant process with an approximate carbon turnover number of 300- 500 billion tons of CO_2 per year. In this vital process, green plants, algae and photosynthetic bacteria are converting CO_2 with water into carbohydrates and oxygen (in oxygenic photosynthesis), both of which are essential for sustaining life on earth. Oxygenic photosynthesis is believed to be started 2.5 billion years ago by the ancestors of cyano bacteria. In this remarkable process, energy need for converting stable compounds (CO_2 and H_2O) into comparably less stable arranged molecules ($(CH_2O)_n$ and O_2) is supplied from solar energy in which highly sophisticated protein complexes embedded in an internal chloroplast membrane (called thylakoid membrane) are major players.

$$6CO_2 + 12\ H_2O + Light\ Energy \rightarrow C_6H_{12}O_6 + 6O_2 + 6H_2O$$

$$\Delta G^0 = 2870\ \text{kJ /mol}\ C_6H_{12}O_6$$

Harnessing solar energy into chemical bonds in this process is achieved by light absorption and sequential electron and proton transport processes in which a great deal of number of light harvesting pigments, protein complexes and intermediate charge carriers are involved. CO_2 is being reduced with the indirect products of water oxidation; supplying required energy in the form of redox free energy (from NADPH) and high energy Pi bonds (from ATP).

Overall process can be shown as below where D: electron donor, A: electron acceptor and T: energy trap [31].

$D^+ \cdot T \cdot A + \frac{1}{2}H_2O \rightarrow D \cdot T \cdot A + \frac{1}{4}O_2 + H^+$ →*Water oxidation*

$D^+ \cdot T \cdot A^- + \frac{1}{2}NADP^+ + H^+ \rightarrow D^+ \cdot T \cdot A + \frac{1}{2}NADPH + \frac{1}{2}H^+$

→*$NADP^+$ reduction*

$D^+ \cdot T \cdot A^- + ADP + P_i \rightarrow D \cdot T \cdot A + ATP$ → *Cyclic Photophosphorylation*

$CO_2 + 2\ NADPH + 3\ ATP \rightarrow (CH_2O) + 2NADP^+ + 3\ ADP + 3P_i$

→*CO_2 reduction*

2.2.2 Reactions

Photosynthesis includes a series of photophysical, photochemical and chemical reactions realized by highly sophisticated protein complexes, energy carriers and enzymes. With the all complexity of their mechanisms, reactions involved in photosynthesis are mainly divided into two stages: (i) light dependent reactions including water oxidation and chemical energy generation through electron and proton transport and (ii) light independent reactions including CO_2 fixation, reduction and regeneration of ribulose 1,5 biphosphate (Calvin Cycle).

2.2.2.1 Light Dependent Reactions

The light dependent reactions occur in a complex membrane system (thylakoid membrane) via electron transfer through light induced generation of cation- anion radical pairs and intermediate charge carriers such as plastoquinone, plastocyanin and ferrodoxin. Light dependent reactions in green plants follow a Z scheme which was first proposed by Hill et al. (Figure 2.3). In this scheme, light energy is absorbed by light harvesting molecules and funneled to two special reaction center molecules; P680 and P700 which are acting as major electron donors in PS II and PSI respectively. Electron transport from PSII to PS I is realized by intermediate charge carriers (Appendix A) and electron need of P680$^+$ (strong oxidant with $E^0 = 1.1$ eV) in PSII is compensated from water molecules (water oxidation).

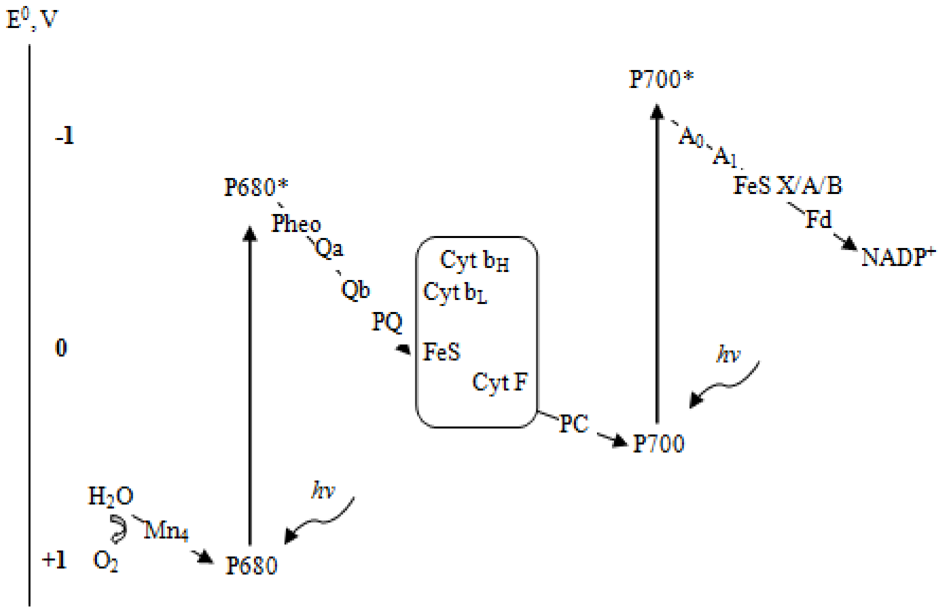

Figure 2.3 Z scheme electron transfer in terms of redox potentials

Electron transport through thylakoid membrane and water oxidation reactions results in a proton concentration gradient across the thylakoid membrane. Energy created by proton electrochemical potential resulting from this proton gradient is used by ATP synthase to produce ATP from ADP and Pi. The net reaction in light dependent reaction system is the electron transport form a water molecule to a NADP$^+$ molecule with the production of ATP molecules (Figure 2.4).

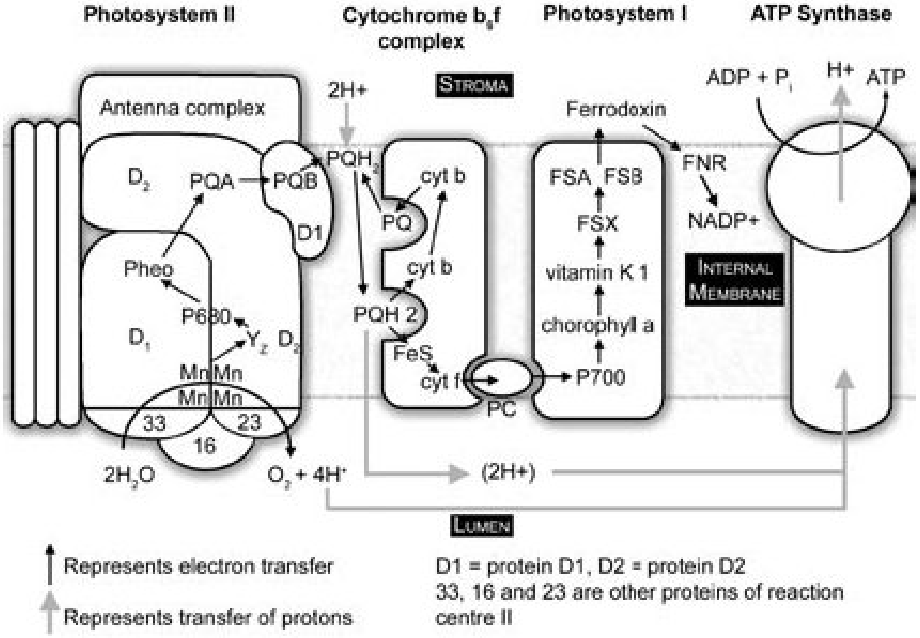

Figure 2.4 Schematic illustration of electron and proton transport processes and ATP synthesis in light dependent reactions [32]

In this complex electron transport system, PS II alone is composed of more than 15 polypeptides and nine different redox components including chlorophylla and b, pheophytin, plastoquinone.

Photosystem II is the only protein complex with the capability of oxidizing water into O_2 and protons. In PS II, water is oxidized with an Oxygen Evolving Complex whose components are believed to be in the form of $Mn_4O_xCaCl_y$ [33]. This inorganic core oxidizes two water molecules in Kok cycle, comprised of five oxidation states (S states) of PSII donor site. In this model, oxygen formation requires successive four light flashes for four-electron and four-proton release. Recently, presence of an intermediate S_4’ state and kinetics of completion of final oxidation cycle responsible for O- O bond formation was revealed with time resolved X ray study of Haumann et al. (Figure 2.5) [34].

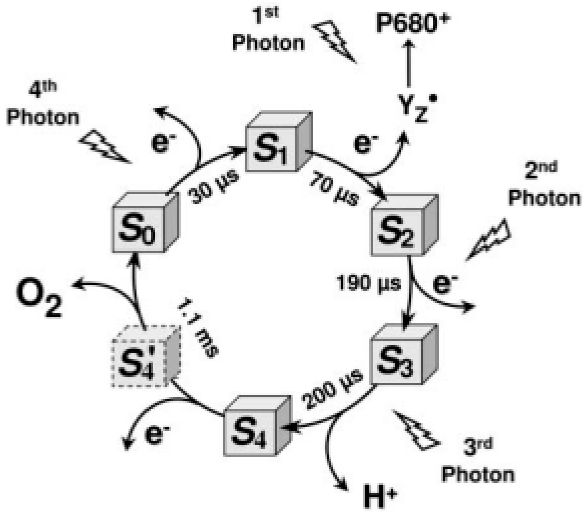

Figure 2.5 Extension of classical S state cycle of the manganese- calcium complex [34]

This high energy requiring water oxidation reaction with four- proton, four- electron extraction and an oxygen- oxygen bond formation (with a standard free energy requirement of 312 kJ/mol of O_2) necessitates the regeneration of the oxygen evolving complex at every half an hour in order to repair the damage caused by the oxygen production [35].

In electron transfer from the oxygen evolving complex (OEC) to $P680^+$ molecule, tyrosine (Y_z*) acts as intermediate electron carrier. Protons evolved from OEC are deposited in lumen phase contributing proton concentration gradient (ΔpH) mentioned in ATP synthesis part. Excited electron upon light absorption is transferred to the cytochrome b6f complex through a pheophytin, a thightly bound phylloquinone (Q_A) and a mobile phylloquinone (Q_B). Subsequently reduced phylloquinol (PQH_2) (reduced with electrons from P680* and two protons from stromal phase) releases two additional protons into lumen phase as it binds to cyctochrome b6f complex after diffusion through thylakoid membrane. Electron transfers from cyctochrome b6f complex to PS I (through lumen phase) and from PS I to $NADP^+$ molecule (through stromal phase) is achieved by plastocyanin and ferrodoxin respectively. ATP synthesis reaction in light dependent reactions is driven by the proton electrochemical and charge potential across the membrane resulted from proton concentration difference and charge separation during illumination respectively.

Produced NADPH and ATP molecules as a result of electron and proton transport in light dependent reactions are used as energy and proton sources in carbon dioxide reduction reactions in Calvin Cycle.

2.2.2.2 Light Independent Reactions

Light independent reactions take place in outer space of thylakoid membrane which is also known as stromal phase. CO_2 enters the leaf structure through small perforations called stomata and diffuses into stromal phase in the chloroplast where it is being reduced with reactions in series that are catalyzed by more than ten enzymes. Driving force for the reduction reaction is supplied from NADPH and ATP molecules; hence, the *'catalytic'* reaction sequence does not require light as an energy source and called as light independent reactions. However, recent findings indicate light activation of enzymes due to regulatory processes (reductive pentose phosphate).

Melvin Calvin and his collaborators were the first to resolve the photosynthetic CO_2 reduction mechanism with studies involving radioactively labeled CO_2. The Calvin Cycle, also known as reductive pentose phosphate pathway consists of three sections:

1. CO_2 fixation by carboxylation of rubilose 1,5- bisphosphate to two 3-phosphoglycerate molecules,
2. Reduction of 3-phosphoglycerate to triose phosphate, and
3. Regeneration of rubilose 1,5- bisphosphate from triose phosphate molecules (Figure 2.6).

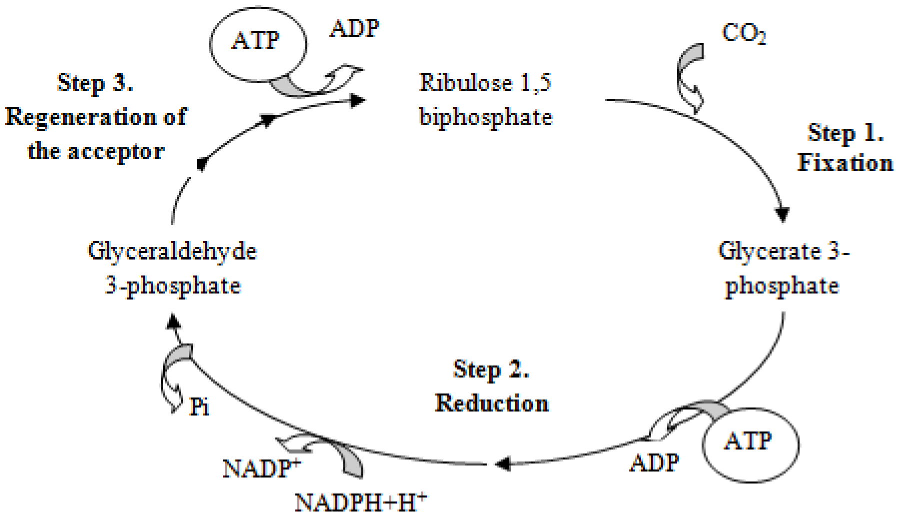

Figure 2.6 The Calvin Cycle

The key reaction in photosynthetic CO_2 reduction is the fixation of a CO_2 molecule to rubilose 1,5- bisphosphate to two phosphoglycerate molecules with a standard free energy of -35 kJ/mol indicating its irreversibility. This reaction is catalyzed with the Ribulose biphosphate Carboxylase/Oxygenase (RubisCO) enzyme which is one of largest enzymes in nature with its 8 large, 8 small subunits (with molecular weights changing from 12 to 58 kDa). This enzyme also catalyzes a side reaction, oxygenation, to give a 3-phospho glycerate and a 2-phosphoglycolate instead of two 3- phosphoglycerates for CO_2 fixation. Although oxygenation occurs with a ratio of 1:4 to 1:2 (oxygenation:carboxylation), oxygenation ratio decreases as CO_2 concentration in the atmosphere is increased. This regulatory measure of photosynthesis worths appreciation.

In carboxylation reaction catalyzed by RubisCO, rubilose 1,5- bisphosphate (RuBP) accepts CO_2 to form a keto intermediate after keto-enol isomerization (Figure 2.7).

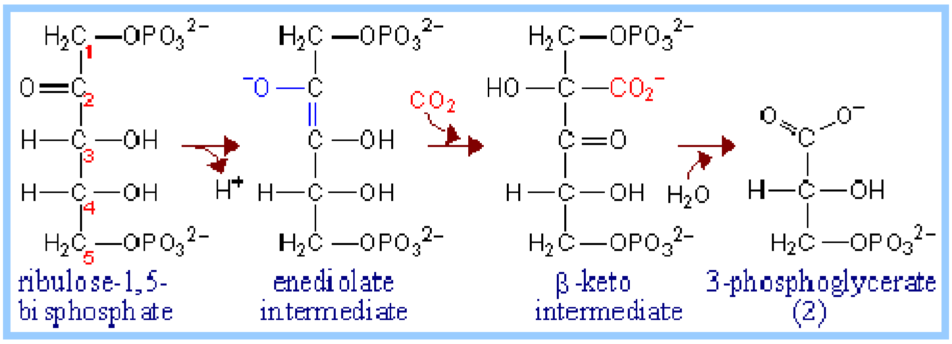

Figure 2.7 Reaction sequence of carboxylation of RuBP by RubisCO [36]

For the synthesis of glyceraldehydes 3- phosphates, firstly 3-phosphoglyerates are phospholyrated to 1,3- bisphosphoglycerate with phosphoglycerate kinase enzyme. Afterwards, 1,3- biphosphoglycerate is reduced with NADPH to glyceraldehydes 3- phosphate with glyceraldehydes phosphate dehydrogenase enzyme. Redox potential difference between the aldehyde and carboxylate is overcome with the consumption of ATP (Figure 2.8).

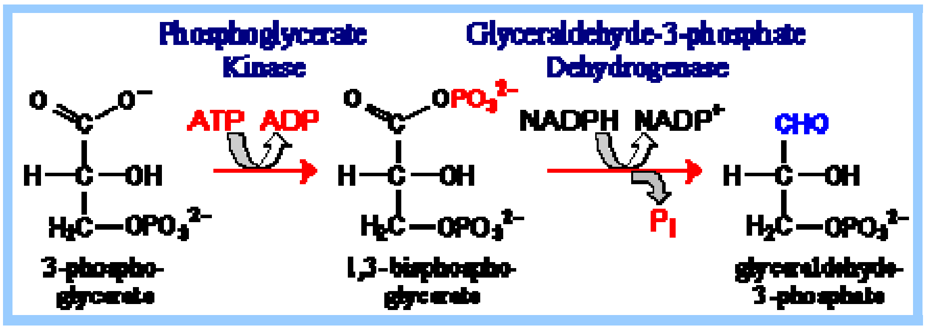

Figure 2.8 Conversion of 3- Phosphoglycerate to triose phosphate [36]

After production of glyceraldehyde 3- phosphates, out of six aldehydes produced by fixation of three CO_2 molecules, five of them are used in regeneration of three RuBP molecules together with ATP consumption.

Remaining one molecule of glyceraldehyde 3- phosphate is transported into the cytosol for utilization in glucose synthesis.

2.2.3 Transport Processes

The vesicular thylakoid membrane structure defines a closed space separating outside water phase (stromal phase) and inside water phase (lumen phase). CO_2 fixation reactions occur in the stromal phase while majority of light dependent reactions are realized in the complex membrane system with embedded protein complexes and intermediate charge carriers.

As mentioned in light dependent reactions, electron and proton transport processes through protein complexes and intermediate charge carriers like plastoquinone, plastocynanin and ferrodoxin molecules play an important role in controlling photosynthetic rates. Within a protein complex such as PSII or cyctochrome bf complex, electron transfer and pathway is controlled by polypeptide chains of the protein. However between protein complexes, electron transfer via electron carriers is controlled by distance and free energy. Below, electron and proton transport processes taken place in light dependent reactions is illustrated with particle sizes of protein complexes given by Ke et al. [37].

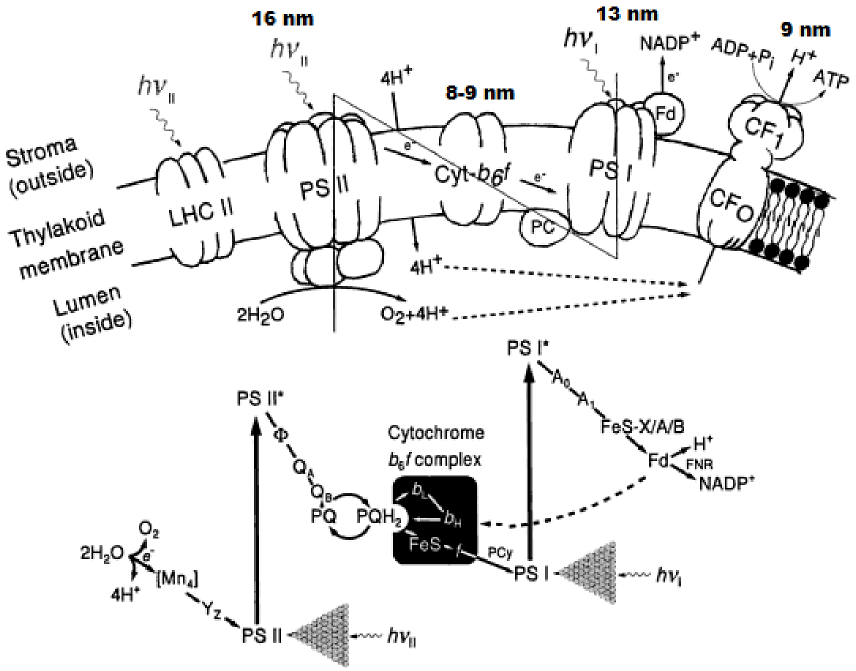

Figure 2.9 Distribution of photosynthetic complexes in thylakoid membrane and the corresponding Z scheme [37]

Presence of the membrane affects reaction rates in an aspect that it limits electron and proton transport to two dimensions which increases the random encounters. Furthermore, electron transport reactions and special structure and orientation of the membrane and protein complexes contribute to a proton electrochemical potential difference which drives ATP synthesis reaction; i.e., plays a significant role in energy supply of photosynthesis. The proton electrochemical potential difference across the membrane is created by two main contributions; i. proton concentration gradient (pH difference), and ii. electric potential difference.

The processes contributing *proton concentration difference (ΔpH)* across the membrane can be listed as below:

1. Proton release to the lumen phase as a consequence of water oxidation reaction at PS II.
2. Proton uptake from stromal phase for PQ reduction.

3. Proton release into lumen phase during PQH_2 oxidation at cytochrome b6f complex.

4. $NADP^+$ reduction at stromal phase.

On the other hand, vectoral electron transfer process in PS II and PS I initiated by photon absorption could be accounted as the reason for *electric potential difference ($\Delta\Psi$).* Whitmarsh et al. [38] gave the proton electrochemical potential difference with Equation (2).

$$\Delta \mu_{H+} = F\Delta\Psi - 2.3RT\Delta pH \qquad (2)$$

Where F is the Faraday constant, R is the ideal gas constant and T is temperature in Kelvin. They reported that although electric potential difference can be as large as 100 mV, pH difference has a dominating effect in overall electrochemical potential. For a pH difference of 2 (with inner pH 6 and outer pH 8, ΔpH equivalent to 120 mV), the free energy difference across the membrane results in -12 kJ/mol of proton.

In photosynthesis, fastest reactions taking place are the photophysical reactions like light absorption and charge separation in picoseconds orders. They are followed with rapid photochemical processes like electron transfer reactions and with slower biochemical reactions like water splitting and CO_2 reduction.

Since photosynthesis is a series of reactions including photophysical, photochemical and chemical reactions, reaction rates of particular reactions are dependent upon transfer rates of reaction intermediates like electrons or protons. In Figures 2.10 and 2.11, electron transfer times in PS II and PS I are given to illustrate characteristic times of different processes.

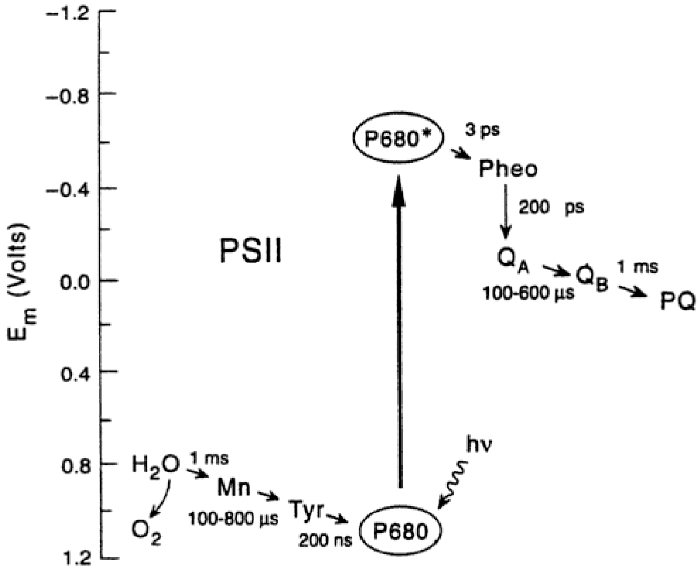

Figure 2.10 PS II electron transport pathways and transfer times with midpoint potentials of electron carriers [38]

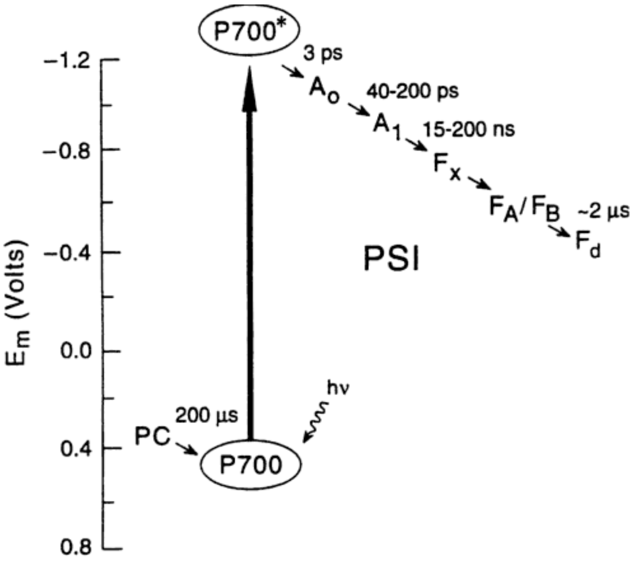

Figure 2.11 PS I electron transport pathways and transfer times with midpoint potentials of electron carriers [38]

Water oxidation and CO_2 reduction reactions are the slowest processes in photosynthesis. S- cycle taking place in PS II for water oxidation is completed with a total of 1.59 ms, which is equivalent to production of 630 molecule of O_2/site/s. On the other hand, turnover frequency given for a subunit of RubisCO for CO_2 reduction is given as 3.3 s^{-1} [39], which is much slower than oxygen evolution. Average photosynthesis rate of a sunflower was given as 13.5 $\mu mol/m^2/s$ by Whittingham et al. [40] and as 12 $\mu mol/m^2/s$ for Brassica pods with an internal CO_2 concentration of 292 ppm by Signal et al. [41] where rate of dark CO_2 fixation was given as 400 nmol/ mg protein/h.

2.2.4 Similarities and Differences between Photosynthesis and Artificial Photosynthesis

Analogy between photosynthesis and artificial photosynthesis is in the similar tools and methods utilized in both systems. Collecting solar energy for triggering chemical reactions by chlorophyll pigments packed in thylakoid membrane or by semiconductors; oxidizing water into molecular oxygen and protons and reducing CO_2 with transported electrons and H^+s are among the similarities of the two systems. However, the gap between the design of the systems and number of reaction sites and intermediate molecules result in more sophisticated such as $(CH_2O)_6$ in photosynthesis and simpler products in photocatalysis (CH_4 or CH_3OH).

In photosynthesis, there are three major reaction centers in light dependent reactions, regulating electron and proton transport together with the intermediate charge carriers (redox components). In photocatalysis, on the other hand, design of the system is limited to the presence of a pool of charges wandering on the semiconductor/metal surface in an unregulated fashion, increasing the chance of recombination of charge carriers. In addition, realization of oxidation and reduction reactions on the same catalyst surface results in interactions between the surface adsorbates which in some cases could be proven to be inhibitory on reaction rates.

In photosynthesis, CO_2 diffusion from atmosphere to stromal phase in chloroplasts is controlled by stomata activities and permeability of chloroplast membranes. Photosynthetic rate is limited with the CO_2 concentration in stromal phase for values lower than a saturation value; i.e., the photosynthetic rate is linearly increasing with CO_2 concentration. For CO_2 concentrations above the saturation value, photosynthetic rate stays constant, limited by the rate of the enzyme system. Since CO_2 concentration in the stromal phase is related to CO_2 diffusion, photosynthetic rate is dependent upon diffusion rates.

In photocatalysis, diffusion of dissolved CO_2 to the catalyst surface is largely dependent upon the reactor types, reaction media and stirring rates. Since the photocatalytic experiments are not standardized, the rate of CO_2 diffusion and its affect on surface concentrations and photocatalytic rates vary to a great extend.

In PSII of photosynthesis, there are over 15 polypeptides and 9 different redox components responsible for water oxidation and electron transport. Even the oxygen evolving complex is regenerating itself at every 30 minutes in order to sustain its stability. Along with the sophistication of light dependent reactions including numerous intermediate charge carriers, difference in the CO_2 reduction mechanism (activating CO_2 by fixing it into another chemical) with 13 specific enzymes result in higher photosynthetic rates and more complicated products (such as glucose) in photosynthesis. On the other hand, C-C bond making is still remaining as a challenge in artificial photosynthesis systems. Even with one carbon chemical synthesis, photocatalytic rates are well below photosynthetic rates. To illustrate, CO_2 reduction using titanium nanotubes resulted in nearly 1 nmol/m^2/s CH_4 production rate [42] whereas an avarage photosynthetic rate is 12 μmol/m^2/s.

2.3 CO_2 PHOTOREDUCTION ON TiO_2

Starting from the pioneering work of Inoue et al. [43], there have been many photocatalytic CO_2 reduction studies with TiO_2. Studies are mainly conducted either in gaseous media or liquid media, in several types of reactors. In gaseous media CO_2 is reduced to CH_4 especially in the presence of Pt [13, 14, 28]; however, in liquid media most commonly encountered reduction product was CH_3OH especially in the presence of Cu [15, 20]. Literature results for photocatalytic CO_2 reduction in gaseous and liquid media for different reactor types are summarized in Table 2.3.

Table 2.3 CO_2 photoreduction normalized rates from literature

BATCH REACTORS					
GAS PHASE			*LIQUID PHASE*		
Photocatalyst	**Normalized Rates (μmol*gcat^{-1}*h^{-1})**		**Photocatalyst**	**Normalized Rates (μmol*gcat^{-1}*h^{-1})**	
	CH_4	**CH_3OH**		**CH_4**	**CH_3OH**
TiO_2[10] H_2O (g)	0,11	0,02	TiO_2 H_2O, Iso-propanol[44]	5,94	
JRC TiO_2 H_2O (g)[9]	0,17		TiO_2 (Degussa P-25) H_2O, 0.2N NaOH[15]		6,37
Cu/TiO_2 H_2O (g)[8]	0,013	0,0015	Cu/TiO_2 H_2O, 0.2N NaOH[15]		19,75
Ti-SBA-15 H_2O(g)[29]	63,60	16,62	TiO_2/SBA-15 H_2O, 0.1N NaOH[20]		627
Ti-MCM-48, H_2O(g)[14]	4,5	1,5	Cu/TiO_2/SBA-15 H_2O, 0.1N NaOH[20]		689,7
Pt/ Ti-MCM-48 H_2O(g)[14]	7,5	0,48	TiO_2 anatase H_2O, 0.2M NaOH[45]	0,38	0,045
TiO_2[46] H_2O (g)	0,2	0,003	Ag/ TiO_2 H_2O, 0.2M NaOH[47]	0,38	0,075
Ex-Ti-oxide/ Y-zeolite H_2O(g)[13]	4,2	2,4	TiO_2 H_2O, 1M isopropanol[48]	0,72	
Pt TiNT H_2O(g)[49]	0,07		Rh /TiO_2 /WO_3 H_2O[50]		2,7
CdSe/Pt/TiO_2 H_2O(g)[51]	0,61	0,04	NiO $InTaO_4$ H_2O, 0.2M NaOH[52]		2,8
NT/Cu-600 H_2O(g)[53]	2,84		CoPc TiO_2 H_2O, 0.1N NaOH[54]		9,3
Average Normalized Photocatalytic Rate w/o Ti-SBA-15		2,5	**Average Normalized Photocatalytic Rate w/o TiO_2 SBA-15**		5,4
Average Normalized Photocatalytic Rate		9,5	**Average Normalized Photocatalytic Rate**		68

Table 2.3 (continued)

CIRCULATED GAS IN BATCH REACTORS			
Photocatalyst	**Reductant**	**CH_4**	**CO**
Cu (1.0 wt%)-ZrO_2 (Ar circulating)[12]	H_2O, $NaHCO_3$		2,5
TiO_2 on pyrex glass (circulated CO_2, H_2, H_2O, N_2)[55]	$H_{2(g)}$	1,46	0,06
TiO_2 on pyrex glass (circulated CO_2, H_2, H_2O, N_2)[55]	$H_2O_{(g)}$	1,64	0,11
ZrO_2 on pyrex glass (circulated CO_2, H_2, H_2O, N_2)[55]	$H_{2(g)}$		0,62
ZrO_2 on pyrex glass (circulated CO_2, H_2, H_2O, N_2) [55]	$H_2O_{(g)}$		0,04
sol-gel TiO_2[56] (CO_2 circulation with gas separation membrane)	$H_2O_{(g)}$		3,5 ppmV/h
TiNT (rxn gases circulation in a batch)[42]	$H_2O_{(g)}$	3,5μmol/m^{2}h	
Ga_2O_3 (closed system with circulated rxn gases)[57]	$H_{2(g)}$		0,72
$LiTaO_3$ (closed system with circulated rxn gases)[58]	$H_{2(g)}$		0,018
Average Normalized Photocatalytic Rate			40

CONTINUOUS FLOW REACTORS			
PACKED BED REACTORS (CO_2 AND H_2O FLOW CONTINUOUSLY)			
Photocatalyst	**Reductant**	**CH_4**	**CH_3OH**
1.2 wt% Cu/TiO_2 coated optical fiber[59]	$H_2O_{(g)}$		0,45
Cu-Fe(0.5wt%)-P25 coated on glass plate[60]	$H_2O_{(g)}$	0,06	
Cu-Fe(0.5wt%)-P25 coated on optical fiber[60]	$H_2O_{(g)}$	0,91	
Cu-Fe(0.5wt%)-P25 glass plate-N_3dye[60]	$H_2O_{(g)}$	0,15	
Cu-Fe(0.5wt%)-P25 optical fiber-N_3 dye[60]	$H_2O_{(g)}$	0,85	
Cu-Fe(0.5wt%)-P25 coated on optical fiber, sunlight[60]	$H_2O_{(g)}$	0,28	
Cu-Fe(0.5wt%)-P25 optical fiber-N_3 dye, sunlight[60]	$H_2O_{(g)}$	0,62	
Cu-Fe(0.5wt%)-TiO_2 SiO_2 optical fiber[61]	$H_2O_{(g)}$	1,86	
Cu-Fe(0.5wt%)-TiO_2 SiO_2 optical fiber, sunlight[61]	$H_2O_{(g)}$	0,28	
NiO $InTaO_4$[52]	$H_2O_{(g)}$		11,1
Average Normalized Photocatalytic Rate			1,7

Table 2.3 (continued)

SEMIBATCH REACTORS (CONTINUOUS CO_2 FLOW)			
Photocatalyst	**Reductant**	**C_2H_5OH**	**CH_3OH**
NiO-$InTaO_4$, visible light[62]	H_2O,$KHCO_3$		1,39
monoclinic $BiVO_4$, visible light[63]	H_2O	21,6	
monoclinic $BiVO_4$, UV+ visible light[63]	H_2O	406	
Average Normalized Photocatalytic Rate			143

As it can be seen from Table 2.3, reported photocatalytic CO_2 reduction rates vary with rector type and reaction media. Although different reactor types and media seem to result in different observed reaction rates, on the overall, photocatalytic CO_2 reduction rates do not seem to be improved in orders of magnitude with few exceptions.

One common practice in photocatalytic studies is the assumption of negligible effect of mass transfer limitations in the observed kinetic rates. This assumption is made based upon the slow photocatalytic reaction rates. However presence of three-phases in liquid phase photocatalytic tests introduces mass transfer limitations at interfaces which could hinder real kinetic rates.

In addition to the different mass transfer rates existing in different reactor types and reaction media, different macro and micromixing conditions in different reactor types could result in changes in kinetic rates and observed rate values respectively. Especially relatively higher photocatalytic rates obtained with gas circulation or semi batch reactors could be explained with the effect of different micromixing conditions on reactions with different reaction orders.

Challenges in liquid media photocatalytic tests arising from mass transfer limitations and possible effects of micromixing conditions on kinetic rates for different types of reactors are discussed in sections 2.3.1 and 2.3.2.

2.3.1 Challenges in CO_2 Photoreduction with H_2O in Three-Phase Systems

Comparison of the CO_2 photoreduction literature results can be fallacious because of the fact that, reaction conditions such as stirring rates, catalyst concentration, liquid volumes and illumination intensities are not standardized for photocatalytic experiments.

In order to understand effect of reaction conditions and be able to report activity test results without any limitations on kinetics, it is required to take a closer look into reaction media and transport phenomena realized in that media.

Majority of CO_2 photoreduction experiments in literature are performed in batch, semi-batch and continuous flow reactors. In experiments where reactions are carried on in liquid media (H_2O_l), CO_2 is fed to the system prior to experiment (batch systems) in order to saturate the solution or it is continuously fed during photocatalytic testing of the catalysts (semi-batch systems).

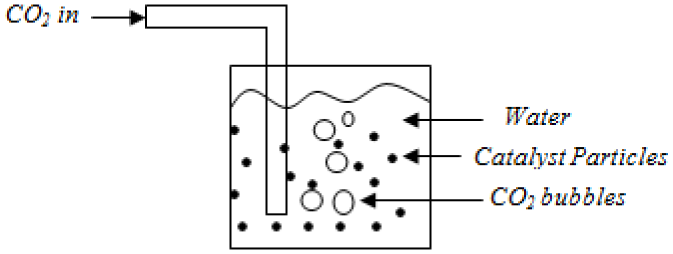

Figure 2.12 Schematic illustration of CO_2 purge to system

When CO_2 is fed to the system; it is dissolved in water with a solubility of 0.033 mol/L of water at 25 °C and 1 atm of CO_2.

$$CO_2(g) \leftrightarrow CO_2(aq)$$

Dissolved CO_2 exists in equilibrium with carbonic acid in water with an equilibrium constant of $1.7*10^{-3}$ at 25 °C which means that majority of CO_2 remains as CO_2 molecules.

$$\mathrm{CO_2(aq) + H_2O(l) \leftrightarrow H_2CO_3(aq)}$$

Carbonic acid dissociates in water to bicarbonate and carbonate ion in two steps:

$$\mathrm{H_2CO_3(aq) \leftrightarrow H^+ + HCO_3^-(aq)} \qquad K_{a1}= 4.6*10^{-7} \text{ at } 25\ °C$$
$$\mathrm{HCO_3^-(aq) \leftrightarrow H^+ + CO_3^{-2}(aq)} \qquad K_{a2}=5.6*10^{-11} \text{ at } 25\ °C$$

In other words, when 1 atm of CO_2 is fed to neutral water, there are 0.033 mol of CO_2, $5.7*10^{-5}$ mol of H_2CO_3 and $1.2*10^{-4}$ mol of HCO_3^- with negligible amount of CO_3^{-2} in 1 liter of water.

Solubility of CO_2 depends on pH of water. Some alkaline chemicals may be present in water, such as NaOH which is used in photocatalytic CO_2 reductions as hole scavengers. In such solutions, alkali-carbonates, such as sodium carbonate or sodium bicarbonate, may be produced with solubilities of 220 g/L and 100g/L respectively at 20 °C.

$$\mathrm{CO_2 + 2NaOH \leftrightarrow Na_2CO_3 + H_2O}$$
$$\mathrm{Na_2CO_3 + CO_2 + H_2O \leftrightarrow 2NaHCO_3}$$

Presence of alkali metals in solution may lead to interaction with catalyst surface which can be detrimental or promoting to/for catalytic activity. To illustrate, Na residues were reported to inhibit the interaction between CuO particles with ZnO matrix in methanol synthesis from CO_2 hydrogenation [64] whereas K residues were reported to facilitate CO_2 activation and dissociation reactions on Rh (111) single crystal by decreasing minimum energy required for photoelectron excitation [65].

2.3.1.1 Mass Transfer Considerations in Liquid Media Photocatalytic Testing

Even though CO_2 exists in CO_2 (aq) and HCO_3^- (aq) forms in neutral water, CO_2 bubbles also exist in the solution together with suspended catalyst particles in CO_2 photocatalytic reduction tests performed in liquid media (Figure 2.13). Presence of three phases in such systems; gas (CO_2), liquid (H_2O) and solid (catalyst particles), may lead to complications especially in mass transfer processes. In order CO_2 (g) to reach catalyst surface, it should overcome mass transfer resistances across gas- liquid- solid interfaces as shown in Figure 2.13.

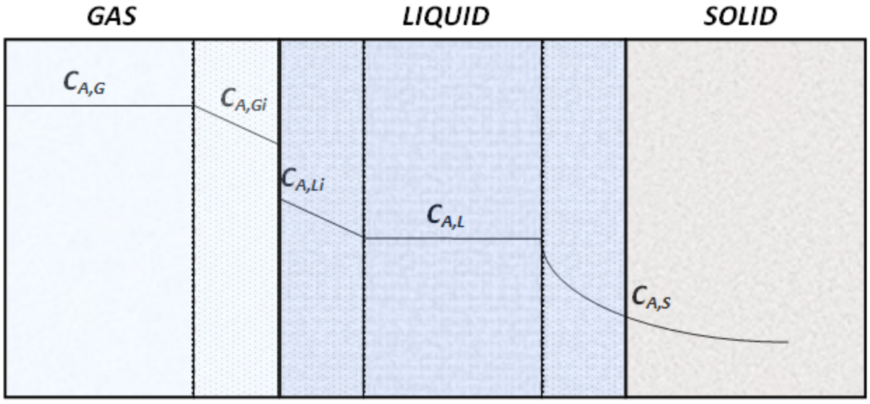

Figure 2.13 Schematic illustration of mass transfer limitations in a slurry reactor

Gas reactant (CO_2) participate five reaction steps in a slurry system:

1. Absorption from the gas phase into the liquid phase at bubble surface: $R_{CO2}= k_G a_b(C_{A,G}-C_{A,Gi})$
2. Diffusion in the liquid phase from bubble surface to bulk liquid: $R_{CO2}= k_L a_b(C_{A,Li}-C_{A,L})$

3. Diffusion from the bulk liquid to the external surface of the solid catalyst: $R_{CO2}= k_s a_p m(C_{A,L}-C_{A,S})$
4. Internal diffusion of the reactant in the porous catalyst
5. Reaction within the porous catalyst: $R_{CO2}= \eta m(-r_{CO2}')$

Mass transfer limitations are frequently overlooked in photocatalytic reaction systems while assuming the system as reaction limited considering slow observed reaction rates. However in three-phase systems, stirring rate plays an important role in observed reaction rates. Increased stirring rates, and equivalently flow rates, in slurry reactors are reported to have improving effects on photocatalytic degradation kinetics for both suspended [66, 67] and immobilized catalysts [68-70] referring to perturbations in concentration profile due to probable boundary layer around catalyst particles.

Diffusion of CO_2 from bulk liquid to external surface of solid particles and also internal diffusion in catalyst particles may alter reaction kinetics, moreover can be rate determining steps due to the probable presence of a boundary layer surrounding catalyst particles in a three-phase system where mixing conditions are not adequate. Especially in cylindrical reactors where mixing is supplied with a magnetic stirrer like the majority of the systems found in literature, there are stagnant zones at the walls of the reactor where formation of boundary layers around catalyst particles is most probable.

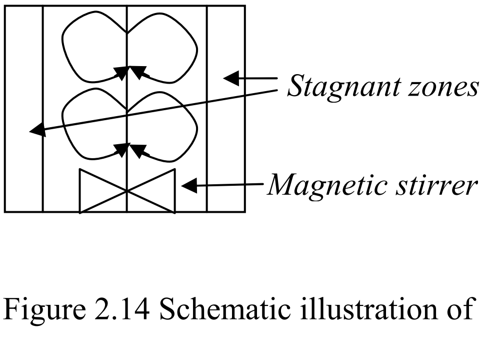

Figure 2.14 Schematic illustration of stagnant zones in a slurry reactor

Super hydrophilicity of TiO_2 under UV irradiation [7, 46, 71] could be accounted as one of the reasons for water boundary layer formation around TiO_2 particles. Mentioned boundary layer of water inhibits diffusion of reactants such as CO_2/ HCO_3^- as well as products to/from catalyst surface to a great extent which results in very low concentrations of reactants on surface.

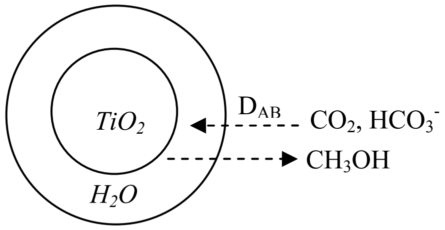

Figure 2.15 Schematic illustration of water boundary layer and diffusion of reactants and products

Even though reactants survive until catalyst surface and react there, same boundary layer will inhibit the diffusion of product to the bulk liquid. More time the products spend on the catalyst surface or in the liquid volume where they can interact with other catalyst particles, more chance there are that they can undergo back-oxidation reactions. Oxidation of the products back to CO_2 and H_2 and negative effects of those back oxidation reactions on photoreduction experiments were reported by Koci et al. 2009 and Tan et al 2007 [45,72]. Recently, enhanced production rates were reported with a gas separation membrane which removes reaction products from reaction surface [56]. Increased reaction yields were achieved since back oxidation reactions were prevented to some extend by removing those intermediates and products from the surface.

2.3.2 Effect of Micromixing Conditions on Reaction Rates

As it can be seen from Table 2.3, gas circulation enhance the rates slightly by postponing equilibrium and preventing back reactions by sweeping away products from catalyst surface. In addition to those, different micromixing conditions introduced in gas circulation reactors may contribute to enhanced rates. Before explaining how, some introductory definition of micromixing, age and life expectation terms will be made.

Starting from 1953 by Danckwert's study, the urge to define non ideal flow patterns in continuous flow reactors was satisfied by introducing "age" and "life expectation" concepts [73, 74]. After describing mixing with two components; macromixing and micromixing, effect of different mixing conditions on reactor performances started to be questioned [75]. Macromixing was defined as being the component that specifies the variation in residence times experienced by the molecules flowing through the system; whereas, micromixing was more concerned with the environment experienced by those molecules.

In plug flow reactors, molecules entering the reactor experience same residence time and therefore same have same life expectation. However molecules inside the reactor have residence times less than entering ones which obstructs micromixing.

In CSTRs, molecules within the reactor and entering to the reactor experience same life expectation and residence time distribution function which is exponential decay function. Micromixing must occur to provide that overlap of those two distributions.

Micromixing is related to the attainment of homogeneity at molecular level and micromixing levels are classified by the earliness or lateness of the association of entering molecules with older molecules within the reactor. Two extremes of micromixing are segregated flow in which association takes place at the exit of the reactor and maximum mixedness in which association is as early as possible.

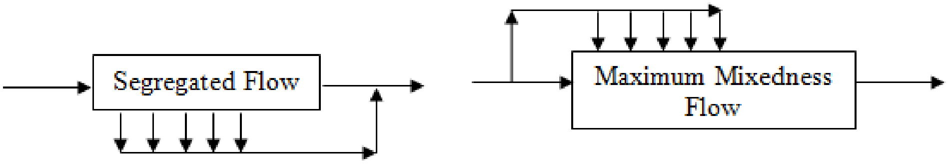

Figure 2.16 Segregated and maximum mixedness flow models

Micromixing conditions affect the chemical reactions by changing their conversions and selectivity. In study of Weinstein et al., segregated flow was observed from calculations to increase second order reaction kinetics and furthermore, Chauhan et al proved the positive effect of micromixing on reaction rates for reactions having orders less than one by a general statement;

- For reactions having reaction rates in the form of $R(C) = k^* C^n$, for $n > 1$ (or $d^2R/dC^2 > 0$), segregation yields maximum conversion.
- For $n = 1$, all micromixing policies yield the same conversion.
- For $n < 1$ (or $d^2R/dC^2 < 0$), maximum mixedness yields maximum conversion [76].

When CO_2 photoreduction reaction with H_2O is concerned, reaction rate Equation (3) is obtained for a Langmuir- Hinshelwood reaction mechanism,

$$r_{CH_3OH} = \frac{kP_{CO_2} P^2{}_{H_2O} I^{\alpha}}{\left[1 + K_{H_2O} P_{H_2O} + K_{CO_2} P_{CO_2}\right]^3} \tag{3}$$

where I is defined as illumination intensity [77].

Reaction rate equation simplifies to Equation (4) assuming higher water adsorption constant and concentration in liquid media (See section 2.4).

$$r_{CH3OH} = \frac{kK_{CO2} P_{CO2} I^{\alpha}}{K_{H2O}^3 P_{H2O}} \tag{4}$$

For reaction order less than one; for H_2O in this situation, maximum mixedness is expected to give better conversions. Therefore, higher mixing rates, approaching to ideal CSTR case is preferred. For CO_2, segregated flow would increase conversion. Both of these conditions; i.e., maximum mixedness for water and segregated flow for carbon dioxide are satisfied with batch reactors with gas circulation of CO_2. This special feature of gas circulation reactors may explain the observed enhanced kinetic reaction rates.

2.4 KINETIC CONSIDERATIONS

2.4.1 Photocatalytic CO_2 Reduction Reaction Mechanism

The photocatalytic CO_2 reduction reaction mechanism still holds its ambiguity, even though there are several propositions like formation of C· and H· and OH· radicals and formation of CH_4 and methanol either from H· or OH· respectively [45, 78].

Mechanism proposed by Tan et al. is as follows [78]:

$$\mathrm{TiO_2} + h\nu \rightarrow \mathrm{e^-} + \mathrm{h^+}$$

$$\left\{\begin{matrix} \mathrm{H_2O} + \mathrm{h^+} \rightarrow \bullet\, \mathrm{OH} + \mathrm{H^+} \\ \bullet\, \mathrm{OH} + \mathrm{H_2O} + 3\mathrm{h^+} \rightarrow \mathrm{O_2} + 3\mathrm{H^+} \end{matrix}\right\}$$

$$2\mathrm{H_2O} + 4\mathrm{h^+} \rightarrow \mathrm{O_2} + 4\mathrm{H^+}$$

$$\left\{\begin{matrix} \mathrm{CO_2} \rightarrow \mathrm{CO} + {}^{1}/_{2}\,\mathrm{O_2} \\ \mathrm{CO} \rightarrow \bullet\, \mathrm{C} + {}^{1}/_{2}\,\mathrm{O_2} \end{matrix}\right\}$$

$$\mathrm{CO_2} \rightarrow \bullet\, \mathrm{C} + \mathrm{O_2}$$

$$\bullet\, \mathrm{C} + 4\mathrm{H^+} + 4\mathrm{e^-} \rightarrow \mathrm{CH_4}$$

$$2\mathrm{H^+} + 2\mathrm{e^-} \rightarrow \mathrm{H_2}$$

And similarly, with the addition of excited state of TiO_2 and formation of methanol, Koci et al. proposed the following mechanism [45]:

$$TiO_2 \overset{hv}{\rightarrow} e^-(TiO_2) + h^+(TiO_2)$$

$$e^-(TiO_2) + h^+(TiO_2) \overset{hv}{\rightarrow} heat$$

$$\mathrm{4h^+ + 2H_2O_{ads}} \xrightarrow{(\mathrm{Ti^{+3}-O^-})^*} \mathrm{O_2 + 4H^+}$$

$$\mathrm{H^+ + e^-} \xrightarrow{(\mathrm{Ti^{+3}-O^-})^*} \bullet\,\mathrm{H}$$

$$\mathrm{CO_2 + e^-} \xrightarrow{(\mathrm{Ti^{+3}-O^-})^*} \mathrm{O} -\bullet\,\mathrm{C - O^-}$$

$$\mathrm{O} -\bullet\,\mathrm{C - O^-} + \bullet\,\mathrm{H} \xrightarrow{(\mathrm{Ti^{+3}-O^-})^*} \mathrm{CO + OH^-}$$

$$\mathrm{CO + e^-} \xrightarrow{(\mathrm{Ti^{+3}-O^-})^*} \bullet\,\mathrm{CO^-}$$

$$\bullet\,\mathrm{CO^-} + \bullet\,\mathrm{H} \xrightarrow{(\mathrm{Ti^{+3}-O^-})^*} \mathrm{C + OH^-}$$

$$\mathrm{OH^- + h^+} \xrightarrow{(\mathrm{Ti^{+3}-O^-})^*} \mathrm{OH}\,\bullet$$

$$\mathrm{C} + \bullet\,\mathrm{H} \xrightarrow{(\mathrm{Ti^{+3}-O^-})^*} \bullet\,\mathrm{CH}$$

$$\bullet\,\mathrm{CH} + \bullet\,\mathrm{H} \xrightarrow{(\mathrm{Ti^{+3}-O^-})^*} \bullet\,\mathrm{CH_2}$$

$$\bullet\,\mathrm{CH_2} + \bullet\,\mathrm{H} \xrightarrow{(\mathrm{Ti^{+3}-O^-})^*} \bullet\,\mathrm{CH_3}$$

$$\bullet\,\mathrm{CH_3} + \bullet\,\mathrm{H} \xrightarrow{(\mathrm{Ti^{+3}-O^-})^*} \bullet\,\mathrm{CH_4}$$

$$\bullet\,\mathrm{CH_3} + \bullet\,\mathrm{OH} \xrightarrow{(\mathrm{Ti^{+3}-O^-})^*} \mathrm{CH_3OH}$$

$$\mathrm{2H}\,\bullet \xrightarrow{(\mathrm{Ti^{+3}-O^-})^*} \mathrm{H_2}$$

As can be seen from proposed mechanisms, CO_2 reduction is not a single step reaction. It requires formation of negatively charged $CO_2^{\delta\bullet-}$ species via electron transfer from catalyst to CO_2 molecules [79, 50].

The methanol production rate mechanism was investigated by Wu et al. [59] and Ren et al. [77] on Cu supported TiO_2 covered optical fibers in gaseous media by changing CO_2 and H_2O partial pressures. Suggested Langmuir-Hinshelwood surface reaction mechanism with competitive adsorption of H_2O and CO_2 on Cu/TiO_2 surface includes also the light intensity term (Equation 3).

Wu et al. estimated the parameters of Equation (3) with correlation of experimental data given in Table 2.4.

Table 2.4 Estimated CO_2 photoreduction L-H parameters, Wu et al. [59]

Parameters	**Value**
k (μmol/g_{cat} bar^3 h)	2481
α	0.20
K_{H2O} (bar^{-1})	51.7
K_{CO2} (bar^{-1})	0.01

Depending on given adsorption parameters, it can be seen that water adsorption on Cu/ TiO_2 dominates CO_2 adsorption; i.e., $K_{H2O}>>K_{CO2}$. Ren et al. suggested a simplified mechanism considering strong adsorption of H_2O as in Equation 5 [77].

$$r_{CH_3OH} = \frac{kP_{CO_2}P^2{}_{H_2O}I^{\alpha}}{\left[1+K_{H_2O}P_{H_2O}\right]^3} \tag{5}$$

Rate parameters and adsorption constants were found by re-arranging Equation (5) and changing partial pressure of water as in Table 2.5.

Table 2.5 Estimated CO_2 photoreduction L-H parameters, Ren et al. [77]

Parameters	**Value**
k (μmol/g_{cat} bar^3 h)	2536
α	0.73
K_{H2O} (bar^{-1})	56

Reported weaker adsorption of CO_2 with TiO_2 than that of H_2O (together with earlier reports; [13, 14]) could be related to photo induced super hydrophilicity of TiO_2 [7, 46, 71] which supports probability of water boundary layer formation around TiO_2 particles.

2.4.2 Catalytic Contributions to Photocatalysis

Sahibzaba et al. [80] revealed that kinetic inhibitions at finite conversions of CO_2 into methanol has been mainly caused by increasing concentration of product water and relatively increasing oxygen coverage on copper surface. Similarly one can infer inhibition of TiO_2 surface in abundance of water for CO_2 photoreduction reactions. Apart from the fact that TiO_2 is super hydrophilic under UV illumination and electronic interactions and also higher tendency of TiO_2 to adsorb water causes a boundary layer of water particles surrounding TiO_2 based photocatalysts, high concentrations of water would make CO_2 activation; i.e., electron transfer from oxygen deficient TiO_2 to CO_2 impossible by oxidizing TiO_2 surface.

Formation of CO_2^- is attributed to the defect structure of TiO_2 by Rasko et al. [81]. Higher oxygen deficiencies of TiO_2 result in higher concentrations of free electrons and therefore ease the electron transfer from Ti^{+3} molecules to CO_2. However one electron reduction potential of CO_2 is much higher than multi electron potential requirements and also higher than conduction band levels of commonly used photocatalysts ($CO_2 + e^- \rightarrow CO_2^{\bullet -}$ $E^0_{redox} = -1.9$ V vs. NHE at pH 7). Therefore, one can say that without a specific interaction between the surface and CO_2, CO_2 reduction is not possible.

Electron affinity of CO_2 molecule is related to the position of lowest unoccupied molecular orbital of CO_2 and conduction band of TiO_2, assuming that electron is transferred from excited state of TiO_2 (Ti^{+3}-O^-) to CO_2. A decrease in lowest unoccupied molecular orbital (LUMO) of CO_2 was reported with lower bond angles that could result from the interaction of the molecule with the surface [82]. According to Indrakanti et al., CO_2 gains electrons from oxygen deficient

TiO_2 via the formation of bent CO_2 molecules near Ti^{+3} sites, whereas electron transfer is not favorable with defect free TiO_2 due to high LUMO of CO_2 [83].

In studies of Solymosi, radical anion CO_2^- was designated to be essential for CO_2 reduction reactions. Addition of electron donating characters such as K to single metal surfaces like Rh (111) or doping TiO_2 with higher valent metals such as W^{+6} increases electron concentration on metals and also electric conductivity of semiconductors (TiO_2) resulting in higher rates of CO_2 activation and also photolysis. (Minimum energy required for photoelectron excitation was reported to decrease with K addition.)

Study of Rasko et al., showed that even if oxygen deficient TiO_2 is compatible to produce CO_2^- anions, it could not dissociate CO_2. For dissociation of CO_2, a metal; Rh, incorporated to TiO_2 surface is needed [81]. Also they reported CO formation on Rh/ TiO_2 catalyst even under dark conditions, with an increase with illumination. In literature dark methane formation was also reported previously although in very small amount [13, 53].

In study of Solymosi et al. where CH_3Cl dissociation on Pd (100) surface was investigated, cleavage of C-Cl bond was found to be photoinduced where as following reactions regarding dissociation of CH_3 to CH_2 and C were designated as thermal processes [84].

Considering above arguments, one can claim that in CO_2 photoreduction reactions, predominant step; CO_2 activation is being realized with the promotion of electron conductivity through generation of photo induced electrons, and following reduction steps were realized catalytically on metal incorporated TiO_2 surface.

Increased CO_2 photoreduction rates at elevated temperatures were observed in literature. In study of Chen et al., methane production activity on magnetron sputtered TiO_2 film was reported to be tripled when temperature was raised to 353 K from 298 K [23]. Similarly methane production from CO_2 reduction was reported to increase to 0.3 $\mu mol*g_{cat}^{-1}*h^{-1}$ from 0.07 $\mu mol*g_{cat}^{-1}*h^{-1}$ as temperature raised from 323 K to 343 K with Pt doped titania nanotubes [49]. Another enhancement in production rates was observed with NiO doped $InTaO_4$

catalyst, in production of methanol; initial production rate was observed to be doubled (from 12 μmole/g_{cat}/h to 24 μmole/g_{cat}/h) as temperature raised to 348 K from 298 K [52].

In a recent study by Uner et al., CH_4 formation under dark conditions was observed upon hydrogen exposure to previously formed carbon deposition on Pt/TiO_2 catalyst. With elevation of temperature to 85 °C from room temperature, methane formation increased approximately 8 times [85]. Photocatalytic methane formation with hydrogenation of CO_2 together with the temperature sensitivity of the photocatalytic CO_2 reduction reaction encourages one to think about the presence of thermally induced steps in CO_2 reduction at which presence of hydrogen or H• radicals play an important role.

In photocatalytic studies and also in photosynthesis, water oxidation reaction is considered to be the key step with very high standard Gibbs free energy: 312 kJ/mol O_2. Concentration and availability of H• radicals on the catalyst surface, limited by the water oxidation rates could be important in photocatalytic CO_2 reduction rates. In order to have a better insight in photocatalytic CO_2 reduction mechanism and possible rate determining steps, kinetic and microkinetic analysis of CO_2 reduction with copper based catalyst were performed regarding the mentioned possible similarities in catalytic and photocatalytic CO_2 reduction reactions mechanisms. Methods and assumptions used in kinetic analysis can be found in Section 3.1.

2.4.3 Catalytic CO_2 Hydrogenation with Copper Based Catalysts

Catalytic CO_2/CO hydrogenation to CH_3OH with copper based industrial Cu/ZnO/Al_2O_3 catalysts is a commercial process for decades with the special emphasis on CO_2 to be the main carbon source of CH_3OH after isotope labeling experiments [86]. Catalytic methanol synthesis was observed to be favored with addition of CO into CO_2 feed, as a consequence of water gas shift reaction [87].

$$CO_2 + 3H_2 \leftrightarrow CH_3OH + H_2O \quad \Delta H_{298} = -49.47\frac{kJ}{mol}\ \Delta G_{298} = 3.30\frac{kJ}{mol}$$

$$CO + H_2O \leftrightarrow CO_2 + H_2 \; \Delta H_{298} = -41.17 \frac{kJ}{mol} \; \Delta G_{298} = -28.64 \frac{kJ}{mol}$$

As it may be seen from catalytic CO_2 hydrogenation to methanol literature results (Table 2.6), methanol production rates increase with increasing space velocities and pressures due to the favorability of CO_2 hydrogenation reaction with high pressures.

Table 2.6 Catalytic methanol synthesis results from literature at different conditions

Catalyst	**P MPa**	**T (°C)**	**H_2/ CO_2**	**GHSV (h^{-1})**	**Rate (μmol *g_{cat}^{-1}* h^{-1})**	**Yield (%)**	**TOF (s^{-1})**
CuO/ZnO[88]	6	240	3:1	14.81 m^3/kg/h	9000		
Pd/CuO/ZnO[88]	6	240	3:1	14.81 m^3/kg/h	10000		
Cu/ ZnO/ Al_2O_3[87]	4.5	250	4:1	54755 h^{-1} 328 m^3/kg/h	220000	0.3	
Cu/ ZnO/ Al_2O_3[87]	5	250	4:1	267 h^{-1} 1.61 m^3/kg/h	22000	6.5	
Cu/ZnO/ Al_2O_3/Cr_2O_3[89]	3	250	3:1	20000 h^{-1} 24 m^3/kg/h	15718	6.87	
Cu/γ Al_2O_3/ TiO_2[90]	3	240	3:1	3600 h^{-1}		13.5	
Cu/ZnO/ Al_2O_3[91]	2	230	3:1	6000 h^{-1}		3.85	0.0087
Cu/ZnO/ TiO_2[91]	2	230	3:1	6000 h^{-1}		3.15	0.0111
Cu/ ZnO/ ZrO_2[92]	1	200	3:1	8.8 m^3/kg/h	2032	2.07	
Cu/ZnO[93]	0.1	167	9:1	12 m^3/kg/h	275		$70*10^{-6}$
Cu/MOF5[94]	0.1	220	36:2:5	1200 h^{-1}	70		
Cu/ZnO/ MOF5[94]	0.1	220	36:2:5	1200 h^{-1}	12		

Higher methanol formation rates (compared to photocatalytic rates; e.g. 20 μmol $*g_{cat}^{-1}*$ h^{-1}) in catalytic CO_2 hydrogenation experiments could be attributed to high temperatures and pressures. For a more proper comparison, catalytic rates at room conditions (as they are in photocatalysis) will be reported via kinetic and microkinetic analysis.

CHAPTER 3

MATERIALS AND METHODS

3.1 CATALYST PREPARATION

3.1.1 Mass Transfer Limitation Experiments

Catalysts used in stirring rate, gas hold-up time and effect of temperature experiments are 0.5 and 1 wt % Pt/ TiO_2 and they were prepared by incipient wetness method. Pt source; Pt $(NH_3)_4Cl_2 \cdot H_2O$ (Alfa Aesar) was dissolved in deionized water and mixed with TiO_2 Degussa P25. After drying at room conditions for one day, and at 120 °C for 2 h, the catalysts were calcined at 410 °C for 5 h.

3.1.2 Photocatalytic CO_2 Reduction Experiments

Commercial TiO_2 Degussa P-25 catalyst and sol- gel prepared TiO_2 catalyst were used in this study with copper; either loaded with incipient wetness method or with direct addition to sol-gel mixture.

There are four sets of catalysts prepared for photoreduction experiments:

3.1.2.1 First Set

First set of Cu/Degussa P25 catalysts (1, 2 and 3 wt %) were prepared by incipient wetness method. In incipient wetness method, copper source; $Cu(NO_3)_2.3H_2O$ was dissolved in 10 ml distilled water for 5 g of TiO_2 Degussa

P25. After dissolving copper salt, TiO_2 Degussa P25 was added and mixed thoroughly. The mixture was left to overnight drying at room conditions and further dried at 150 °C for 2 hours. Finally, the dried catalyst was calcined at 500 °C for 30 minutes under air (Figure 3.1).

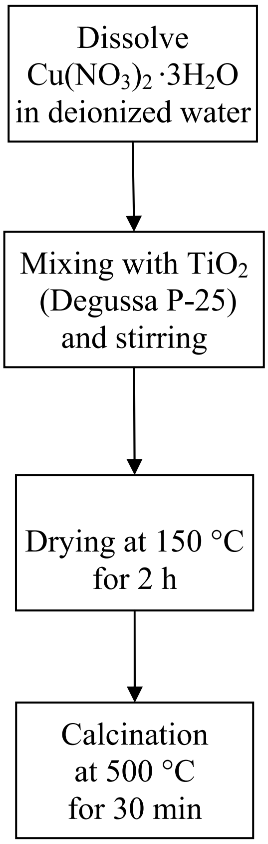

Figure 3.1 Preparation procedure of first set of catalyst; incipient wetness method

3.1.2.2 Second Set

Second set of catalysts were prepared via sol- gel method. In sol-gel method, titanium isopropoxide, ($Ti\{OCH(CH_3)_2\}_4$), ethanol (C_2H_5OH), acetic acid (CH_3COOH), and water is mixed at volumetric ratios of 15:90:1:1 and stirred for 15 h. Afterwards, copper source; Cu $(NO_3)_2$. $3H_2O$ (1 and 2 wt %) was added to the mixture and further stirred for 30 minutes. The mixture was again dried at 150 °C for 2 hours and calcined at 500 °C for 30 minutes (Figure 3.2).

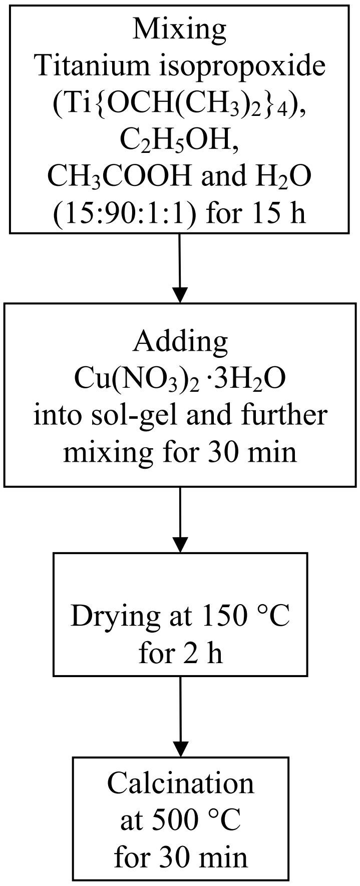

Figure 3.2 Preparation procedure of second set of catalysts

3.1.2.3 Third Set

For preparation of the third set of catalysts; surfactant and also titanium oxide anatase nanopowder (Aldrich, <25 nm) was added to the sol-gel mixture in order to obtain higher surface areas in sol-gel prepared TiO_2. Firstly, surfactant; Pluronic 123 is dissolved in ethanol and then titanium anatase nanopowder, titanium isopropoxide and nitric acid (HNO_3) was added to the mixture. After stirring it for 20 hours, copper source; copper nitrate (II) trihydrate (1 wt %) was added and further stirred for 30 min. The mixture was again dried at 150 °C for 2 hours and calcined at 500 °C for another 2 hours in order to burn surfactant thoroughly (Figure 3.3).

3.1.2.4 Fourth Set

The difference between third set and fourth set of catalysts is that; in fourth set, copper is added to sol-gel prepared catalyst by incipient wetness method. In the sol-gel mixture, surfactant, ethanol, titanium anatase nanopowder, titanium isopropoxide and nitric acid were added and stirred for 80 hours this time, and dried at 150 °C for 2 hours and calcined at 500 °C for 5 hours. After calcination, copper was added by previously mentioned incipient wetness method and further calcined at 500 °C for 2 hours after drying at 150 °C for 2 hours (Figure 3.4).

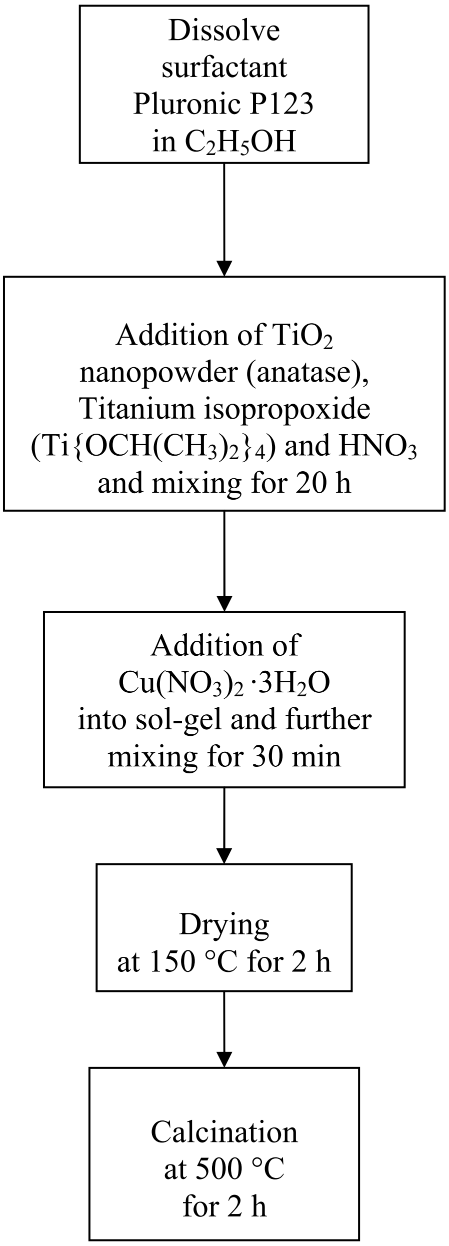

Figure 3.3 Preparation procedure of third set of catalysts

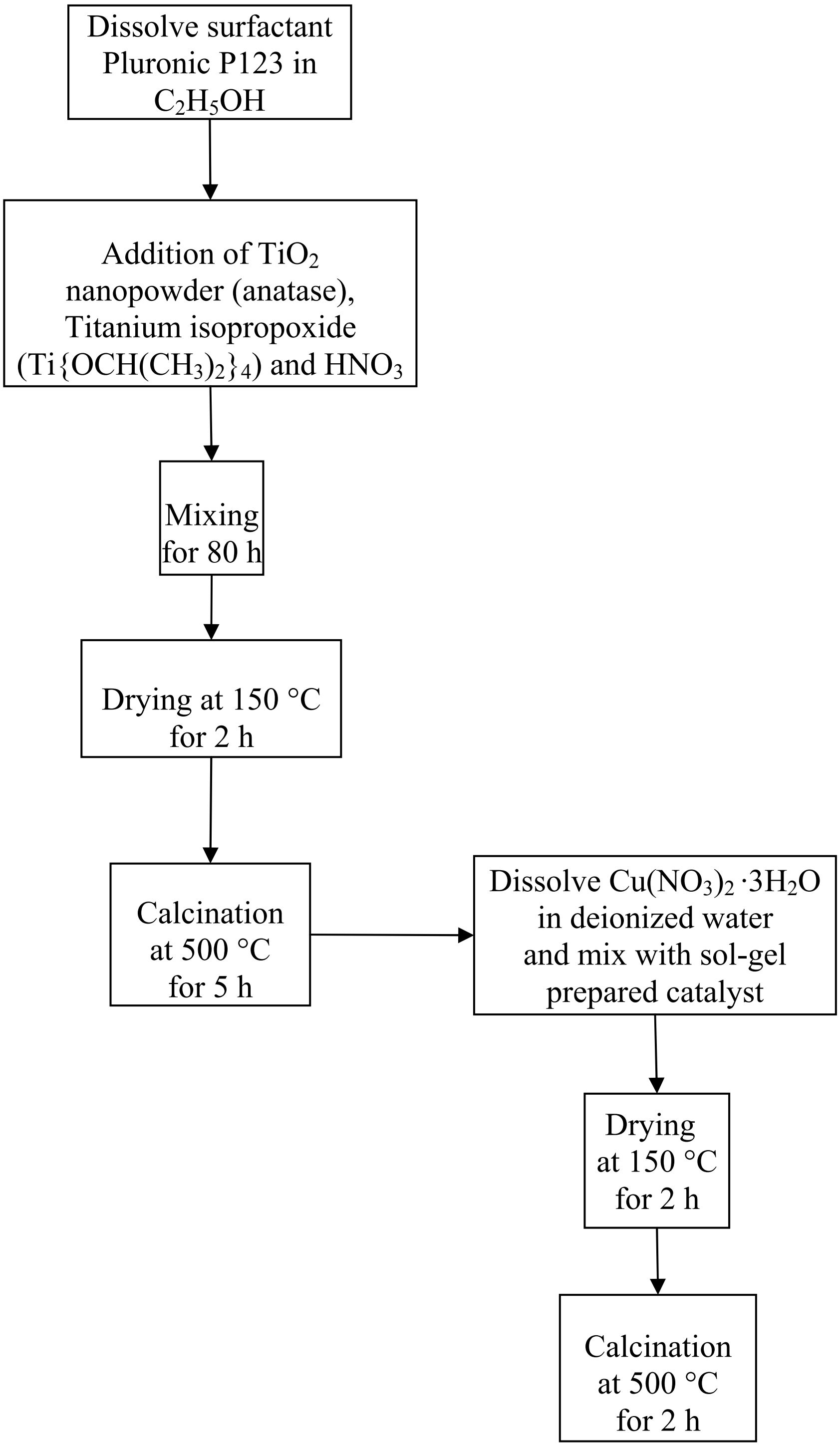

Figure 3.4 Preparation procedure of fourth set of catalysts

3.2 CATALYST CHARACTERIZATION

BET surface area measurements of Cu/TiO_2 catalysts were done by automated ASAP 2000 Micromeritics N_2 adsorption equipment. All of the samples were dried under vacuum in order to eliminate water vapor adsorbed on surface of powder catalysts.

X ray diffraction (XRD) analysis was done to determine crystallinity of the catalysts and also to investigate other phases formed with copper titania. The analysis was done by a Philips PW 1840 Diffractometer.

Transmission Electron Microscopy (TEM) was used to observe morphology of the prepared catalysis and also to measure copper particle sizes on TiO_2. The microscopy was performed with a JEOL JEM 2100F STEM.

X ray photoelectron spectroscopy (XPS) measurements were performed at Central Laboratory, M.E.T.U., as additional information. XPS measurement results can be seen in Appendix C.

3.3 CATALYST TESTING

3.3.1 Mass Transfer Limitation Experiments

In stirring rate and effect of temperature experiments, photocatalytic hydrogen evolution tests were conducted in a batch Pyrex glass reactor containing 250 ml de-ionized water and 2 ml methanol mixture with 0.25 g of catalyst. Total volume of the reactor was measured to be 354 ml comprised 250 ml liquid volume and 104 ml gas volume including pipe connections to manometer. The cylindrical shape Pyrex glass reactor has a diameter of 5 cm and a height of 18 cm, approximately 13 cm of which belongs to liquid volume for 250 ml of water. The magnetic stirrer has a diameter of 3 cm (Figure 3.5).

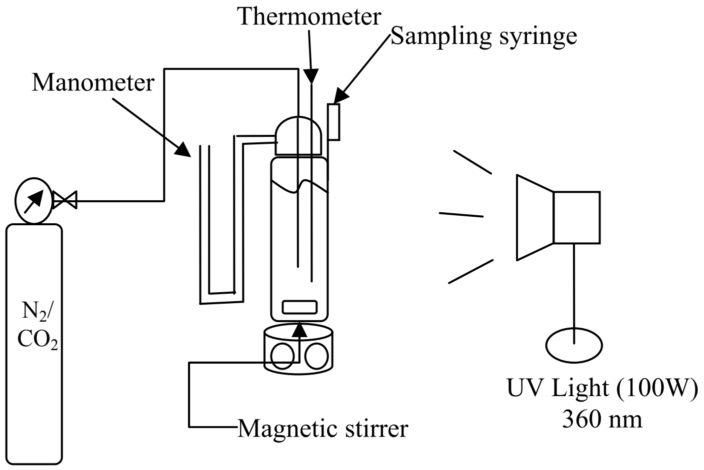

Figure 3.5 Schematic illustration of the set-up

In gas hold-up time experiment, amount of de-ionized water in the same reactor has been changed to 187.5, 125 and 62.5 ml, in order to alter the path distance and hold-up time of product hydrogen in liquid media (before transferred into gas phase). The methanol and catalyst concentration was kept the same for each solution in gas hold-up time experiments. The catalyst concentration was selected to be 1 g/L for each experiment for it is being the optimal concentration reported by Tseng et al. in terms of photo-activation [15].

The solutions were purged with N_2 for 30 min in order to remove dissolved O_2 from deionized water and from closed gas volume. After purging, 100 W UV lamp (365 nm) is activated and batch testing of the catalysts were performed while stirring the solution with a magnetic stirrer. The distance of the UV lamp was taken constant at each experiment and the reactor set up is covered with an aluminum foil for better illumination of the reactor. Gas samples were withdrawn from closed gas volume for every 15 min with a gas syringe and analyzed with a HP 4890 GC with TCD equipped with a 6’ Alltech Porapak Q column (Table 3.1). The pressure and temperature were recorded for each sample withdrawn (Raw data of the experiment and product amount calculations are given in Appendix B). The temperature of the reactor reached to upmost 40 °C because of UV irradiation during reaction.

Table 3.1 GC/ TCD Operation Parameters

Column Characteristics	Alltech Porapak Q 6’ 1/8’’ .085’’
Column Head Pressure	15 psi
Column Temperature	35 °C
Injection Temperature	40 °C
Detector Temperature	50 °C

3.3.2 Photocatalytic CO_2 Reduction Experiments

The photocatalytic testing of the Cu /TiO_2 catalysts for methanol production were done in a Pyrex reactor containing 300 ml of de-ionized water and 0.3 g catalyst under 365 nm UV light illumination (Figure 3.5). Prior to batch testing of the prepared catalysts, CO_2 was purged into the system for 30 minutes in order to saturate the solution. After purging, the system was closed and UV light (100W) was activated while a magnetic stirrer continuously mixed the solution at 1000 rpm.

Liquid samples (1 ml) were withdrawn from the solution every hour and filtered through millipore filters in order to eliminate catalyst particles from the solution. After filtering, samples were kept in sample holder and withdrawn with liquid syringes (2 μl) for GC analysis.

The samples were analyzed with HP-5890 GC, with flame ionization detector, equipped with a 12’ Porapak Q column. Operation method parameters were given in Table 3.2.

Table 3.2 GC/ FID Operation Parameters

Column Characteristics	Alltech Porapak Q 12’ 1/8’’ .085’’
Column Head Pressure	40 psi
Column Temperature	150 °C
Injection Temperature	220 °C
Detector Temperature	230 °C

3.4 KINETIC AND MICROKINETIC MODELLING OF METHANOL FORMATION

3.4.1 Calculation of Methanol Formation Rates with the Steady State Kinetic Model Proposed by Vanden Bussche et al. [95]

Methanol formation rates through CO_2 hydrogenation and water gas shift reactions over a Cu based catalyst were calculated by using steady state kinetic model proposed by Vanden Bussche et al. for $Cu/ZnO/Al_2O_3$ catalyst [95]. In their model, CO_2 was taken as the main source of carbon in methanol whereas water gas shift reaction produces extra CO_2.

$$CO_2 + 3H_2 \leftrightarrow CH_3OH + H_2O$$
$$CO + H_2O \leftrightarrow CO_2 + H_2$$

Methanol production rate was derived by assuming a pseudo steady state concentration of surface intermediates. Rate determining steps were selected to be $CO_2(g) + * \leftrightarrow O * + CO(g)$ for water gas shift reaction and $HCO_2 ** + H * \leftrightarrow H_2CO_2 ** + *$ for CO_2 hydrogenation.

Rate equations of methanol synthesis and reverse water gas shift reactions were given in Equations (6-8).

$$r_{CH3OH} = k_{5a}K_2K_3K_4K_{H2}p_{CO2}p_{H2}\left(1 - \frac{1}{K_1}\frac{p_{H2O}p_{CH3OH}}{p_{H2}^3p_{CO2}}\right)\beta^3 \quad (6)$$

$$r_{CO} = k_1p_{CO2}\left(1 - K_3\frac{p_{H2O}p_{CO}}{p_{CO2}p_{H2}}\right)\beta \quad (7)$$

$$1/\beta = 1 + \frac{K_{H2O}}{K_{H2}K_8K_9}\frac{p_{H2O}}{p_{H2}} + \sqrt{K_{H2}p_{H2}} + K_{H2O}p_{H2O} \quad (8)$$

The equilibrium constants (K_1, K_3) were taken from Graaf et al. as in Equations 9 and 10 [96].

$$K_1 = 10^{\frac{3066}{T} - 10.592} \quad (9)$$

$$K_3 = \frac{1}{10^{\frac{-2073}{T} + 2.029}} \quad (10)$$

Parameters in the kinetic model were estimated by fitting experimental data with a temperature range of 453 – 553 K. Therefore, parameters, product of rate constants and equilibrium constants, could be used safely only within mentioned temperature range.

Estimated parameters [95]:

$$k_{5a}K_2K_3K_4K_{H2} = 1.07exp\left(\frac{36696}{RT}\right)$$

$$\frac{K_{H2O}}{K_{H2}K_8K_9} = 3453.38$$

$$\sqrt{K_{H2}} = 0.499exp\left(\frac{17197}{RT}\right)$$

$$K_{H2O} = 6.62 * 10^{-11}\ exp\left(\frac{124119}{RT}\right)$$

$$k_1 = 1.22 * 10^{10}exp\left(\frac{-94765}{RT}\right)$$

Given rate equations were used in steady state modeling of a packed bed reactor with constant pressure and temperature assumption. Initial methanol formation rates at the start of the reactor were calculated with feed gas molar compositions of 5% CO_2, 25 % CO, 70 % H_2 and 2 % H_2O, 4% CO_2, 24 % CO, 70 % H_2 with a total molar flow rate of 0.27 mol/s for each case. Molar composition of the feed was determined based on the optimal conditions for highest methanol yields reported by Klier et al. in his study [97].

Equations used in initial methanol formation rate calculations are as follows:

$$\frac{dF_{CO2}}{dw} = r_{CO2}, \frac{dF_{CO}}{dw} = r_{CO}, \frac{dF_{H2}}{dw} = r_{H2}, \frac{dF_M}{dw} = r_M, \frac{dF_W}{dw} = r_W$$

Where $r_{CO2} = -r_M - r_{CO}$ and $r_{H2} = -3r_M - r_{CO}$ and $r_W = r_M + r_{CO}$

And

$$p_{CO} = \frac{F_{CO}}{F_T}P$$

$$p_{CO2} = \frac{F_{CO2}}{F_T}P$$

$$p_{H2} = \frac{F_{H2}}{F_T}P$$

$$p_{CH3OH} = \frac{F_M}{F_T}$$

$$p_{H2O} = \frac{F_W}{F_T}P$$

$$F_T = F_{CO2} + F_{CO} + F_{H2} + F_M + F_W$$

3.4.2 Calculation of Methanol Formation Rates with the Static Kinetic Model Proposed by Ovesen et al. [98]

As mentioned in previous section, kinetic model proposed by Vanden Bussche et al. did not cover temperature ranges below 453 K. In order to obtain more accurate rate data at low temperatures also, a kinetic model of methanol synthesis over a Cu based catalyst, proposed by Ovesen et al. was used [98]. In this model, parameters were obtained from surface science studies and also from partition functions of intermediates.

Elementary steps in this kinetic model including CO_2 hydrogenation and water gas shift reactions are given in Table 3.3.

Table 3.3 Elementary Steps in the Kinetic Model of Methanol Synthesis [98]

Steps	**Surface reactions**
1	$H_2O + * \leftrightarrow H_2O *$
2	$H_2O * + * \leftrightarrow OH * + H *$
3	$2OH * \leftrightarrow H_2O * + O *$
4	$OH * + * \leftrightarrow O * + H *$
5	$2H * \leftrightarrow H_2 + 2 *$
6	$CO + * \leftrightarrow CO *$
7	$CO * + O * \leftrightarrow CO_2 * + *$
8	$CO_2 * \leftrightarrow CO_2 + *$
9	$CO_2 * + H * \leftrightarrow HCOO * + *$
10	$HCOO * + H * \leftrightarrow H_2CO * + O *$
11	$H_2CO * + H * \leftrightarrow H_3CO * + *$
12	$H_3CO * + H * \leftrightarrow H_3COH * + *$
13	$CH_3OH * \leftrightarrow CH_3OH + *$

In this kinetic model, steps 2, 4, 7 and 11 were assumed to be slow and all other steps were considered relatively fast and in equilibrium. Rate determining step of methanol synthesis was taken to be methoxide formation (step 11) and CO_2 formation (step 7) for water gas shift reaction. Under these considerations, methanol and water synthesis rate equations were given in Equations (11) and (12) [99]:

$$r_{CH3OH} = k_{-11}K_{11}K_{10}\frac{\theta_{HCOO*}\theta_H^2}{\theta_*} - k_{-11}\theta_{H3CO*}\theta_{O*} \tag{11}$$

$$r_{H2O} = k_{-11}K_{11}K_{10}\frac{\theta_{HCOO*}\theta_H^2}{\theta_*} - k_{-11}\theta_{H3CO*}\theta_{O*} - k_7\theta_{CO*}\theta_{O*} + \frac{k_7}{K_7}\theta_{CO2*}\theta_* \tag{12}$$

Rate constants belonging to slow steps were fitted from experimental data (with a temperature range of 485- 580 K) (Table 3.4).

Table 3.4 Rate constants for Cu (111) used in the kinetic model $k_i= A_i* \exp(-E_i/RT)$ [99]

Steps	**A_i (s^{-1})**	**E_i (kJ/mol)**
2	$2.6*10^{14}$	114
4	$2.3*10^{8}$	99.1
7	$1.1*10^{13}$	72.2
9	$2.1*10^{10}$	78
11	$7.8*10^{20}$	161.8

Equilibrium constants for fast reactions in the kinetic model were calculated from the partition functions of each species:

$K_1=z_{H2O*}/ z_{H2O}$

$K_2=z_{OH*}z_{H*}/z_{H2O*}$

$K_3=z_{H2O*}z_{H*}/z_{OH*}$

$K_4=z_{O*}z_{H*}/z_{OH*}$

$K_5=z_{H2}/z^2_{H*}$

$K_6=z_{CO*}/z_{CO}$

$K_7=z_{CO2}/z_{CO*}z_{O*}$

$K_8=z_{CO2}/z_{CO2*}$

$K_9=z_{HCOO*}/z_{H*}z_{CO2*}$

$K_{10}=z_{H2COO*}/z_{H*}z_{HCOO*}$

$K_{11}=z_{H3CO*}z_{O*}/z_{H*}z_{H2COO*}$

$K_{12}=z_{CH3OH*}/z_{H*}z_{H3CO*}$

$K_{13}=z_{CH3OH}/z_{CH3OH*}$

Where the partition function of a species is the product of its translational, vibrational, rotational and ground state partition functions. ($z = z_t\, z_v\, z_r\, z_e$)

3.4.2.1 Calculation of Molecular Partition Functions

For gas molecules translational partition function was calculated from Equation (13).

$$z_t = \left(\frac{2\pi m k_B T}{h^2}\right)^{\frac{3}{2}} * \frac{k_B T}{P} \tag{13}$$

for triple degeneracy (where P is 1 atm reference pressure).

For adsorbed molecules, translation was taken as frustrated translation accounting vibrations of the molecule parallel and orthogonal to surface (Equation (14)).

$$z_t = \frac{\exp\left(-\frac{\left(\frac{1}{2}\right)hc\nu_{\perp}}{k_B T}\right)}{1-\exp\left(-\frac{hc\nu_{\perp}}{k_B T}\right)} * \frac{\exp\left(-\frac{hc\nu_{\parallel}}{k_B T}\right)}{\left(1-\exp\left(-\frac{hc\nu_{\parallel}}{k_B T}\right)\right)^2} \tag{14}$$

Vibrational partition function, z_v, was calculated for each vibrational degree of freedom from with Equation (15).

$$z_v = \frac{\exp\left(-\frac{\left(\frac{1}{2}\right)hc\nu}{k_B T}\right)}{1-\exp\left(-\frac{hc\nu}{k_B T}\right)} \tag{15}$$

Rotational partition function for gas linear molecules was calculated from Equation (16).

$$z_r = \frac{k_B T}{\sigma h c B} \tag{16}$$

For nonlinear gas molecules:

$$z_r = \frac{\sqrt{8}\pi^{1/2}(k_B T)^{3/2}(I_A I_B I_C)^{1/2}}{\sigma h^3} \tag{17}$$

The ground state partition function, z_e, is given as :

$$z_e = \exp\left(-\frac{E_e}{k_B T}\right) \tag{18}$$

Partition function values of species involved at methanol synthesis were calculated with the vibrational parameters given by Ovesen et al. (Table 3.5).

Table 3.5 Thermodynamic parameters used in partition function calculations [98]

Species	**Vibrational parameters**	**Energy , E_g**
H_2(g)	B= 60.9 cm^{-1}, σ=2, ν_1 = 4405 cm^{-1}	-35 kJ/ mol
H*	$\nu_{\perp}$= 1121 cm^{-1}, $\nu_{\parallel}$=928 (2) cm^{-1}	Cu(111): -40.7 kJ/ mol
H_2O (g)	$I_AI_BI_C$= 5.77*10^{-141} kg^3m^6, σ=2, ν_1 = 1595 cm^{-1}, ν_2 = 3657 cm^{-1}, ν_3 = 3755 cm^{-1}	-305.6 kJ/ mol
H_2O*	$\nu_{\perp}$= 460 cm^{-1}, $\nu_{\parallel}$=48 (2) cm^{-1}, ν_r = 745(3) cm^{-1}, ν_1 = 1600 cm^{-1}, ν_2 = 3370(2) cm^{-1}	Cu(111): -362.6 kJ/ mol
O*	$\nu_{\perp}$= 391 cm^{-1}, $\nu_{\parallel}$=508 (2) cm^{-1}	-243.8 kJ/mol
OH*	$\nu_{\perp}$= 280 cm^{-1}, $\nu_{\parallel}$=49 (2) cm^{-1}, ν_r = 670(2) cm^{-1}, ν_1 = 3380 cm^{-1}	Cu(111): -309.6 kJ/ mol
CO(g)	B= 1.93 cm^{-1}, σ=1, ν_1 = 2170 cm^{-1}	-132.2 kJ/ mol
CO*	$\nu_{\perp}$= 343 cm^{-1}, $\nu_{\parallel}$=24 (2) cm^{-1}, ν_r = 290(3) cm^{-1}, ν_1 = 2089 cm^{-1}	Cu(111): -186.1kJ/ mol
CO_2(g)	B= 0.39cm^{-1}, σ=2, ν_1 = 667 cm^{-1}, ν_2 = 1343 cm^{-1}, ν_3 = 2350 cm^{-1}	-433 kJ/ mol
CO_2*	$\nu_{\perp}$=410 cm^{-1}, $\nu_{\parallel}$=31 (2) cm^{-1}, ν_r = 13(2) cm^{-1}, ν_1 = 667 cm^{-1}, ν_2 = 1343 cm^{-1}, ν_3 = 2349 cm^{-1}	Cu(111): -460.3 kJ/ mol
HCOO*	$\nu_{\perp}$=322 cm^{-1}, $\nu_{\parallel}$=36 (2) cm^{-1}, ν_r = 400(3) cm^{-1}, ν_1 = 758 cm^{-1}, ν_2 = 1331 cm^{-1}, ν_3 = 1640 cm^{-1}, ν_4 = 2879 cm^{-1}, ν_5 = 1073 cm^{-1}, ν_6 = 1377 cm^{-1}	Cu(111): -552.7 kJ/ mol

Table 3.5 (continued)

Species	**Vibrational parameters**	**Energy , E_g**
CH_3O^*	$\nu_{\perp}$=400 cm^{-1}, $\nu_{\parallel}$=37 (2) cm^{-1}, ν_r = 360(3) cm^{-1}, ν_1 = 1020 cm^{-1}, ν_2 = 1150(2) cm^{-1}, ν_3 = 1460(3) cm^{-1}, ν_4 = 2840 cm^{-1}, ν_5 = 2940(2) cm^{-1}	Cu(111): -300 kJ/ mol
H_2COO^*	$\nu_{\perp}$=405 cm^{-1}, $\nu_{\parallel}$=30 (2) cm^{-1}, ν_r = 400(3) cm^{-1}, ν_1 = 630 cm^{-1}, ν_2 = 960 cm^{-1}, ν_3 = 1090 cm^{-1}, ν_4 = 1220(2) cm^{-1}, ν_5 = 1420 cm^{-1}, ν_6 = 1480 cm^{-1}, ν_7 = 2920 cm^{-1}, ν_8 = 3000 cm^{-1}	Cu(111): -568 kJ/ mol
$CH_3OH(g)$	I_A= 6.68*10^{-47} kgm^2 I_B= 34*10^{-47} kgm^2 I_C= 35.31*10^{-47} kgm^2, σ=3, ν_1 = 270 cm^{-1}, ν_2 = 1033 cm^{-1}, ν_3 = 1060 cm^{-1}, ν_4 = 1165 cm^{-1}, ν_5 = 1345 cm^{-1}, ν_6 = 1477(2) cm^{-1}, ν_7 = 1455 cm^{-1}, ν_8 = 2844 cm^{-1}, ν_9 = 2960 cm^{-1}, ν_{10} = 3000 cm^{-1}, ν_{11} = 3681 cm^{-1}	-342.8 kJ/mol
CH_3OH^*	$\nu_{\perp}$=290 cm^{-1}, $\nu_{\parallel}$=36 (2) cm^{-1}, ν_r = 360(3) cm^{-1}, ν_1 = 750 cm^{-1}, ν_2 = 820 cm^{-1}, ν_3 = 1030 cm^{-1}, ν_4 = 1150(2) cm^{-1}, ν_5 = 1470(3) cm^{-1}, ν_6 = 2860 cm^{-1}, ν_7 = 2970(2) cm^{-1}, ν_8 = 3320 cm^{-1}	Cu(111): -413.3 kJ/ mol

For steady state methanol production rate calculations, same packed bed reactor mole balances were used with a 0.27 total initial molar flow rate and feed gas composition of 2 % H_2O, 4% CO_2, 24 % CO and 70 % H_2. Again pressure and temperature values are taken as constant. Rate value, which was given as molecules/site/s, was multiplied with 24.4μmol/m^2Cu (density of Cu active sites taken from Xia et al. [100]) and 5.5 m^2Cu/g_{cat} in mole balances in order to be consistent with F_i (mol/s).

3.4.3 Microkinetic Modeling of CO_2 Hydrogenation using Finite Difference Method and Pseudo Steady State Approximation

Rate determining steps in proposed kinetic models were selected based on methanol formation experiments conducted at temperature ranges between 450 and 580 K. However using kinetic models with the same rate determining steps for methanol formation reaction occurring at lower temperatures is not reasonable. Rate mechanism with the slowest rate may change upon significant decreases in temperature. In order to prevent such inexact results, a microkinetic modeling without a rate determining step was performed with finite differences method and pseudo steady state approximation.

In this microkinetic model, molar and thermodynamic consistency was sought. Reaction steps and total reaction including CO_2 hydrogenation and water gas shift reaction can be seen in Table 3.6.

Table 3.6 Elementary reaction steps used in microkinetic modeling

Steps	**Reactions**
1	$5/H_2 + * \leftrightarrow H_2 *$
2	$5/H_2 * + * \leftrightarrow 2H *$
3	$CO_2 + * \leftrightarrow CO_2 *$
4	$CO + * \leftrightarrow CO *$
5	$CO * + O * \leftrightarrow CO_2 * + *$
6	$2/CO_2 * + H * \leftrightarrow HCOO * + *$
7	$2/HCOO * + H * \leftrightarrow H_2CO * + O *$
8	$2/H_2CO * + H * \leftrightarrow H_3CO * + *$
9	$2/H_3CO * + H * \leftrightarrow H_3COH * + *$
10	$2/CH_3OH * \leftrightarrow CH_3OH + *$
11	$O * + H * \leftrightarrow OH * + *$
12	$OH * + H * \leftrightarrow H_2O * + *$
13	$H_2O * \leftrightarrow H_2O + *$
Total	$CO_2 + CO + 5H_2 \leftrightarrow 2CH_3OH + H_2O$

3.4.3.1 Activation Energy Barrier Calculations for Each Step

Enthalpy changes of reaction steps and individual activation energy barriers were calculated using Bond Order Conservation – Morse Potential Method, which is further developed and named as Unity Bond Index Quadratic Exponential Potential (UBI-QEP) method.

In Bond Order Conservation- Morse Potential Method, energetics of chemisorption and surface reactions can be described in an accurate manner with basic inputs such as atomic heats of adsorption and gas phase molecular bond energies. The method is suggested to estimate energetics of complex reactions with an accuracy of ±1-3 kcal/mol [101].

Heats of chemisorptions on Cu (111) and total bond energies in gas phase for species involved in methanol synthesis reaction were calculated and listed by Shustorovich et al. [101].

Table 3.7 Heats of chemisorptions and total bond energies for reaction species given on Cu (111)

Species	**Total Bond Energies (kj/mol)**	**Heat of Chemisorption on Cu (111) (kJ/mol)**
H	-	234
C	-	502
O	-	431
OH	427	218
HCOO	1607	247
H_2CO	1511	67
CH_3O	1603	230
H_2	435	21
CO_2	1607	21
CO	1076	50
CH_3OH	2038	63
H_2O	921	59

From heats of chemisorptions and bond energies, enthalpy change of reactions can be calculated using Equation (19).

$$\Delta H = \sum Q_r - \sum Q_p + \sum D_b - \sum D_f \qquad (19)$$

Where Q_r and Q_p are the heats of chemisorption of reactants and products, D_b and D_f are the binding energies of the bonds that are broken and formed respectively.

Forward activation energy barrier for a dissociation reaction from a chemisorbed state is given as Equation (20):

$$ABs + s \leftrightarrow As + Bs$$

$$E_{f,s} = \frac{1}{2}\left[\Delta H + \frac{Q_A Q_B}{Q_A + Q_B}\right] \tag{20}$$

And reverse activation barrier could be calculated from Equation (21).

$$E_f - \Delta H = E_r \tag{21}$$

For the dissociation reactions in which gas phase species are involved, heat of adsorption of dissociated molecule, Q_{AB} should be subtracted from the barrier of dissociation reaction involving surface adsorbates (Equation (22)).

$$AB(g) + 2s \leftrightarrow As + Bs$$

$$E_{f,g} = E_{f,s} - Q_{AB} \tag{22}$$

For recombination reactions, for one dimensional cases such as, COs+ Os→ CO_2s+s, forward activation barrier was given as in Equation (23):

$$As + Bs \leftrightarrow ABs + s$$

$$E_{f,s} = \frac{Q_A Q_B}{Q_A + Q_B} \tag{23}$$

For disproportionation reactions such as As+ BCs→ ABs+ Cs, the forward activation barrier can be calculated with Equation (24) provided that direction of the reaction was set right with the condition $D_{BC} > D_{AB}$ satisfied..

$$E_{f,s} = \frac{1}{2}\left[\Delta H + \frac{Q_{AB} Q_C}{Q_{AB} + Q_C}\right] \tag{24}$$

3.4.3.2 Calculation of Pre-Exponentials

In most of the microkinetic studies, preexponential factors were assumed from Transition State Theory, in which entropy change of the elementary steps were not taken into consideration. In this model, a combination of transition state theory and Lunds methodology was used in order to sustain thermodynamic consistency of the reaction.

In order to achieve this, firstly the entropy change of each step was calculated from partition function of species.

Since equilibrium constant of a reaction is given as:

$$K = \frac{z_C z_D}{z_A z_B} exp\left(-\frac{\Delta H^0}{RT}\right) \quad (25)$$

and

$$K = exp\left(\frac{\Delta S^0}{R}\right) exp\left(-\frac{\Delta H^0}{RT}\right) \quad (26)$$

therefore;

$$\frac{Af}{Ar} = \frac{z_C z_D}{z_A z_B} = exp\left(\frac{\Delta S^0}{R}\right) \quad (27)$$

for a reaction : A+ B → C+ D, net entropy change of each reaction can be found from K_i.

After calculating A_f/A_r, one of the pre-exponentials was assumed from TST ($10^{13}s^{-1}$ for a surface reaction, immobile species [102]) and the other one was calculated according to entropy change of that step (Equation (28)).

$$A_f = A_r * exp\left(\frac{\Delta S_i}{R}\right) \quad (28)$$

3.4.3.3 Finite Difference Method

In the finite difference method, forward and reverse elementary reaction rates for reaction: $CO_2 + CO + 5H_2 \leftrightarrow 2CH_3OH + H_2O$ were solved for a batch system. It was assumed to be 5 g of Cu based catalyst in a 1 L of reactor. Initial moles of reactants were calculated from initial pressures. Initial molar fractions of gases were taken as: %70 H_2, %25 CO and %5 CO_2. Density of copper active sites and copper surface area were taken as 24.4 µmol/ m^2Cu and 5.5 m^2Cu/g_{cat} respectively. Therefore, reaction rate, which was originally in molecules * $site^{-1}$* s^{-1}, was multiplied with $24.4*10^{-6}$ mol/m^2Cu*5.5 m^2Cu/g_{cat} *5 g_{cat}* $6.02*10^{-23}$ sites/ 1 mol /$6.02*10^{-23}$ molecules* 1 mol= $6.71*10^{-4}$ site*mol/molecule.

According to given reaction steps (Table 3.6), moles in the reactor and coverages on catalyst surface of the species were calculated by using below equations order to sustain stoichiometry:

$$N_{H2}\,|_{\,t1} = N_{H2}\,|_{\,t0} + (-5 * r_1 + 5 * r_{-1}) * 6.71 * 10^{-4} * \Delta t$$

$$N_{CO2}\,|_{\,t1} = N_{CO2}\,|_{\,t0} + (-r_3 + r_{-3}) * 6.71 * 10^{-4} * \Delta t$$

$$N_{CO}\,|_{\,t1} = N_{CO}\,|_{\,t0} + (-r_4 + r_{-4}) * 6.71 * 10^{-4} * \Delta t$$

$$N_{H2O}\,|_{\,t1} = N_{H2O}\,|_{\,t0} + (r_{13} - r_{-13}) * 6.71 * 10^{-4} * \Delta t$$

$$N_{CH3OH}\,|_{\,t1} = N_{CH3OH}\,|_{\,t0} + (2 * r_{10} - 2 * r_{-10}) * 6.71 * 10^{-4} * \Delta t$$

$$\theta_{H2}\,|_{\,t1} = \theta_{H2}\,|_{\,t0} + (5 * r_1 - 5 * r_{-1} - 5 * r_2 + 5 * r_{-2})\Delta t$$

$$\theta_{CO2}\,|_{\,t1} = \theta_{CO2}\,|_{\,t0} + (r_3 - r_{-3} + r_5 - r_{-5} - 2 * r_6 + 2 * r_{-6})\Delta t$$

$$\theta_{CO}\,|_{\,t1} = \theta_{CO}\,|_{\,t0} + (r_4 - r_{-4} - r_5 + r_{-5})\Delta t$$

$$\theta_{HCOO}\,|_{\,t1} = \theta_{HCOO}\,|_{\,t0} + (2 * r_6 - 2 * r_{-6} - 2 * r_7 + 2 * r_{-7})\Delta t$$

$$\theta_{H2CO}\,|_{\,t1} = \theta_{H2CO}\,|_{\,t0} + (2 * r_7 - 2 * r_{-7} - 2 * r_8 + 2 * r_{-8})\Delta t$$

$$\theta_{H3CO}\,|_{\,t1} = \theta_{H3CO}\,|_{\,t0} + (2 * r_8 - 2 * r_{-8} - 2 * r_9 + 2 * r_{-9})\Delta t$$

$$\theta_{CH3OH}\,|_{\,t1} = \theta_{CH3OH}\,|_{\,t0} + (2 * r_9 - 2 * r_{-9} - 2 * r_{10} + 2 * r_{-10})\Delta t$$

$$\theta_{O}\,|_{\,t1} = \theta_{O}\,|_{\,t0} + (-r_5 + r_{-5} + 2 * r_7 - 2 * r_{-7} - r_{11} + r_{-11})\Delta t$$

$$\theta_{OH}\,|_{\,t1} = \theta_{OH}\,|_{\,t0} + (r_{11} - r_{-11} - r_{12} + r_{-12})\Delta t$$

$$\theta_{H2O}\,|_{\,t1} = \theta_{H2O}\,|_{\,t0} + (r_{12} - r_{-12} - r_{13} + r_{-13})\Delta t$$

$$\theta_{H}\,|_{\,t1} = \theta_{H}\,|_{\,t0} + (10 * r_2 - 10 r_{-2} - 2 * r_6 + 2 * r_{-6} - 2 * r_7 + 2 * r_{-7} - 2 * r_8 + 2 * r_{-8} - 2 * r_9 + 2 * r_{-9} - r_{11} + r_{-11} - r_{12} + r_{-12})\Delta t$$

Giving the net reaction: $CO_2 + CO + 5H_2 \leftrightarrow 2CH_3OH + H_2O$.

3.4.3.4 Pseudo Steady State Approximation

Although methanol formation rates and surface coverage trends could be calculated and observed for a defined time interval (up to 10^{-7} seconds), steady state rates and coverages with pseudo steady state approximation were calculated for very small conversions (X_{CO2}= 0.00005) using Equations (29) and (30).

$$\frac{d\theta_i}{dt} = \sum_j r_{ji} - r_{-ji} = 0 \tag{29}$$

$$\theta_v + \sum_i \theta_i = 1 \tag{30}$$

Feed compositions were again taken as 70 % H_2, 25 % CO, 5 % CO_2 and 70 % H_2, 24 % CO, 4 % CO_2, 2% H_2O.

3.4.4 Revealing Rate Determining Steps

In order to reveal any change in reaction mechanism and to find rate determining steps, the degree of rate control of each elementary step is calculated for different temperatures.

The concept of the degree of rate control of elementary steps is defined by Campbell et al. as in Equation (31) [103].

$$X_{rc,i} = (k_i/\delta k_i)*(\delta R/R) \tag{31}$$

By changing both forward and reverse rate constants (%5) for step i (in order not to disturb thermodynamics), change in overall rate, R, was observed while keeping other parameters constant. In this study, step 10 (methanol desorption step) is taken as the reference methanol formation step while changing other steps rate constants.

Campbell proposed that rate-limiting steps were those with positive degree of rate control and inhibition steps were those with negative degree of rate control.. The larger the numeric value of degree of rate control, $X_{rc,i}$, the bigger is the influence of its rate constant on the overall reaction rate.

CHAPTER 4

RESULTS AND DISCUSSION

4.1 Cu/ TiO_2 CATALYST CHARACTERIZATION RESULTS

4.1.1 BET Surface Area Measurements

BET surface areas were measured in order to investigate the relationship between surface area and photocatalytic activity. Measured BET surface areas for prepared photocatalysts are given in Table 4.1.

Table 4.1 BET surface areas of Cu/TiO_2 catalysts

	Catalyst	**Surface Area (m^2/ g)**
First Set Incipient wetness	Degussa P25	50
	1wt % Cu/ Degussa P25	42.9
	2wt % Cu/ Degussa P25	41.4
	3wt % Cu/ Degussa P25	41
Second Set Sol-Gel	1wt % Cu/TiO_2	18.4
	2wt % Cu/TiO_2	27.1
Third Set Sol-gel+surfactant	1wt % Cu/TiO_2	96
Fourth Set SolGel+Surfactant incipient wetness	TiO_2	77.7
	3wt % Cu/TiO_2	60.4

As it can be seen from Table 4.1, copper addition with incipient wetness method has caused a slight decrease in BET surface area from 50 m^2/g to 41 m^2/g.

Sol-gel prepared catalysts without surfactant (Second set of catalysts) had low surface areas, whereas, addition of surfactant and also titanium anatase nanopowder contributed to a three-fold increase in the surface area.

Apparently, longer mixing of the solution in fourth set of catalysts has not resulted in higher surface areas, on the contrary, decreased the surface area from 96 m^2/g (for 20 h of mixing) to 77.7 m^2/g (for TiO_2, 80 h of mixing). Also, addition of copper with incipient wetness method further decreased the surface area (60.4 m^2/g for 3 wt% Cu/ TiO_2).

4.1.2 XRD Analysis

XRD analysis was performed in order to investigate crystalline phases of TiO_2 and copper oxides. A representative 10 wt % Cu/TiO_2 catalyst was prepared via sol- gel method with surfactant in order to be able to see crystalline phases of copper. It was compared with bare TiO_2 (also prepared with surfactant and TiO_2 anatase nanopowder) in measurements (Figure 4.1).

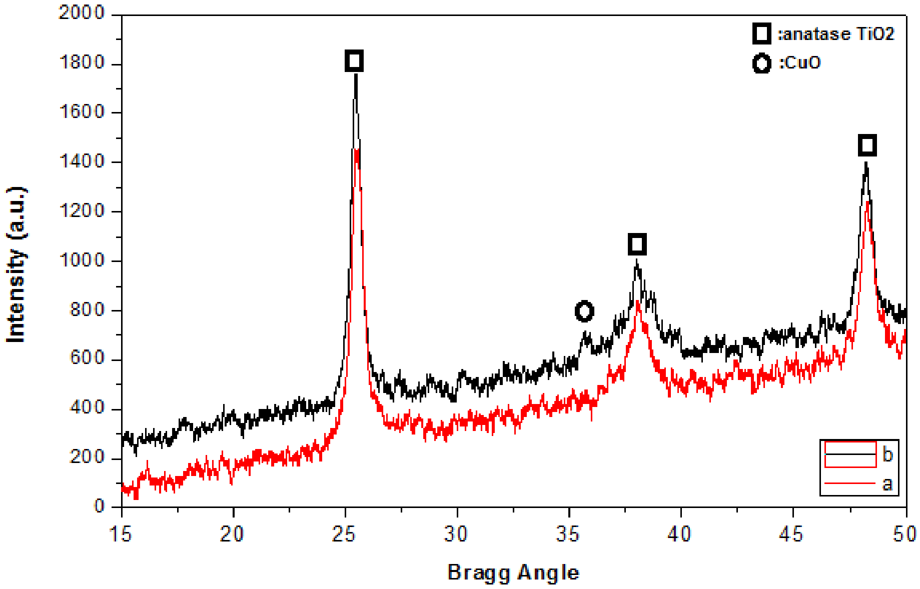

Figure 4.1 XRD analysis of a: TiO_2 and b: 10 wt %Cu/TiO_2, both prepared via sol-gel technique with surfactant and TiO_2 anatase nanopowder

Characteristic peaks of anatase (2θ = 25.3, 37.8 and 48) clearly belong to titanium anatase nanopowders and in 10 wt % Cu/TiO_2, a small peak at 2θ = 35.5 belongs to 002 crystalline phase of CuO [104].

4.1.3 TEM Measurements

TEM analysis was performed for 2 wt % Cu/Degussa P25 and sol-gel prepared 2 wt % Cu/TiO_2 catalysts (Figure 4.2 and 4.3). In Figure 4.2, TiO_2 Degussa P25 particles are seen with average particle diameter of 30 nm. Particles having diameters in the range of 14-16 nm belong to CuO particles having 0.34 nm lattice parameter, which were also confirmed by EDX. In Figure 4.3, sol-gel prepared catalyst showed very large particles of TiO_2 where copper particles cannot be distinguished due to preparation technique (due to addition of copper salt into the sol-gel mixture).

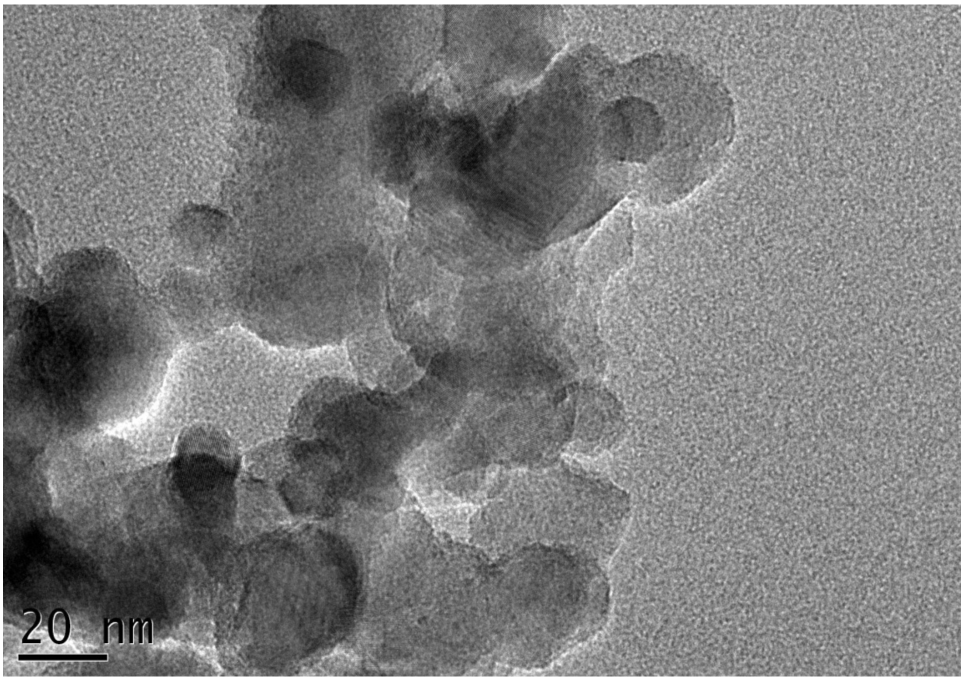

Figure 4.2 TEM image of 2 wt % Cu/ Degussa P25 prepared via incipient wetness method

Large particle sizes of catalyst may explain lower surface areas in sol-gel prepared, second set of catalysts. In sol-gel prepared samples, presence of copper-titanate is suggested with a lattice parameter of 0.77 nm which is in agreement with literature data; 0.74 nm , lattice parameter of calcium copper-titanate [105].

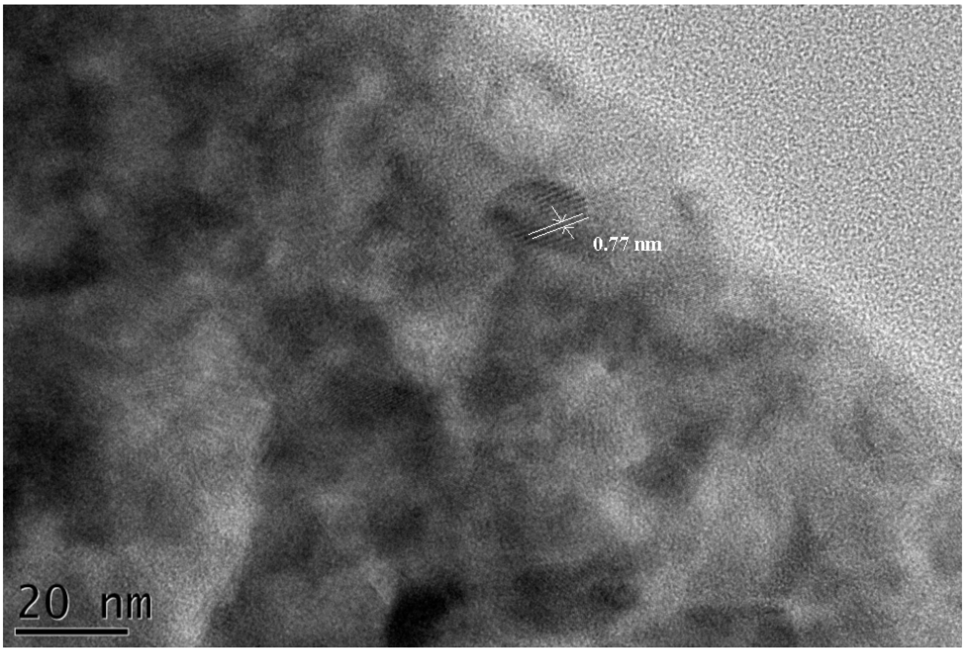

Figure 4.3 TEM image of 2 wt % Cu/TiO_2 prepared via sol- gel technique

4. 2 MASS TRANSFER LIMITATION EXPERIMENTS

Stirring rate and gas hold-up time experiments were conducted on photocatalytic hydrogen evolution from a water/ methanol mixture with Pt/ TiO_2 for revealing mass transfer limitation effects in gas – liquid – solid systems. Investigation of mass transfer limitations was performed with photocatalytic hydrogen evolution experiments since photocatalytic hydrogen evolution rates were reported to be much higher in literature than CO_2 reduction rates so that changes in rates resulted from reactor parameters can be easily followed. Tests were conducted with 250 ml deionized water and 2 ml methanol mixture with 0.25 g of catalyst. For gas hold-up time experiments, 62.5, 125, 187.5 and 250 ml of water was used with same catalyst and methanol concentrations.

4.2.1 Effect of Stirring Rates

Photocatalytic hydrogen evolution experiments with 0.5 wt % Pt / TiO_2 were performed at different stirring rates to investigate presence of mass transfer limitations in liquid media. Difference in photocatalytic rates can be seen in Figure 4.4.

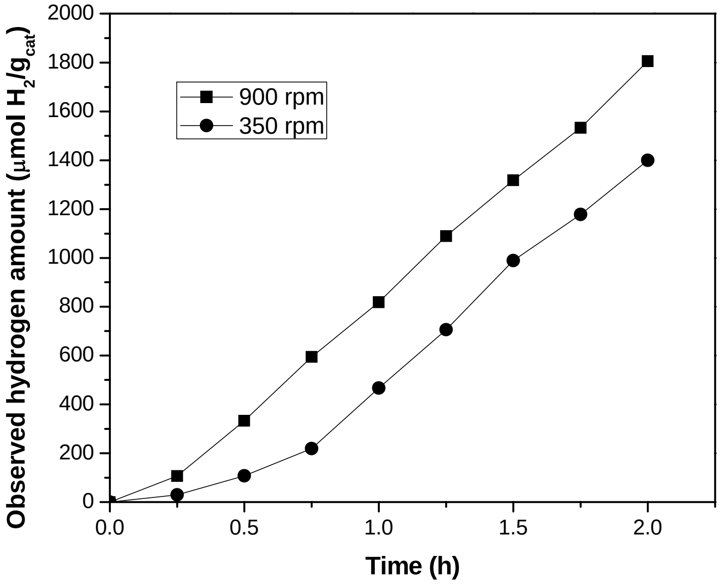

Figure 4.4 Effect of stirring rates on photocatalytic hydrogen evolution with 0.5 wt % Pt/TiO_2 in 250 ml of water and 2 ml of methanol (■) 900 rpm, (●) 350 rpm

Observed hydrogen amounts in the gas volume of the batch reactor showed difference for different stirring rates until they reached a specific hydrogen concentration (which is around 200 µmoles H_2/g_{cat}) in the gas phase. The difference in hydrogen evolution rates up to that concentration was attributed to the change in boundary layer thickness surrounding the catalyst particles, which is changing with stirring rates. As stirring rate increased, boundary layer thickness would probably decreased (Figure 4.5). Therefore increased product transport rate from catalyst surface to bulk liquid volume enhanced observed hydrogen production rates.

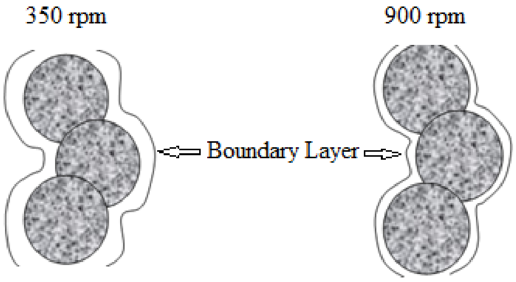

Figure 4.5 Decreasing boundary layer thickness with increasing stirring rates

A similar effect in photocatalytic CO_2 reduction tests realized in liquid media is expected at slow stirring rates. In case of such a mass transfer limitation due to a boundary layer, the diffusion rate of aqueous CO_2 molecules through bulk liquid volume and boundary layer could be limiting reaction rates.

In Figure 4.4, what was observed for hydrogen amounts is that, above that mentioned specific concentration, hydrogen amount in the gas volume has increased with the same rate for two different experiments. This could be explained by the rate determining role of gas-liquid equilibrium of the hydrogen. In a batch system comprised of three phases, produced hydrogen experiences different resistances such as desorption from the surface, mass transfer through the boundary layer, through the bulk liquid and through the gas-liquid interface (Figure 2.13). For this experiment, it was assumed that after hydrogen in the liquid volume reached a gas- liquid equilibrium (approximately at 15th minute for fast stirring rate and at 45th minute for slow stirring rate), the hydrogen accumulation rate in the gas phase is controlled with mass transfer rate of hydrogen at the gas- liquid interface.

4.2.2 Effect of Gas Hold-up Time

Photocatalytic hydrogen evolution reactions were performed with 0.5 wt % Pt/TiO_2 and with liquid volumes of 62.5, 125, 187.5 and 250 ml as they were explained in Section 3.3.1.

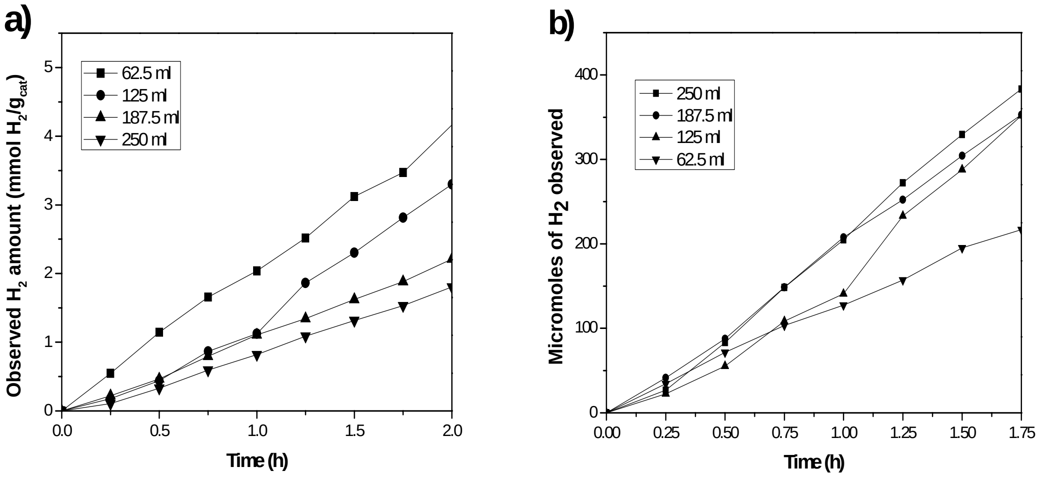

Figure 4.6 Effect of hydrogen hold-up time on photocatalytic hydrogen evolution amounts (a) normalized with respect to catalyst amount (b) not normalized with respect to catalyst amount, with CH_3OH/ H_2O: 1/125 (v/v) and C_{cat}: 1 g/L (■) 62.5 ml (●) 125 ml (▲) 187.5 ml (▼) 250 ml

In Figure 4.6 (a) the effect of the hydrogen hold-up time on normalized hydrogen evolution amounts with respect to the catalyst amount was plotted versus time, while in Figure 4.6 (b), the data was presented without normalizing to the catalyst amount. The data in Figure 4.6 (b) indicated that the evolved hydrogen amounts were independent of the catalyst amount. This clearly indicates the presence of mass transfer limitations at the gas- liquid interface. That is to say, even though hydrogen is produced and transferred to the liquid volume with different amounts, mass transfer limitation at the gas- liquid interface can be accounted for the reason of accumulation of hydrogen in the gas phase with same rates. Furthermore, hydrogen hold-up time experiments indicated that increased hold-up time of the product (hydrogen) in the liquid volume decreased the observed reaction rate. Longer the time spent by the products, higher the amount of hydrogen expected to react with other catalyst particles to give H_2O again.

In case of photocatalytic CO_2 reduction experiments, design of a liquid phase reactor with suspended catalyst particles increase the chance of interaction of reduction products such as methanol and water (with much higher concentrations) on the catalyst surface. Even though methanol could diffuse through a boundary layer from the catalyst surface to the bulk volume, the probability of back oxidation with water molecules on a different catalyst particle still exists. This probability is non negligible considering the standard free energies of the two reactions:

$$CO_2 + 2H_2O \rightarrow CH_3OH + {}^{3}/_{2}\, O_2 \qquad \Delta G^0 = \frac{693.9\ kJ}{mol\ CO_2}$$

$$CH_3OH + H_2O \rightarrow CO_2 + 3H_2 \qquad \Delta G^0 = \frac{17.4\ kJ}{mol\ CH_3OH}$$

Therefore, in photocatalytic testing with suspensions of a catalyst, one should not forget the high probability of back oxidation reactions.

4.2.3 Effect of Temperature

Effect of temperature on photocatalytic hydrogen evolution reaction with 1 wt % Pt/TiO_2 and also with 1 wt % Cu/TiO_2 was investigated (Figure 4.7 and Figure 4.8). Hydrogen evolution reaction from a water/methanol mixture was again selected in order to better observe minor changes in production rates.

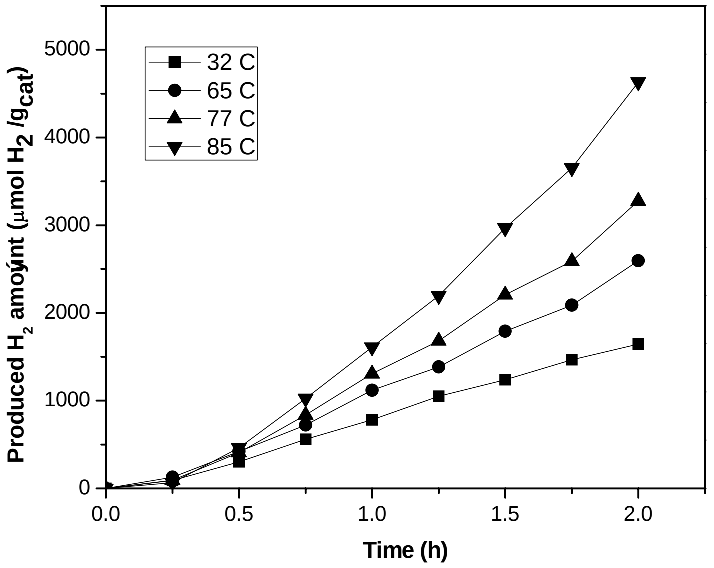

Figure 4.7 Effect of temperature on photocatalytic hydrogen evolution with 1 wt % Pt/TiO_2 in 250 ml water and 2 ml methanol (■) 32 °C (●) 65 °C (▲) 77 °C (▼) 85°C

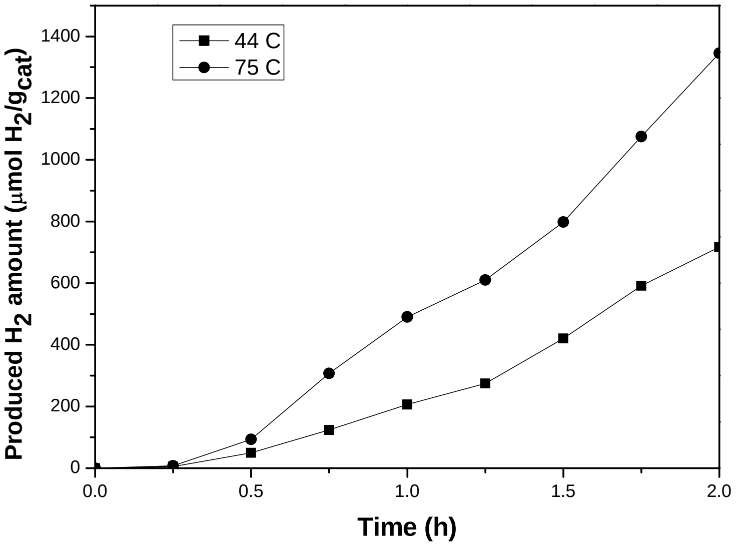

Figure 4.8 Effect of temperature on photocatalytic hydrogen evolution with 1 wt % Cu/TiO_2 in 250 ml water and 2 ml methanol (■) 44 °C (●) 75 °C

Table 4.2 Initial hydrogen evolution rates with changing temperature values

Temperature (°C)	**Catalyst**	**Hydrogen Evolution Rates (μmol H_2 *g_{cat}^{-1}* h^{-1})**
32	1 wt % Pt/ TiO_2	782
65	1 wt % Pt/ TiO_2	1058
77	1 wt % Pt/ TiO_2	1241
85	1 wt % Pt/ TiO_2	1563
44	1 wt % Cu/ TiO_2	296
75	1 wt % Cu/ TiO_2	573

As it can be seen from Table 4.2, photocatalytic hydrogen production with both Pt/TiO_2 and Cu/TiO_2 catalysts showed increased initial rates with increased temperature. Temperature sensitivity with Pt/TiO_2 catalyst was found to be respectively low when compared with catalytic temperature sensitivities. Apparent activation energy with Pt/ TiO_2 catalyst was found to be 12 kJ/mol (Figure 4.9) and 19.5 kJ/mol for Cu/TiO_2 catalyst.

Low activation energy barrier (8 kJ/mol) for water oxidation reaction was also reported by Hisatomi et al., relating the observed activation energy to trap hindered transport of photoexcited carriers [106]. However, in a study of Suzuki et al., activation energy of diffusion of dilute solvents in water was reported to be 16 kJ/mol, which is close to our observed activation energy values [107]. Based on the results presented in the previous sections and the results of the activation energy measurements, it is reasonable to say that the liquid phase photocatalytic hydrogen evolution reaction is mass transfer limited.

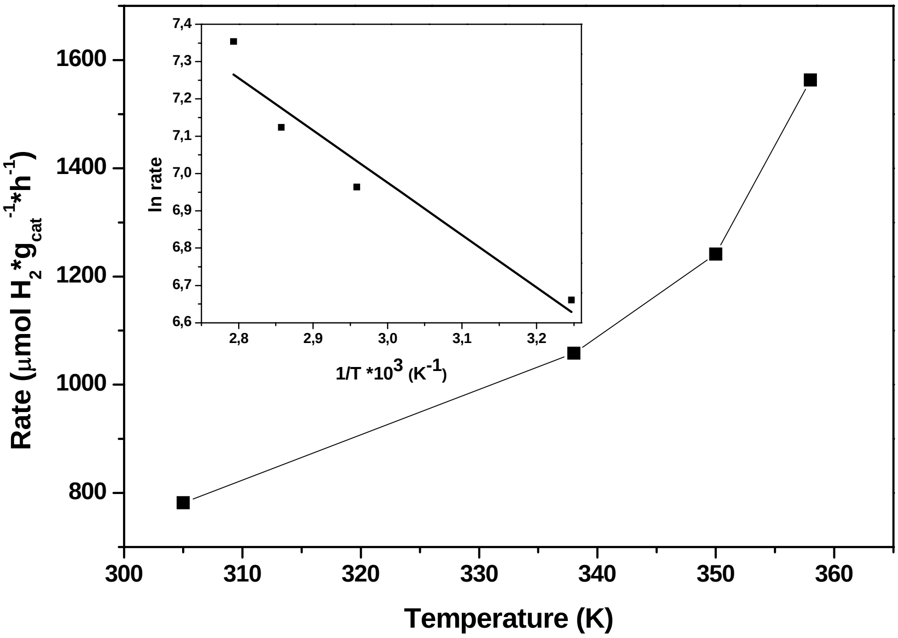

Figure 4.9 Effect of temperature on photocatalytic hydrogen evolution and ln rate vs 1/T demonstration with Pt/ TiO_2 catalyst

4.3 PHOTOCATALYTIC CO_2 REDUCTION ACTIVITY RESULTS

Four sets of Cu/TiO_2 catalysts were tested for CO_2 photo reduction in liquid media. Batch testing was performed with 300 ml deionized water and 0.3 g catalyst (with a catalyst concentration of 1 g/ L). In comparing the results of photocatalytic testing of the prepared catalysts, same conditions (such as temperature and stirring rates) and procedure were tried to be followed for a proper comparison. However, having proved the significant effect of slight changes in reaction conditions such as temperature or stirring rates on photocatalytic rates, one should not draw exact conclusions from this part of the study. This section is only to show the ability of reducing CO_2 photocatalytically at similar conditions as in literature.

4.3.1 Photocatalytic Testing of First Set of Catalysts

In Figure 4.10, methanol production amounts with respect to time are given for first set of catalysts which were prepared with incipient wetness method.

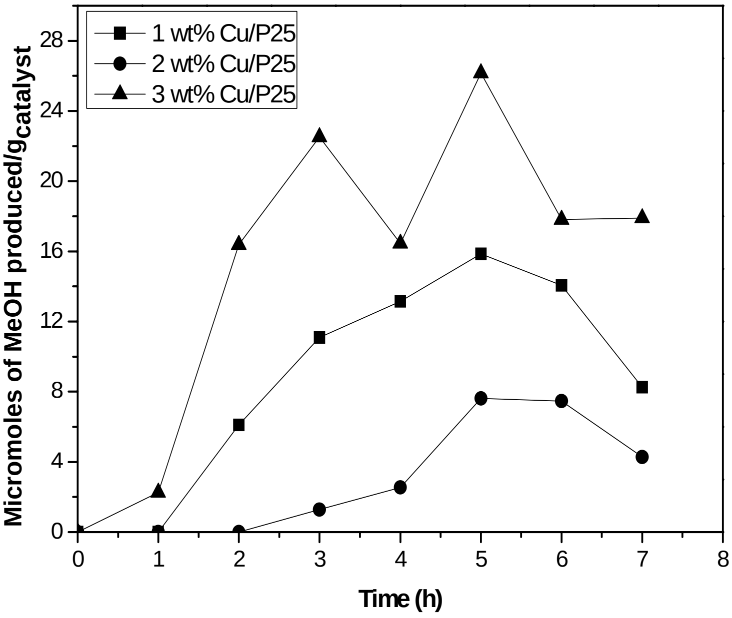

Figure 4.10 Photocatalytic methanol production amounts of first set of catalysts with respect to time

Among the catalysts prepared by incipient wetness method, 3 wt % Cu/ Degussa P25 has showed the highest photocatalytic activity. Methanol production amounts are 26 µmol/g$_{cat}$ for 3 wt % Cu/ Degussa P25, 15.9 µmol/g$_{cat}$ for 1 wt % Cu/ Degussa P25, and finally 7.6 µmol/g$_{cat}$ for 1 wt % Cu/ Degussa P25 after 5 hour of UV- illumination.

Instantaneous reaction rates related to above catalysts can be found in Figure 4.11. It can be inferred that firstly reaction rates increased slightly to a maximum and then started to decrease and finally became negative after fifth hour.

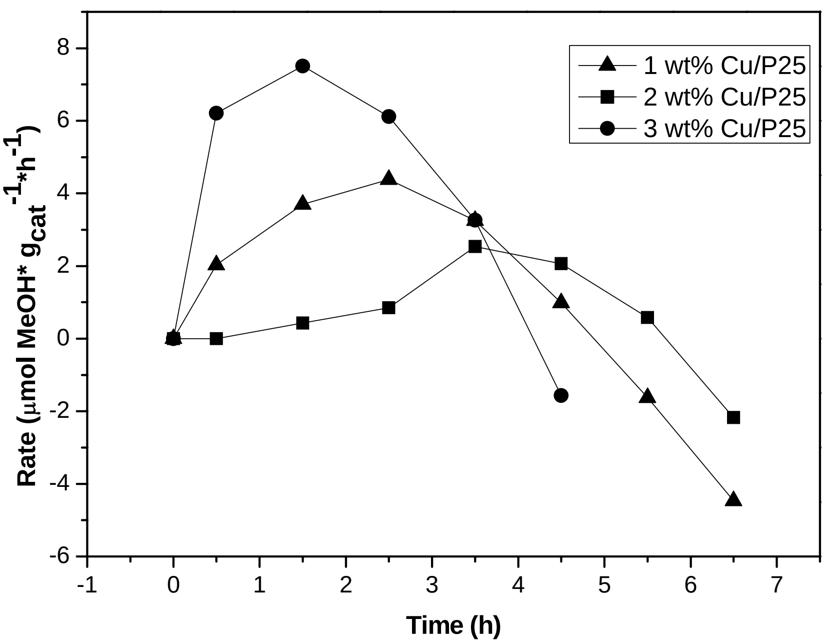

Figure 4.11 Reaction rates of first set of catalysts with respect to time

Decreasing reaction rates may indicate deactivation of the catalysts or reached equilibrium for a reversible reaction (see Figure 4.21). Another explanation can be the high hydrophilicity of the catalyst particles, saturation of the catalyst surface with excess concentration of water may lead to deactivation of the active sites.

Negative reaction rates may be resulted from back oxidation of methanol or realization of a series reaction which uses methanol as a reactant. Photocatalytic hydrogen evolution from water / methanol mixtures with Cu/ TiO_2 and Pt/ TiO_2 catalysts has been studied for a known time giving significant photocatalytic rates, reaching to the orders of 10000 µmoles*gcat^{-1}*h^{-1} [108]. In such a case, final products could be formic acid, formaldehyde as well as ethanol.

Photocatalytic activity did not increase with catalyst loading amounts accordingly as expected; 3 wt % Cu/ Degussa P25 catalyst showed the highest activity whereas 2 wt % Cu/ Degussa P25 catalyst showed the lowest. This result may indicate that particle sizes and dispersion of copper particles on TiO_2 Degussa P25 changes with different copper loading amounts.

In Table 4.3 calculated normalized rates and rates per gram of copper added can be seen for catalysts prepared with incipient wetness method. Highest rate per gram of copper was achieved with lowest copper loading; 1 wt % Cu/ Degussa P25 catalyst. This phenomenon can be explained by the findings that with higher metal loadings, a decrease in activity is observed because of agglomeration of metal particles on catalyst support; i.e., lower dispersions of metal particles. But again, one should keep in mind that minor changes in photocatalytic rates could be resulted from changing reaction conditions.

At the highest methanol amount in the liquid volume; i.e., 26 micromoles of methanol/gcat ~7.8 micromoles in 300 ml water, there is approximately 0.0005 micromoles of methanol in 50 ml of gas volume considering an ideal solution with vapor pressure of methanol 175 mmHg at 30 °C.

Table 4.3 Calculated rates for first set of catalysts

Photocatalyst	**Normalized Rates (μmol*$g_{cat}^{-1*}h^{-1}$)**	**Rate / g Cu (μmol H_2* g_{Cu}^{-1}*h^{-1})**
1 wt % Cu / Degussa P25	4.4	440
2 wt % Cu / Degussa P25	2.5	125
3 wt % Cu / Degussa P25	7.5	250

4.3.2 Photocatalytic Testing of Second Set of Catalysts

In Figure 4.12, methanol production amounts with respect to time are given for second set of catalysts which were prepared via sol-gel method.

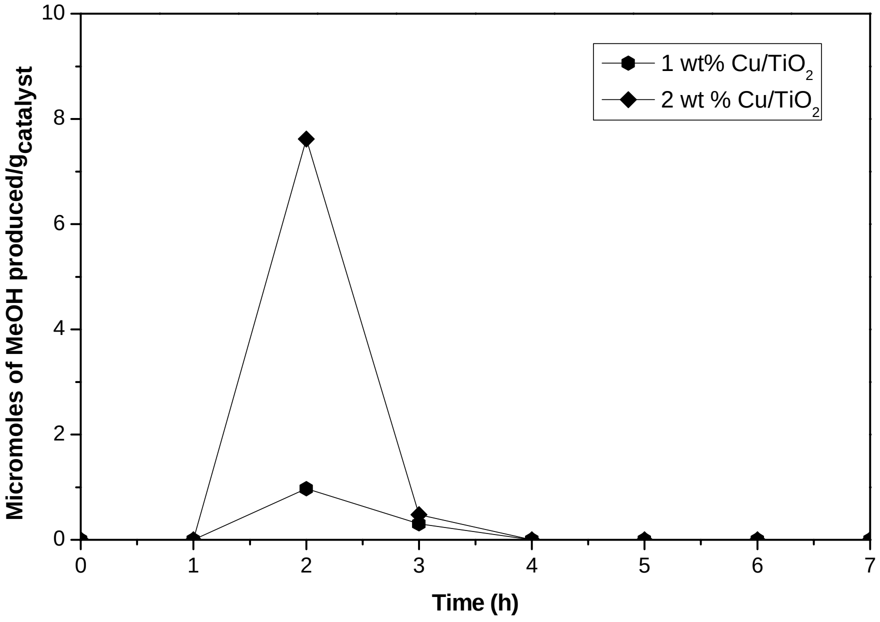

Figure 4.12 Photocatalytic methanol production amounts of second set of catalysts with respect to time

Sol-gel prepared catalysts produced very small amounts of methanol only at the second hour of the experiments. Low concentrations of methanol; with respect to those produced from first set of catalysts, may result from very low surface areas of those catalysts prepared with sol-gel method.

4.3.3 Photocatalytic Testing of Third Set of Catalysts

Third set of catalyst, 1 wt % Cu/TiO_2, showed negligible activity during seven hour of UV illumination. 1 wt % Cu/TiO_2 was prepared with sol-gel technique with the addition of surfactant and also titanium dioxide anatase nanoparticles. BET surface area of that catalyst was found to be 96 m^2/g, which was reasonably high than second set of catalysts. From that result, it can be inferred that surface area is not directly related to photocatalytic activity.

Surface copper/titanium ratios were found too high for second and third set of catalysts in which copper source was added to the sol-gel mixture (Appendix C). Not forgetting the importance of surface structure of copper and titanium dioxide, and their arrangements on surface for better interpreting surface activity, one can suggest inefficient light activation of TiO_2 semiconductor catalyst for sol-gel prepared catalysts due to excess amount of copper on surface.

4.3.4 Photocatalytic Testing of Fourth Set of Catalysts

Fourth set of catalyst, 3 wt % Cu/TiO_2 was prepared with incipient wetness impregnated copper onto bare TiO_2 prepared via sol-gel technique with surfactant and titanium dioxide anatase powder. In Figure 4.13, methanol production amounts of 3 wt % Cu/ TiO_2 catalyst from fourth set and also 3 wt % Cu/ Degussa P25 catalyst from first set were compared.

Photocatalytically produced methanol concentrations in batch testing of fourth set 3 wt % Cu/ TiO_2 showed overlapping results with 3 wt % Cu/ Degussa P25. That result emphasizes the importance of the presence and availability of the metal particles on the surface. In the preparation of the third set of catalyst; 1 wt % Cu/ TiO_2, copper was added to the sol-gel mixture; however, in fourth set of catalysts; 3 wt % Cu/TiO_2, incipient wetness addition of copper clearly resulted in proper distribution of copper (II) oxide sites on sol-gel prepared TiO_2, which enhanced the photocatalytic activity. Also, since the surface area of the fourth catalyst was measured to be smaller than third set of catalyst, it can be again stated that surface area does not directly affect the activity. In Figure 4.14, instantaneous reaction rates were compared for the mentioned catalysts. Decrease in rates and negative rates were again observed for 3 wt % Cu/ TiO_2 catalyst.

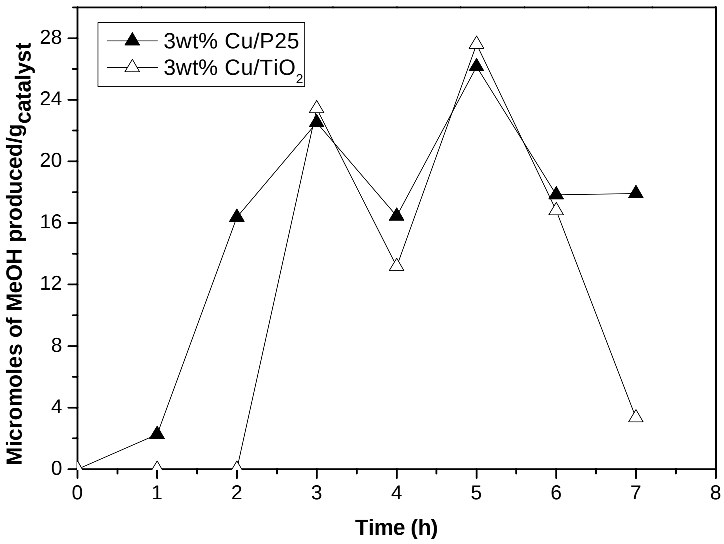

Figure 4.13 Photocatalytic methanol production amounts of 3 wt % Cu/ Degussa P25 and 3 wt % Cu/ TiO$_2$ (prepared by incipient wetness addition of copper on sol-gel prepared titania)

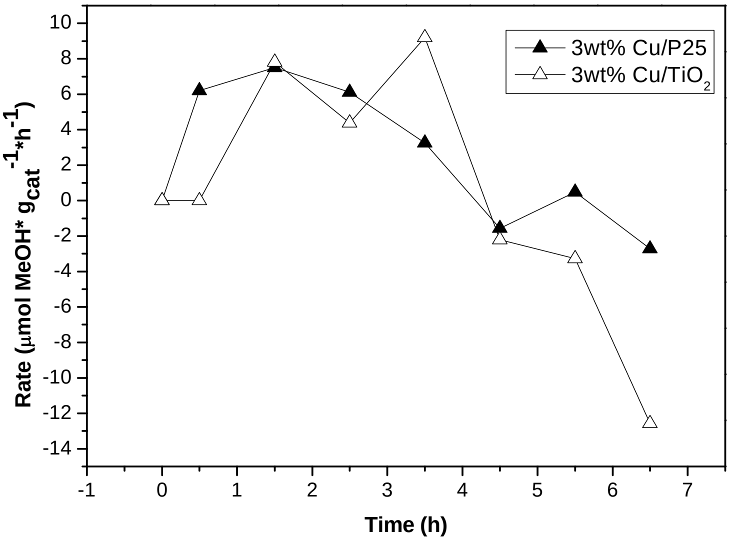

Figure 4.14 Comparison of reaction rates of first set 3 wt % Cu/Degussa P25 and fourth set 3 wt % Cu/TiO$_2$ with respect to time

4.3.5 Comparison of Results with Literature Results

In Table 4.4 initial methanol production rates of this study is given together with some literature results.

Table 4.4 Initial methanol production rates for tested catalysts

Photocatalyst	**Normalized Rates (μmol*$g_{cat}^{-1*}h^{-1}$)**
1 wt % Cu / Degussa P25 (This study)	4.4
2 wt % Cu / Degussa P25(This study)	2.5
3 wt % Cu / Degussa P25(This study)	7.5
3 wt % Cu / TiO_2(This study)	7.8
2 wt % Cu/ Degussa P25, 0.2 N NaOH[15]	10
2 wt % Cu / TiO_2, 0.2 N NaOH[15]	19.7
3.3 wt % Cu/ TiO_2, 0.2 N NaOH[15]	14.9

Photocatalytic CO_2 reduction rates obtained from this study is compared with those obtained under similar conditions. Tseng et al reported that Cu/ TiO_2 photocatalysts those were prepared with sol-gel method gave better activities than those prepared with incipient wetness method. They also added that CO_2 could not be reduced at solutions having pH 7.

In this study, it was seen that CO_2 could be reduced at pH 7 with comparable photocatalytic CO_2 reduction rates with those obtained in literature at pH 13.

Of course, one should always keep in mind that, comparison of the CO_2 reduction results with the literature results always brings the possibility of drawing misleading conclusions due to presence of mentioned mass transfer effects. In fact, very close photocatalytic CO_2 reduction results given in Table 4.4

indicate presence of probable mass transfer limitation effects which hinders acquisition of real kinetic data from those experiments.

4.4 KINETIC AND MICROKINETIC ANALYSIS

The results presented so far indicated very low photocatalytic methanol formation amounts. Thus, it is necessary to reveal the ‘Photocatalytic’ effect by comparing with the rates of industrial processes at ambient conditions. Since the data at such conditions are not available, then the comparison was solely based on the kinetic models which are vastly available for methanol synthesis over copper based catalysts in literature.

In the performed kinetic and microkinetic analysis of methanol synthesis at ambient conditions, effect of TiO_2 on methanol formation mechanism was not taken into consideration since the used models were proposed for metallic copper surfaces.

4.4.1 Catalytic Methanol Formation Rates Calculated with the Kinetic Model of Vanden Bussche et al. [95]

Initial formation rates of methanol from CO_2 hydrogenation and water gas shift reaction were calculated for a packed bed reactor (see Section 3.4.1). Results for two different feed compositions; without initial water (5% CO_2, 25 % CO, 70 % H_2) and with some amount of water (2 % H_2O, 4% CO_2, 24 % CO, 70 % H_2) with a total molar flow rate of 0.27 mol/s can be seen in Table 4.5 and Table 4.6.

Table 4.5 Initial methanol formation rates (in mol/gcat/s) with F_{CO20} = 0.0135 mol/s, F_{CO0}= 0.0675 mol/s, F_{H20}= 0.189 mol/s

Temperature	**Pressure (bar)**			
(K)	**2**	**15**	**50**	**75**
523		$7.66*10^{-6}$	$3.80*10^{-5}$	$5.07*10^{-5}$
453	$5.57*10^{-7}$	$8.88*10^{-7}$	$8.05*10^{-7}$	$7.67*10^{-7}$
423	$1.75*10^{-7}$	$1.04*10^{-7}$	$7.94*10^{-8}$	$7.84*10^{-8}$
400	$4.10*10^{-8}$	$2.32*10^{-8}$	$2.05*10^{-8}$	$1.63*10^{-8}$
393	$2.52*10^{-8}$	$1.74*10^{-8}$	$1.23*10^{-8}$	$9.68*10^{-9}$
353	$1.45*10^{-9}$	$9.59*10^{-10}$	$6.45*10^{-10}$	$5.83*10^{-10}$
323	$1.04*10^{-10}$	$6.31*10^{-11}$	$4.66*10^{-11}$	$4.22*10^{-11}$
300	$9.51*10^{-12}$	$5.75*10^{-12}$	$4.25*10^{-12}$	$3.84*10^{-12}$

Table 4.6 Initial methanol formation rates (in mol/gcat/s) with F_{CO20} = 0.0108 mol/s, F_{CO0}= 0.0648 mol/s, F_{H20}= 0.189 mol/s, F_{H2O0}= 0.0054 mol/s

Temperature	**Pressure (bar)**			
(K)	**2**	**15**	**50**	**75**
523	$1.61*10^{-7}$	$8.61*10^{-6}$	$3.57*10^{-5}$	$4.8*10^{-5}$
453	$7.59*10^{-9}$	$1.99*10^{-9}$	$6.70*10^{-10}$	$4.57*10^{-10}$
423	$2.11*10^{-11}$	$3.02*10^{-12}$	$9.16*10^{-13}$	$6.04*10^{-13}$
400	$9.32*10^{-14}$	$1.26*10^{-14}$	$3.77*10^{-15}$	$2.52*10^{-15}$
393	$1.55*10^{-14}$	$2.08*10^{-15}$	$6.26*10^{-16}$	$4.17*10^{-16}$
353	$1.38*10^{-19}$	$1.84*10^{-20}$	$5.51*10^{-21}$	$3.67*10^{-21}$
323	$3.36*10^{-24}$	$4.47*10^{-25}$	$1.34*10^{-25}$	$8.95*10^{-26}$
300	$2.31*10^{-28}$	$3.08*10^{-29}$	$9.25*10^{-30}$	$6.17*10^{-30}$

Calculated initial methanol formation rates seem to be in agreement with literature data. A methanol formation rate of $6.11*10^{-5}$ mol/gcat/s was found with a differential reactor at 523 K and 45 bar without initial water concentration [87].

Although at high temperatures such as 523 K, initial water concentration did not alter methanol formation rates significantly, as temperature decreases, inhibitory effect of water on methanol formation rates is substantial. Another interesting point is that, at lower temperatures, increasing pressure affects the methanol formation rates in an unexpected way; i.e., decreasing the methanol formation rates. This phenomenon is also observed with the kinetic modeling of Ovesen et al. [98].

4.4.2 Catalytic Methanol Formation Rates Calculated with the Static Kinetic Model Proposed by Ovesen et al. [98]

In this static kinetic model, again rate determining steps were determined in order to find the rate expressions. Parameters used in kinetic model were either obtained from gas phase experiments or surface science studies. In calculation of equilibrium constants of elementary steps, molecular partition functions were used. Molecular partition function values, calculated from the given thermodynamic data (Table 3.3) by Ovesen et al. are given in Table 4.7. Equations used in partition function calculations can be seen in Section 3.4.2.

Table 4.7 Translational (z_t), vibrational (z_v) and rotational (z_r) partition functions for species involved in methanol synthesis mechanism (T= 523K)

Species	z_t	z_v	z_r	z
H*	$2.05*10^{-2}$	1	1	$2.05*10^{-2}$
H_2 (g)	$4.52*10^{5}$	$2.33*10^{-3}$	2.98	$3.14*10^{3}$
O*	$3.86*10^{-1}$	1	1	$3.86*10^{-1}$
OH*	69.5	$9.55*10^{-3}$	$2.23*10^{-1}$	$1.48*10^{-1}$
HCOO*	111	$4.94*10^{-6}$	$6.45*10^{-1}$	$3.54*10^{-4}$
H_2COO*	125	$7.16*10^{-9}$	$6.45*10^{-1}$	$5.77*10^{-7}$
CH_3O*	83.2	$1.88*10^{-10}$	$9.10*10^{-1}$	$1.43*10^{-8}$
CO_2 (g)	$4.67*10^{7}$	$3.03*10^{-3}$	$4.66*10^{2}$	$6.59*10^{7}$
CO_2*	115	$3.03*10^{-3}$	$7.81*10^{2}$	$2.73*10^{2}$
CO (g)	$2.37*10^{7}$	$5.06*10^{-2}$	$1.88*10^{2}$	$2.26*10^{8}$
CO*	234	$5.66*10^{-2}$	1.82	$2.41*10^{1}$
CH_3OH(g)	$2.90*10^{7}$	$3.75*10^{-11}$	$2.47*10^{3}$	2.68
CH_3OH*	124	$2.44*10^{-13}$	$9.10*10^{-1}$	$2.75*10^{-11}$
H_2O (g)	$1.22*10^{7}$	$4.19*10^{-6}$	99.37	$5.09*10^{3}$
H_2O*	42.3	$1.05*10^{-5}$	$6.98*10^{-2}$	$3.10*10^{-5}$

Equilibrium constants of the reaction steps were calculated to result in below equations with the partition function values reported above.

$K_1 = 5.56*10^{-9} \exp(57000/RT)$

$K_2 = 117.8 \exp(-12300/RT)$

$K_3 = 4.37*10^{-5} \exp(-2800/RT)$

$K_4 = 5.34*10^{-2} \exp(-25100/RT)$

$K_5 = 8.06*10^{6} \exp(-46400/RT)$

$K_6 = 8*10^{-8} \exp(53900/RT)$

$K_7 = 17 \exp(30400/RT)$

$K_8 = 2.44*10^5 \exp(-27300/RT)$

$K_9 = 1.65*10^{-4} \exp(51700/RT)$

$K_{10} = 0.814 \exp(-25400/RT)$

$K_{11} = 6.22 \exp(-64900/RT)$

$K_{12}= 1.27*10^{-2} \exp(72600/RT)$

$K_{13}= 4.53*10^8 \exp(-70500/RT)$

From the kinetic model described in Section 3.4.2 and a similar packed bed reactor with same feed molar flow rates, initial methanol formation rates were calculated as in Table 4.8.

Table 4.8 Initial Initial methanol formation rates (mol/gcat/s) with F_{CO20} = 0.0108 mol/s, F_{CO0}= 0.0648 mol/s, F_{H20}= 0.189 mol/s and F_{H2O0}= 0.0054 mol/s

Temperature (K)	**Pressure (bar)**			
	2	**15**	**50**	**75**
523	$3.83*10^{-8}$	$4.04*10^{-6}$	$4.73*10^{-5}$	$9.78*10^{-5}$
453	$7.16*10^{-9}$	$3.36*10^{-7}$	$1.27*10^{-6}$	$1.63*10^{-6}$
423	$2.26*10^{-9}$	$3.33*10^{-8}$	$5.03*10^{-8}$	$5.01*10^{-8}$
400	$5.32*10^{-10}$	$1.88*10^{-9}$	$1.61*10^{-9}$	$1.43*10^{-9}$
393	$2.82*10^{-10}$	$6.33*10^{-10}$	$4.84*10^{-10}$	$4.2*10^{-10}$
353	$5.04*10^{-13}$	$2.37*10^{-13}$	$1.37*10^{-13}$	$1.12*10^{-13}$
323	$3.10*10^{-16}$	$1.18*10^{-16}$	$6.51*10^{-17}$	$5.31*10^{-17}$
300	$3.15*10^{-19}$	$1.61*10^{-19}$	$6.37*10^{-20}$	$5.20*10^{-20}$

From calculated kinetics, it was seen that water concentration drops due to higher kinetics of water gas shift reaction, therefore water was added to inlet gas composition as 2% of inlet gas making initial gas composition as: 70 % H_2, 24 % CO, 4 % CO_2 and 2 % H_2O.

It can be said for initial methanol rates that, for temperatures greater than 400 K, pressure has a positive effect on rates, nevertheless, for temperatures below 400 K, increasing pressure leads to a decrease in rates. A similar trend was observed for the rates calculated with Vanden Bussche and Froment kinetic model [95]. This may be due to increasing formate (HCOO*) coverage at low temperatures, which is said to be the abundant species for temperatures below 500 K by blocking free sites [99].

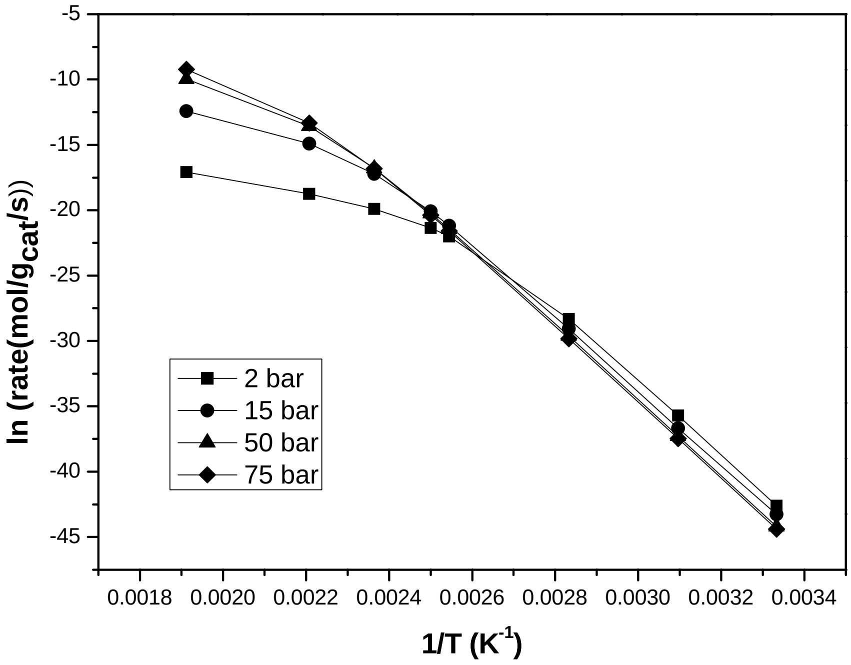

Figure 4.15 Demonstration of calculated rates in ln rate vs 1/T scale.

For temperatures below 393 K, same activation energy value, 240 kJ/mole is found for all pressure values. For temperatures above 393 K, found activation energy values vary between 60 kJ/mol and 100 kJ/mol, which is consistent with the values found by Askgaard et al. [99].

4.4.3 Microkinetic Modeling of CO_2 Hydrogenation using Finite Difference Method and Pseudo Steady State Approximation

Majority of the methanol formation kinetic models and their rate determining steps were based on the experimental data obtained at temperature ranges between 450 K and 580 K. Observed unexpected behaviors in calculated rates for low temperatures could be attributed to limitedness of the kinetic models to high temperatures. In order to obtain reasonable methanol formation rates at low temperatures also, a microkinetic modeling whose details can be found in Section 3.4.3 was performed. Calculated activation energy barriers and pre-exponential factors for each elementary step can be found in Table 4.9.

Table 4.9 Calculated activation energy barriers and pre exponential factors in microkinetic modeling

$k_f= A_f*exp(-E_{af}/RT)$		**Reactions**	**$k_r= A_r*exp(-E_{ar}/RT)$**	
A_f	E_{af} (kJ/mol)		A_r	E_{ar} (kJ/mol)
$6.77*10^{5}$	0	$H_2 +* \leftrightarrow H_2 *$	$6*10^{12}$	21
$1*10^{13}$	52.5	$H_2 * + * \leftrightarrow 2H *$	$8.55*10^{12}$	64.5
$1*10^{6}$	0	$CO_2 +* \leftrightarrow CO_2 *$	$1.62*10^{13}$	21
$1*10^{6}$	0	$CO +* \leftrightarrow CO *$	$8.86*10^{14}$	50
$1*10^{13}$	44.8	$CO * +O * \leftrightarrow CO_2 * + *$	$2.38*10^{13}$	115.8
$1*10^{13}$	14	$CO_2 * +H * \leftrightarrow HCOO * + *$	$1.79*10^{11}$	6
$1*10^{13}$	79	$HCOO * +H * \leftrightarrow H_2CO * +O *$	$1*10^{13}$	0
$1*10^{13}$	15.5	$H_2CO * +H * \leftrightarrow H_3CO * + *$	$1*10^{13}$	36.5
$1*10^{13}$	41	$H_3CO * +H * \leftrightarrow H_3COH * + *$	$1.06*10^{14}$	75
$9*10^{16}$	63	$CH_3OH * \leftrightarrow CH_3OH +*$	$1*10^{6}$	0
$1*10^{13}$	86.8	$O * +H * \leftrightarrow OH * + *$	$5.31*10^{11}$	64.8
$1*10^{13}$	6	$OH * +H * \leftrightarrow H_2O * + *$	$9.78*10^{14}$	107
$1.59*10^{14}$	59	$H_2O * \leftrightarrow H_2O +*$	$1*10^{6}$	0

Thermodynamic consistency of the reaction parameters could be observed from Table 4.10.

Table 4.10 Entropy and Gibbs free energy values calculated for each step of reaction

	Reactions	**ΔS (J/mol/K)**	**ΔH (kJ/mol)**	**ΔG (kJ/mol)**
1	$H_2 + * \leftrightarrow H_2 *$	-133	-21	18.63
2	$H_2 * + * \leftrightarrow 2H *$	1.30	-12	-12.39
3	$CO_2 + * \leftrightarrow CO_2 *$	-138	-21	20.13
4	$CO + * \leftrightarrow CO *$	-171	-50	1.04
5	$CO * + O * \leftrightarrow CO_2 * + *$	-7.21	-71	-68.85
6	$CO_2 * + H * \leftrightarrow HCOO * + *$	33.4	8	-1.97
7	$HCOO * + H * \leftrightarrow H_2CO * + O *$	0	79	79
8	$H_2CO * + H * \leftrightarrow H_3CO * + *$	0	-21	-21
9	$H_3CO * + H * \leftrightarrow H_3COH * + *$	-19.6	-34	-28.16
10	$CH_3OH * \leftrightarrow CH_3OH + *$	210	63	0.508
11	$O * + H * \leftrightarrow OH * + *$	24.4	22	14.73
12	$OH * + H * \leftrightarrow H_2O * + *$	-38.1	-101	-89.65
13	$H_2O * \leftrightarrow H_2O + *$	157	59	12.21
T	$CO_2 + CO + 5H_2 \leftrightarrow 2CH_3OH + H_2O$		-137	-22.4

In the microkinetic analysis performed with finite difference method, surface intermediate coverages could be easily followed for very short time intervals. CO_2 and CO molecules showed a sharp saturation coverage which is responsible for the sharp decrease in vacant site coverage (Figure 4.16). Surface intermediates and H* species on the surface, on the other hand, showed a slow increase with progressing time (Figure 4.19 and 4.20).

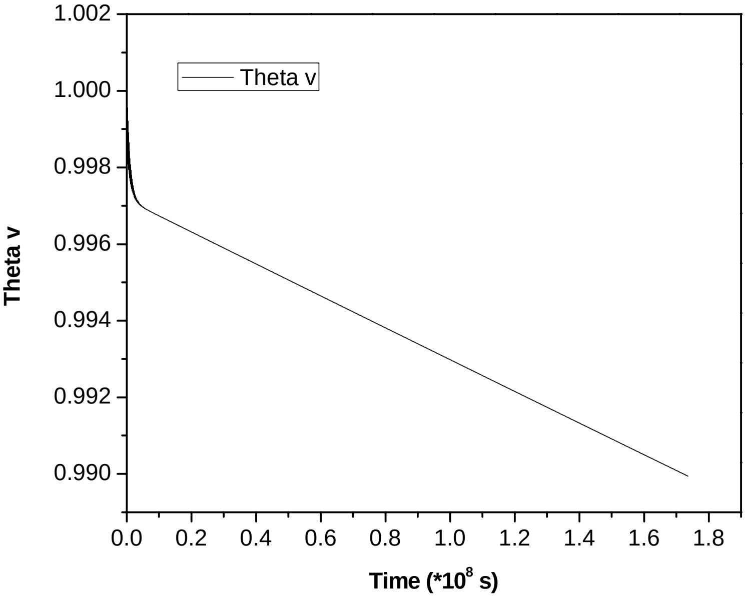

Figure 4.16 Vacant site coverage values with respect to time at 75 bar, 523 K on a Cu based catalyst

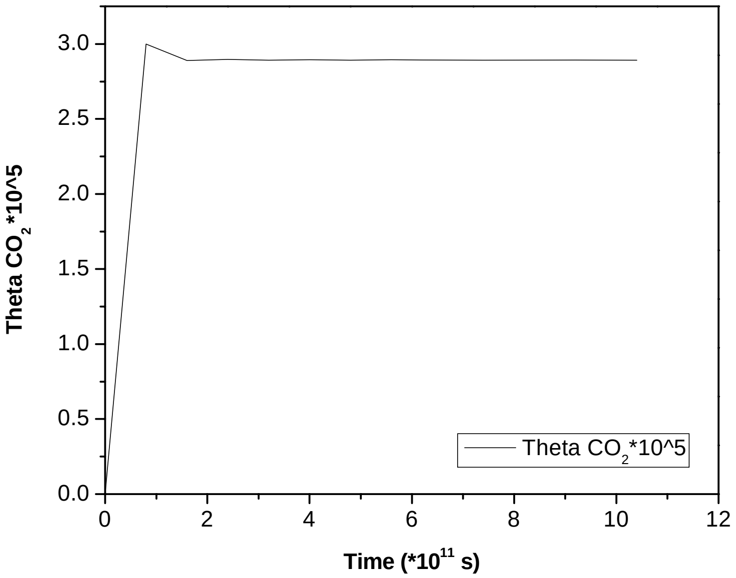

Figure 4.17 CO_2 coverage values with respect to time at 75 bar, 523 K

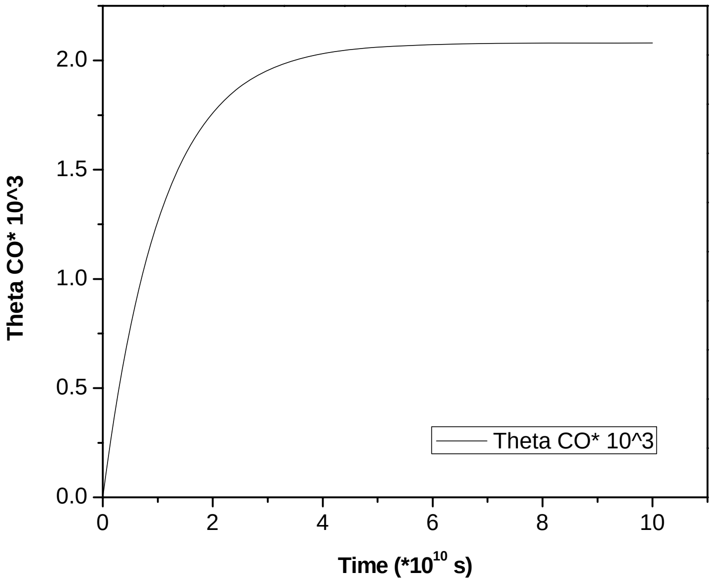

Figure 4.18 CO coverage values with respect to time at 75 bar, 523 K

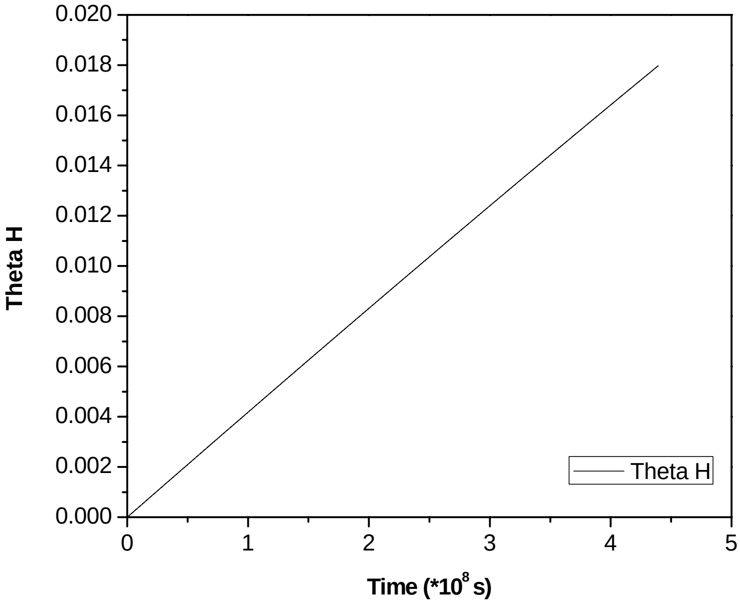

Figure 4.19 H coverage values with respect to time at 75 bar 523 K

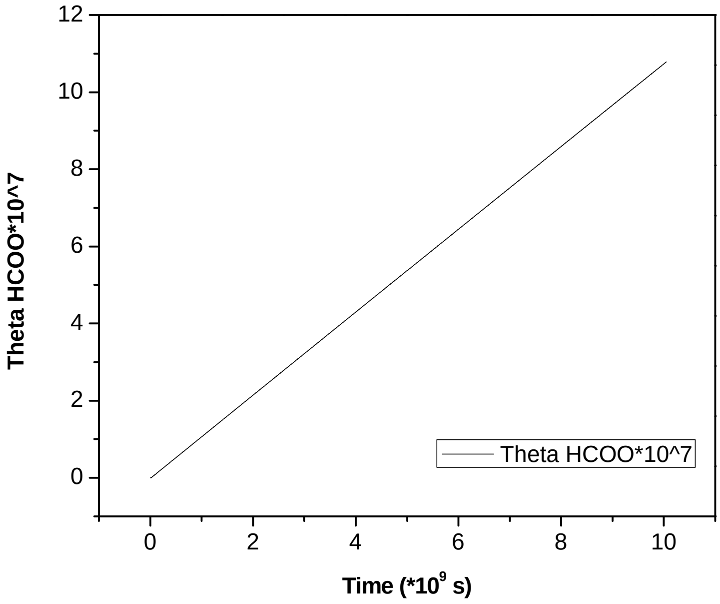

Figure 4.20 HCOO coverage values with respect to time at 75 bar, 523 K

With the pseudo steady state approximation, pseudo steady state values of coverages and methanol formation rates (of step 10:$CH_3OH *\leftrightarrow CH_3OH +*$) were calculated for initial gas compositions of 70 % H_2, 25 % CO, 5 % CO_2 and 70 % H_2, 24 % CO, 4 % CO_2, 2% H_2O and very small CO_2 conversions (X_{CO2} = 0.00005) as in Table 4.11.

Inhibitory effect of initial water concentration is clearly seen in net methanol formation rates. As it was in kinetic modeling of Vanden Bussche et al, inhibitory effect of water on methanol formation rates dominates at low temperatures; at which photocatalytic studies are conducted.

Inhibitory effect of water may also be seen in equilibrium CO_2 conversions and methanol formation constant rate curves (Figure 4.22) where CO_2 conversion was defined in Equation (32).

$$X_{CO2} = \frac{\xi_1 - \xi_2}{N_{CO20}} \tag{32}$$

For reactions:

1. $CO_2 + 3H_2 \leftrightarrow CH_3OH + H_2O$ and
2. $CO + H_2O \leftrightarrow CO_2 + H_2$

Table 4.11 Steady state surface concentrations and initial methanol formation rates (X_{CO2}= 0.00005) at 75 bar and initial gas composition: 70 % H_2, 25 % CO, 5 % CO_2 for r_{NET1} and coverages and 70 % H_2, 24 % CO, 4 % CO_2, 2% H_2O for r_{NET2}

T (K)	θ_{CO2}	θ_{CO}	θ_{H}	θ_{HCOO}	θ_{CH3OH}	θ_{V}	r_{NET1} (s^{-1})	r_{NET2} (s^{-1})
523	$2.6*10^{-5}$	$1.9*10^{-3}$	0.104	$2.7*10^{-5}$	$3.7*10^{-7}$	0.893	0.3378	0.267
453	$5*10^{-5}$	$1*10^{-2}$	0.172	$7*10^{-5}$	$3.2*10^{-6}$	0.818	0.0878	0.064
423	$6.9*10^{-5}$	$2.4*10^{-2}$	0.217	$1.1*10^{-4}$	$9.6*10^{-6}$	0.758	0.0407	0.025
393	$9.5*10^{-5}$	$6.2*10^{-2}$	0.272	$1.8*10^{-4}$	$3.3*10^{-5}$	0.664	$1.5*10^{-2}$	0.0059
353	$1.3*10^{-4}$	$2.3*10^{-1}$	0.321	$3.5*10^{-4}$	$2*10^{-4}$	0.442	$2.2*10^{-3}$	$1.7*10^{-4}$
323	$1.2*10^{-4}$	$5.3*10^{-1}$	0.254	$4.1*10^{-4}$	$6.7*10^{-4}$	0.207	$1.7*10^{-4}$	$2.2*10^{-6}$
300	$7.6*10^{-5}$	$7.8*10^{-1}$	0.142	$1.4*10^{-4}$	$1.4*10^{-3}$	0.073	$8.0*10^{-6}$	$3.4*10^{-8}$

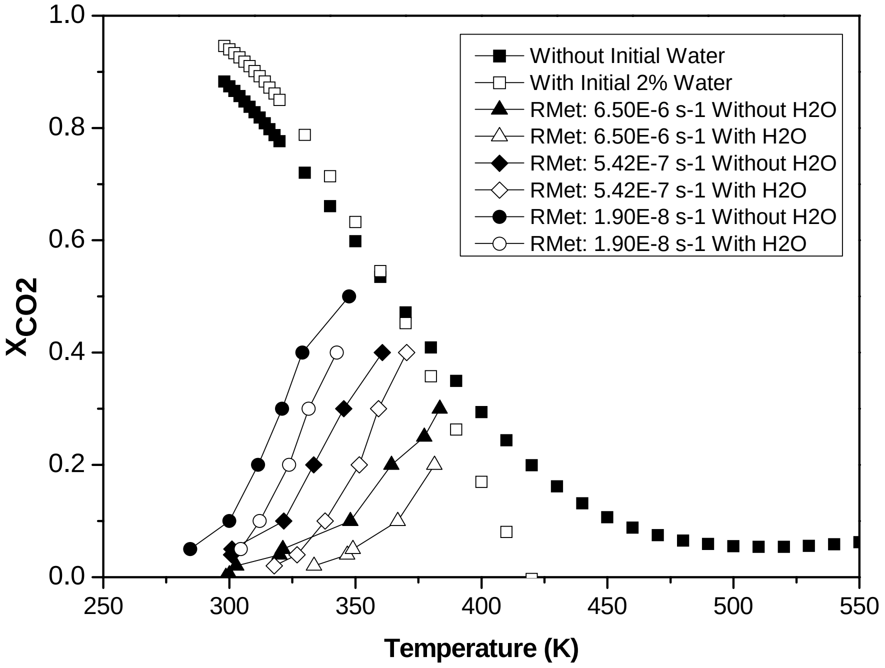

Figure 4.21 Equilibrium CO_2 conversion and constant rate conversion values at 75 bar. Constant rate curves were drawn for two cases, i. for 0 % initial H_2O concentration and ii. for 2 % initial H_2O concentration in the feed. Negative CO_2 conversion values are resulted from extra CO_2 production from water gas shift reaction in the presence of extra water.

Methanol formation rates with different kinetic and microkinetic models and at different reaction conditions are given in Table 4.12 in order to be able to compare methanol formation rates within the kinetic models and also with the photocatalytic rates.

Table 4.12 Methanol formation rates (mol/g_{cat}/s) at different reaction conditions found with different kinetic models and with or without initial water concentration

	Kinetic Models				
	Vanden Bussche et al. [95]		**Ovesen et al. [98]**	**Microkinetic Model**	
Reaction Conditions	**Without initial H_2O**	**With initial H_2O**	**With initial H_2O**	**Without initial H_2O**	**With initial H_2O**
523 K 75 bar	$5.1*10^{-5}$	$4.8*10^{-5}$	$9.78*10^{-5}$	$4.53*10^{-5}$	$3.58*10^{-5}$
300 K 75 bar	$3.84*10^{-12}$	$6.17*10^{-30}$	$5.2*10^{-20}$	$1.07*10^{-9}$	$4.58*10^{-12}$
300 K 1 bar	$1.13*10^{-11}$	$4.62*10^{-28}$	$3.55*10^{-19}$	$1.9*10^{-11}$	$2.07*10^{-12}$

With the microkinetic analysis, which is more sensitive to changes at low temperature, increasing effect of pressure on methanol production rates are observed as expected. This result may indicate necessity of high pressure photocatalytic systems in order to achieve higher methanol formation rates.

When the catalytic methanol formation rates were compared with photocatalytic rates, it is seen that at room conditions; i.e., at 300 K and 1 atm, photocatalytic rates (20 µmol/g_{cat}/h ~$6*10^{-9}$ mol/gcat/s [15]) significantly surpass catalytic rates ($2.07*10^{-12}$ mol/gcat/s). Even though estimation of kinetic parameters could contribute to non certainty of the kinetic results, it could be observed from the comparison that photo irradiation results in an obvious improvement in methanol formation rates. This improvement could be attributed to easier activation of molecules such as carbon dioxide through transfer of a photo-generated electron.

Rate determining steps in methanol synthesis reaction on copper based catalysts were investigated in the next section.

4.4.4 Rate Determining Step Investigation on Copper Based Catalysts

In order to find rate determining steps in methanol formation reaction, degree of rate control of each species were calculated at t= 5.18*10^{-7} s in finite difference method (Table 4.13) and at the pseudo steady state (Table 4.14).

Table 4.13 The degree of rate control values with respect to r$_f$10 ($CH_3OH * \leftrightarrow CH_3OH +*$) found by finite difference method at t= 5.18*10^{-7} s

	Elementary reactions	**$X_{rc,i}$**			
		75 atm 523 K	***75 atm 423 K***	***75 atm 300 K***	***1 atm 300K***
1	$H_2 +* \leftrightarrow H_2 *$	~0	0	0	0
2	$H_2 * + * \leftrightarrow 2H *$	0.36	2.4	3.53	3.7
3	$CO_2 +* \leftrightarrow CO_2 *$	0	0	~0	0
4	$CO +* \leftrightarrow CO *$	0	0	-3.67	-0.21
5	$CO * +O * \leftrightarrow CO_2 * + *$	0	0	0	0
6	$CO_2 * +H * \leftrightarrow HCOO * + *$	0	0	0	0
7	$HCOO * +H * \leftrightarrow H_2CO * +O *$	0.997	~1	~1	1
8	$H_2CO * +H * \leftrightarrow H_3CO * + *$	~0	~0	0.71	0.57
9	$H_3CO * +H * \leftrightarrow H_3COH * + *$	0	0.56	~1	1
10	$CH_3OH * \leftrightarrow CH_3OH +*$	-	-	-	-
11	$O * +H * \leftrightarrow OH * + *$	0	0	0	0
12	$OH * +H * \leftrightarrow H_2O * + *$	0	0	0	0
13	$H_2O * \leftrightarrow H_2O +*$	0	0	0	0

Table 4.14 The degree of rate control values with respect to r10net ($CH_3OH * \leftrightarrow CH_3OH + *$) found by steady state assumption at X_{CO2}=0.00005

	Elementary reactions	$X_{rc,i}$			
		75 atm 523 K	***75 atm 423 K***	***75 atm 300 K***	***1 atm 300K***
1	$H_2 + * \leftrightarrow H_2 *$	0	0	0	0
2	$H_2 * + * \leftrightarrow 2H *$	0	0	0	0
3	$CO_2 + * \leftrightarrow CO_2 *$	0	0	0	0
4	$CO + * \leftrightarrow CO *$	0	~0	~0	~0
5	$CO * + O * \leftrightarrow CO_2 * + *$	~0	~0	0	0
6	$CO_2 * + H * \leftrightarrow HCOO * + *$	0	0	0	0
7	$HCOO * + H * \leftrightarrow H_2CO * + O *$	0.97	0.993	~1	~1
8	$H_2CO * + H * \leftrightarrow H_3CO * + *$	0	0	0	0
9	$H_3CO * + H * \leftrightarrow H_3COH * + *$	~0	0	~0	~0
10	$CH_3OH * \leftrightarrow CH_3OH + *$	-	-	-	-
11	$O * + H * \leftrightarrow OH * + *$	0	0	0	0
12	$OH * + H * \leftrightarrow H_2O * + *$	0	0	0	0
13	$H_2O * \leftrightarrow H_2O + *$	0	0	0	0

Although degree of rate controls calculated for the pseudo steady state prevailed reaction Step 7 ($HCOO * + H * \leftrightarrow H_2CO * + O *$) to be the rate determining step for all conditions tried, at different time scales before steady state, Step 2 ($H_2 * + * \leftrightarrow 2H *$) is proven to be rate determining especially for low temperatures. This change in rate determining step from 7 to 2 as temperatures decreases, suggests the probability of a change in mechanism at lower temperatures.

As a matter of fact, rate determining role of H* molecules could also be observed from the comparison of coverages on catalyst surface. As CO and CO_2 molecules seem to be saturated on the surface as soon as 10^{-10}s (Figure 4.17 and

Figure 4.18), H molecules continue to accumulate on the surface slowly (Figure 4.19).

Therefore, one could suggest that the bottleneck of the reaction in photocatalytic CO_2 reduction mechanism could be the H supply to the catalyst surface, whose rates are already known to be slow since only source of H is the water oxidation reaction in photocatalytic CO_2 reduction mechanism.

In photocatalytic CO_2 reduction systems, utilization of H_2O as the reductant results in some consequences which can be said to be limiting the photocatalytic rates. The following factors are the observations and the outcomes of this study:

- As it was proved from kinetic and microkinetic modeling, water itself has an inhibitory effect on methanol formation rates on copper surfaces.
- Slow stirring rates of photocatalytic solutions together with the super hydrophilicity of TiO_2 surfaces contribute to a water boundary layer formation which complicates CO_2 diffusion to the surface.
- The presence of water molecules prevents or hinders activation of CO_2 in photocatalytic systems by interrupting the interaction between CO_2 molecules and catalyst surface and by also oxidizing oxygen deficiencies which are essential in CO_2 activation [83].
- Slow water oxidation rates on photocatalytic systems (in which back oxidation reaction was reported to have significant effect on observed slow hydrogen evolution rates) limits the H concentration on the catalyst surface which limits CO_2 reduction rates.

This result; i.e., discovery of the rate determining step to be the presence or rates of H supply in photocatalytic experiments supports the assertion of the presence of dark steps in photocatalysis so that CO_2 could be reduced with H molecules on copper/ metal surfaces catalytically.

CHAPTER 5

CONCLUSIONS

The aim of this study is to elucidate the role of operational parameters and to understand chemical details of photocatalytic carbon dioxide reduction reaction performed in liquid media.

The stirring rate and gas hold-up time experiments performed in a liquid phase photocatalytic system indicated probable interference of mass transfer rates in kinetic rates at three- phase photocatalytic systems, especially at the solid-liquid and gas- liquid interfaces. Also, gas hold-up time experiments performed in liquid suspension of photocatalysts revealed the probability of negative contribution of back oxidation reactions. Apparent activation energies of 12 and 19.5 kj/mol, found in photocatalytic hydrogen evolution experiments with 1 wt % Pt/ TiO_2 and 1 wt % Cu/TiO_2 catalysts, were attributed as solute diffusion activation energies in water, which also confirms the probability of mass transfer limitations in liquid media photocatalytic tests.

As a second part of this study, photocatalytic CO_2 reduction activities of Cu/ TiO_2 photocatalysts, prepared with sol-gel and incipient wetness methods, were tested in liquid media. BET surface area, XRD, TEM and XPS characterization analysis were performed. Metal addition with incipient wetness method showed the best results underlying the importance of the availability of the copper oxides on surface and also their size and dispersion rather than the surface area of the catalyst. All of the observed methanol formation rates showed a decrease after some point, reaching to negative values, indicating equilibrium and realization of back oxidation reactions.

Low methanol formation amounts observed with carbon dioxide reduction experiments led to the investigation of the rates of industrial processes at ambient conditions. Comparison of the industrial and photocatalytic methanol formation rates on copper surfaces indicated the significant effect of photo-irradiation in carbon dioxide activation at ambient conditions. But still, findings of the kinetic and microkinetic analysis such as inhibitory effect of water on methanol formation rates on copper surfaces is of importance, especially at ambient conditions. Kinetic and microkinetic analysis gave an opinion about the rate determining steps in CO_2 reduction. It was observed that $H_2 * + * \leftrightarrow 2H *$ step plays an important role especially at lower temperatures at which photocatalysis occurs. Therefore, for photocatalytic systems where carbon dioxide is reduced with water, the importance of the water oxidation rates were underlined since it is the only H* source. Results also indicated the probability of dark steps of CO_2 reduction with H molecules.

CHAPTER 6

RECOMMENDATIONS

One suggestion that could improve the present photocatalytic rates is the utilization of a gas circulation system in CO_2 reduction experiments. As mentioned in Section 4.3.2, different micromixing conditions could be achieved with a gas circulated batch system. Maximum mixedness achieved for water molecules in the system would improve the reaction kinetics as having a reaction order less than one in reaction rate. CO_2 circulation, on the other hand, would approach to segregated flow, which would also enhance the rates.

From the kinetic analysis, it was observed that methanol formation rates increase as pressure increase even at room temperatures. Photocatalytic systems could benefit from higher pressures in methanol synthesis likewise the photosynthesis which benefits from high osmotic pressures inside the plants.

Another suggestion that could be made for present photoreactors is the implementation of immobilized catalysts. Such kind of a system is believed to inhibit back oxidation reactions of the reaction products by preventing the encounter between products and other catalyst particles.

On the other hand, the gap between the photocatalytic and photosynthetic rates motivates designing a photocatalytic system similar to photosynthetic systems. In designing photocatalytic CO_2 reduction reactions, thermal contributions to the reaction mechanism as well as contribution of a special electron and proton transport process should be taken into consideration.

By mimicking the nature, one could design a photocatalytic/ catalytic reactor in such a way that in one compartment light is harvested by the semiconductor in order to split water to form H^+s and by the transfer of produced protons and electrons, CO_2 could be reduced catalytically with another catalyst, such as copper, in the other compartment. In this way, with the help of proton exchange membranes and separate reaction centers interaction between reactants or products and therefore reverse reactions could be prevented by supplying Hs to catalytic compartment at the same time. On the other hand, a high conductance electron membrane would prevent charge recombination (Figure 6.1). By this way one may approach photosynthetic rates which are 12000 times faster than current photocatalytic CO_2 reduction yields.

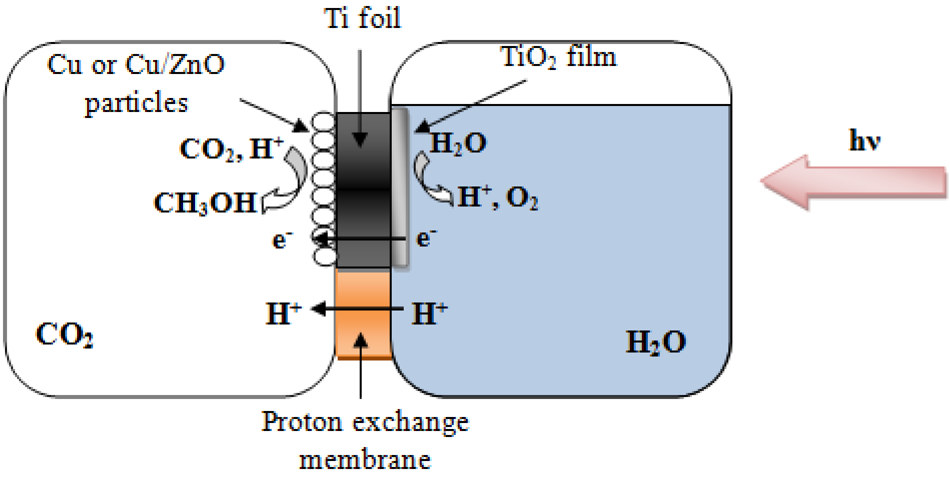

Figure 6.1 Schematic illustration of suggested reactor for CO_2 reduction

In literature, Kitano et al. reported separate hydrogen and oxygen evolution with an H-type glass container, in which water is splitted with titanium nanotubes on one chamber and hydrogen is evolved with Pt particles on the other chamber. The electrical connection was set with a nafion film [109]. Karslioglu studied and improved this H-type system for water splitting reaction with a proton exchange membrane and resulted in separate oxygen and hydrogen evolution in neutral media [110].

REFERENCES

[1] U.S. Department of Energy Office of Science Genomic Science Program, www.genomicscience.energy.gov/pubs/CarbonCycleFlyer_01-28-09.pdf, last visited in October 2010.

[2] International Energy Agency, www.iea.org/textbase/nppdf/free/2010/key_stats_2010.pdf, last visited in October 2010.

[3] Millward, A. R.; Yaghi, O. M. *Journal of the American Chemical Society* **2005**, *127*, 17998.

[4] Mikkelsen, M.; Jorgensen, M.; Krebs, F. C. *Energy & Environmental Science* **2010**, *3*, 43.

[5] Softpedia, news.softpedia.com/news/Photosynthesis-Denuded-41035.shtml, last visited in April 2010.

[6] Linsebigler, A. L.; Lu, G. Q.; Yates, J. T. *Chemical Reviews* **1995**, *95*, 735.

[7] Carp, O.; Huisman, C. L.; Reller, A. *Progress in Solid State Chemistry* **2004**, *32*, 33.

[8] Yamashita, H.; Nishiguchi, H.; Kamada, N.; Anpo, M.; Teraoka, Y.; Hatano, H.; Ehara, S.; Kikui, K.; Palmisano, L.; Sclafani, A.; Schiavello, M.; Fox, M. A. *Research on Chemical Intermediates* **1994**, *20*, 815.

[9] Anpo, M.; Yamashita, H.; Ichihashi, Y.; Ehara, S.; *Journal of Electroanalytical Chemistry* **1995** *396*, 21.

[10] Anpo, M.; Chiba, K., *Journal of Molecular Catalysis*, **1992**, *74*, 207.

[11] Hirano, K.; Inoue, K.; Yatsu, T. *Journal of Photochemistry and Photobiology a-Chemistry* **1992**, *64*, 255.

[12] Sayama, K.; Arakawa, H. *Journal of Physical Chemistry* **1993**, *97*, 531.

[13] Anpo, M.; Yamashita, H.; Ichihashi, Y.; Fujii, Y.; Honda, M. *Journal of Physical Chemistry B* **1997**, *101*, 2632.

[14] Anpo, M.; Yamashita, H.; Ikeue, K.; Fujii, Y.; Zhang, S. G.; Ichihashi, Y.; Park, D. R.; Suzuki, Y.; Koyano, K.; Tatsumi, T. *Catalysis Today* **1998**, *44*, 327.

[15] Tseng, I. H.; Chang, W. C.; Wu, J. C. S. *Applied Catalysis B-Environmental* **2002**, *37*, 37.

[16] Anpo, M.; Takeuchi, M.; *Journal of Catalysis* **2003**, *216*, 505.

[17] Yahaya, A. H.; Gondal, M. A.; Hameed, A. *Chemical Physics Letters* **2004**, *400*, 206.

[18] Wu, J. C. S.; Lin, H. M. *International Journal of Photoenergy* **2005**, *7*, 115.

[19] Ozcan, O.; Yukruk, F.; Akkaya, E. U.; Uner, D. *Applied Catalysis B-Environmental* **2007**, *71*, 291.

[20] Yang, H. C.; Lin, H. Y.; Chien, Y. S.; Wu, J. C. S.; Wu, H. H. *Catalysis Letters* **2009**, *131*, 381.

[21] Kaneco, S.; Kurimoto, H.; Ohta, K.; Mizuno, T.; Saji, A. *Journal of Photochemistry and Photobiology a-Chemistry* **1997**, *109*, 59.

[22] Sa, J.; Fernandez-Garcia, M.; Anderson, J. A. *Catalysis Communications* **2008**, *9*, 1991.

[23] Chen, L.; Graham, M. E.; Li, G. H.; Gentner, D. R.; Dimitrijevic, N. M.; Gray, K. A. *Thin Solid Films* **2009**, *517*, 5641.

[24] Woan, K.; Pyrgiotakis, G.; Sigmund, W. *Advanced Materials* **2009**, *21*, 2233.

[25] Yoneyama, H. *Catalysis Today* **1997**, *39*, 169.

[26] Ozcan, O.; Yukruk, F.; Akkaya, E. U.; Uner, D. *Topics in Catalysis* **2007**, *44*, 523.

[27] Asahi, R.; Morikawa, T.; Ohwaki, T.; Aoki, K.; Taga, Y. *Science* **2001**, *293*, 269.

[28] Ikeue, K.; Nozaki, S.; Ogawa, M.; Anpo, M. *Catalysis Today* **2002**, *74*, 241.

[29] Hwang, J. S.; Chang, J. S.; Park, S. E.; Ikeue, K.; Anpo, M. *Topics in Catalysis* **2005**, *35*, 311.

[30] Yamashita, H.; Fujii, Y.; Ichihashi, Y.; Zhang, S. G.; Ikeue, K.; Park, D. R.; Koyano, K.; Tatsumi, T.; Anpo, M. *Catalysis Today* **1998**, *45*, 221.

[31] Govindjee, Ed. *Bioenergetics of Photosynthesis*; Academic Press: New York, 1975.

[32] Hankamer, B.; Barber, J.; Boekema, E. J. *Annual Review of Plant Physiology and Plant Molecular Biology* **1997**, *48*, 643.

[33] Ananyev, G. M.; Zaltsman, L.; Vasko, C., Dismukes, G. C.; *Biochimica et Biophysica Acta* **2001**, *1503*, 52.

[34] Haumann, M.; Liebisch, P.; Muller, C.; Barra, M.; Grabolle, M.; Dau, H. *Science* **2005**, *310*, 1019.

[35] Meyer, T. J. *Nature* **2008**, *451*, 778.

[36] Rensselaer Polytechnic Institute, http://www.rpi.edu/dept/bcbp/molbiochem/MBWeb/mb2/part1/dark.htm, last visited in March 2011.

[37] Ke, B. Photosynthesis: *Photobiochemistry and Photobiophysics*; Kluwer Academic Publishers: Dordrecht, 2001; Vol. 10 of *Advances in Photosynthesis*.

[38] Whitmarsh, J.; Govindjee In *Concepts in Photobiology: Photosynthesis and Photomorphogenesis;* Singhal, G.S., Renger, G., Sopory, S. K., Irrgang, K. D., Govindjee, Eds.; Narosa Publishing House: New Delhi, 1999; Chapter 2.

[39] Heldt, H. W. *Plant Biochemistry*; Heldt, H. W., B. Piechulla, Eds.; Academic: London, 2010; 4th Edition.

[40] Whittingham, C. P. *The Mechanism of Photosynthesis*; American Elsevier Pub. Co: New York, 1974.

[41] Singal, H. R.; Talwar, G.; Dua, A.; Singh, R. *Journal of Biosciences* **1995**, *20*, 49.

[42] Schulte, K. L.; DeSario, P. A.; Gray, K. A. *Applied Catalysis B-Environmental* **2010**, *97*, 354.

[43] Inoue, T.; Fujishima, A.; Konishi, S.; Honda, K. *Nature* **1979**, *277*, 637.

[44] Dey, G. R.; Belapurkar, A. D.; Kishore, K. *Journal of Photochemistry and Photobiology a-Chemistry* **2004**, *163*, 503.

[45] Koci, K.; Obalova, L.; Matejova, L.; Placha, D.; Lacny, Z.; Jirkovsky, J.; Solcova, O. *Applied Catalysis B-Environmental* **2009**, *89*, 494.

[46] Kitano, M.; Matsuoka, M.; Ueshima, M.; Anpo, M. *Applied Catalysis a-General* **2007**, *325*, 1.

[47] Koci, K.; Mateju, K.; Obalova, L.; Krejcikova, S.; Lacny, Z.; Placha, D.; Capek, L.; Hospodkova, A.; Solcova, O. *Applied Catalysis B: Environmental* **2010**, *96*, 239.

[48] Kaneco, S.; Shimizu, Y.; Ohta, K.; Mizuno, T. *Journal of Photochemistry and Photobiology a-Chemistry* **1998**, *115*, 223.

[49] Zhang, Q. H.; Han, W. D.; Hong, Y. J.; Yu, J. G. *Catalysis Today* **2009**, *148*, 335.

[50] Solymosi, F.; Tombacz, I. *Catalysis Letters* **1994**, *27*, 61.

[51] Wang, C. J.; Thompson, R. L.; Baltrus, J.; Matranga, C. *Journal of Physical Chemistry Letters* **2010**, *1*, 48.

[52] Wang, Z. Y.; Chou, H. C.; Wu, J. C. S.; Tsai, D. P.; Mul, G. *Applied Catalysis a-General* **2010**, *380*, 172.

[53] Varghese, O. K.; Paulose, M.; LaTempa, T. J.; Grimes, C. A. *Nano Letters* **2009**, *9*, 731.

[54] Zhao, Z. H.; Fan, J. M.; Xie, M. M.; Wang, Z. Z. *Journal of Cleaner Production* **2009**, *17*, 1025.

[55] Lo, C. C.; Hung, C. H.; Yuan, C. S.; Wu, J. F. *Solar Energy Materials and Solar Cells* **2007**, *91*, 1765.

[56] Nishimura, A.; Komatsu, N.; Mitsui, G.; Hirota, M.; Hu, E. *Catalysis Today* **2009**, *148*, 341.

[57] Tsuneoka, H.; Teramura, K.; Shishido, T.; Tanaka, T. *Journal of Physical Chemistry C* **2010**, *114*, 8892.

[58] Teramura, K.; Okuoka, S.; Tsuneoka, H.; Shishido, T.; Tanaka, T. *Applied Catalysis B-Environmental* **2010**, *96*, 565.

[59] Wu, J. C. S.; Lin, H. M.; Lai, C. L. *Applied Catalysis a-General* **2005**, *296*, 194.

[60] Nguyen, T. V.; Wu, J. C. S.; Chiou, C. H. *Catalysis Communications* **2008**, *9*, 2073.

[61] Nguyen, T. V.; Wu, J. C. S. *Solar Energy Materials and Solar Cells* **2008**, *92*, 864.

[62] Pan, P. W.; Chen, Y. W. *Catalysis Communications* **2007**, *8*, 1546.

[63] Liu, Y. Y.; Huang, B. B.; Dai, Y.; Zhang, X. Y.; Qin, X. Y.; Jiang, M. H.; Whangbo, M. H. *Catalysis Communications* **2009**, *11*, 210.

[64] Jun, K. W.; Shen, W. J.; Rao, K. S. R.; Lee, K. W. *Applied Catalysis a-General* **1998**, *174*, 231.

[65] Solymosi, F.; Kliveyni, G. *Journal of Physical Chemistry* **1994**, 98, 8061.

[66] Bigg, T.; Judd, S. J. *Process Safety and Environmental Protection* **2001**, *79*, 297.

[67] Nam, S.; Tratnyek, P. G. *Water Research* **2000**, *34*, 1837.

[68] Chen, D.W.; Li, F.M.; Ray, A.K. *Alche Journal* **2000** *46*, 1034.

[69] Chen, D.W.; Li, F.M.; Ray, A.K. *Catalysis Today* **2001** *66*, 475.

[70] Dijkstra, M. F. J.; Michorius, A.; Buwalda, H.; Panneman, H. J.; Winkelman, J. G. M.; Beenackers, A. *Catalysis Today* **2001**, *66*, 487.

[71] Wang, R.; Hashimoto, K.; Fujishima, A.; Chikuni, M.; Kojima, E.; Kitamura, A.; Shimohigoshi, M.; Watanabe, T. *Advanced Materials* **1998**, *10*, 135.

[72] Tan, S. S.; Zou, L.; Hu, E. *Science and Technology of Advanced Materials* **2007**, *8*, 89.

[73] Danckwerts, P. V. *Chemical Engineering Science* **1953**, *2*, 1.

[74] Zwietering, T. N. *Chemical Engineering Science* **1959**, *11*, 1.

[75] Weinstei.H; Adler, R. J. *Chemical Engineering Science* **1967**, *22*, 65.

[76] Chauhan, S. P.; Adler, R. J.; Bell, J. P. *Chemical Engineering Science* **1972**, *27*, 585.

[77] Ren, M. M.; Valsaraj, K. *International Journal of Chemical Reactor Engineering* **2009**, *7*.

[78] Tan, S. S.; Zou, L.; Hu, E. *Catalysis Today* **2006**, *115*, 269.

[79] Indrakanti, V. P.; Kubicki, J. D.; Schobert, H. H. *Energy & Environmental Science* **2009**, *2*, 745.

[80] Sahibzada, M. *Chemical Engineering Research and Design* **2000**, *78*, 943.

[81] Rasko, J.; Solymosi, F. *Journal of Physical Chemistry* **1994**, *98*, 7147.

[82] Freund, H. J.; Roberts, M. W. *Surface Science Reports* **1996**, *25*, 227.

[83] Indrakanti, V. P.; Schobert, H. H.; Kubicki, J. D. *Energy & Fuels* **2009**, *23*, 5247.

[84] Solymosi, F.; Kiss, J.; Revesz, K. *Journal of Chemical Physics* **1991**, *94*, 8510.

[85] Uner, D.; Oymak, M. M. *Catalysis Today* in press

[86] Chinchen, G. C.; Denny, P. J.; Parker, D. G.; Spencer, M. S.; Whan, D. A. *Applied Catalysis* **1987**, *30*, 333.

[87] Sahibzada, M.; Metcalfe, I. S.; Chadwick, D. *Journal of Catalysis* **1998**, *174*, 111.

[88] Melian-Cabrera, I.; Granados, M. L.; Fierro, J. L. G. *Journal of Catalysis* **2002**, *210*, 285.

[89] Arakawa, H.; Dubois, J. L.; Sayama, K. *Energy Conversion and Management* **1992**, *33*, 521.

[90] Qi, G. X.; Zheng, X. M.; Fei, J. H.; Hou, Z. Y. *Catalysis Letters* **2001**, *72*, 191.

[91] Lee, K. H.; Lee, J. S. *Korean Journal of Chemical Engineering* **1995**, *12*, 460.

[92] Arena, F.; Italiano, G.; Barbera, K.; Bonura, G.; Spadaro, L.; Frusteri, F. *Catalysis Today* **2009**, *143*, 80.

[93] Fujita, S.; Moribe, S.; Kanamori, Y.; Kakudate, M.; Takezawa, N. *Applied Catalysis a-General* **2001**, *207*, 121.

[94] Muller, M.; Hermes, S.; Kaehler, K.; van den Berg, M. W. E.; Muhler, M.; Fischer, R. A. *Chemistry of Materials* **2008**, *20*, 4576.

[95] Vanden Bussche, K. M.; Froment, G. F. *Journal of Catalysis* **1996**, *161*, 1.

[96] Graaf, G. H.; Sijtsema, P. J. J. M.; Stamhuis, E. J.; Joosten, G. E. H. *Chemical Engineering Science* **1986**, *41*, 2883.

[97] Klier, K.; Chatikavanij, V.; Herman, R. G.; Simmons, G. W. *Journal of Catalysis* **1982**, *74*, 343.

[98] Ovesen, C.V., Clausen, B.S., Schiotz, C., Stoltze, P., Topsoe, H., Norskov, J.K, *Journal of Catalysis* **1997**, *168*, 133.

[99] Askgaard, T.S., Norskov, J.K., Ovesen, C.V., Stoltze, P, *Journal of Catalysis* **1995**, *156*, 229.

[100] Xia, X.; d'Alnoncourt, R. N.; Strunk, J.; Litvinov, S.; Muhler, M. *Applied Surface Science* **2007**, *253*, 5851.

[101] Shustorovich, E; Bell, A. T. *Surface Science* **1991**, *253*, 386.

[102] Dumesic, J. A.; Rudd, D. F.; Aparicio, L. M.; Rekoske, J. E.; Trevino, A. A. *The Microkinetics of Heterogeneous Catalysis;* American Chemical Society: Washington, 1993.

[103] Campbell, C.T.; Letter to the Editor, *Journal of Catalysis*, **2001**, *204*, 520.

[104] Majid, A.; Tunney, J.; Argue, S.; Kingston, D.; Post, M.; Margeson, J.; Gardner, G. J. *Journal of Sol- Gel Science and Technology* **2010**, *53*, 390.

[105] Ramirez, A. P.; Subramanian, M. A; Gardel, M.; Blumberg, G.; Li, D.; Vogt, T.; Shapiro, S. M. *Solid State Communications* **2000,** *115*, 217.

[106] Hisatomi, T.; Maeda, K.; Takanabe, K.; Kubota, J.; Domen, K. *Journal of Physical Chemistry C* **2009**, *113*, 21458.

[107] Suzuki, E.; Hayashi, Y.; Shimomura, Y.; Yoshida, S.; Usami, H.; Nakasa, A.; Fujimatsu, H. *Journal of Chemical Engineering of Japan* **2005**, *38*, 824.

[108] Choi, H. J.; Kang, M. *International Journal of Hydrogen Energy* **2007**, *32*, 3841.

[109] Kitano, M..; Takeuchi, M.; Matsuoka, M.; Thomas, J. M.; Anpo, M.; *Catalysis Today* **2007**, *120*, 133.

[110] Osman Karslıoğlu, *Photocatalytic and Photoelectrochemical Water Splitting over Ordered Titania Nanotube Arrays*, M.Sc. Thesis, Chemical Engineering Department, METU, Ankara, 2008.

APPENDIX A

REDOX COMPONENTS IN PHOTOSYNTHESIS

A.1 TYROSINE

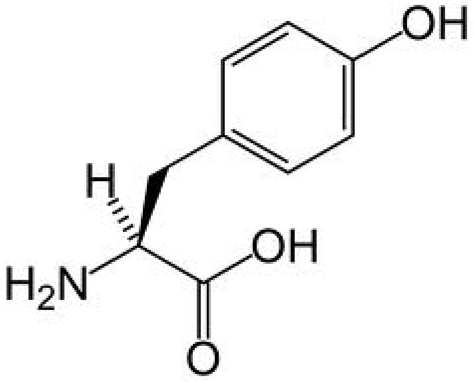

Figure A.1 Structural formula of tyrosine

A.2 PLASTOQUINONE

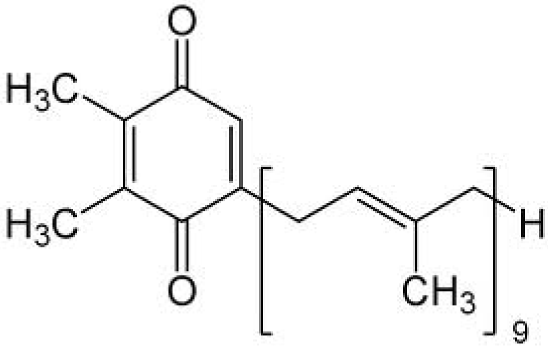

Figure A.2 Structural formula of plastoquinone

A.3 PLASTOCYANIN

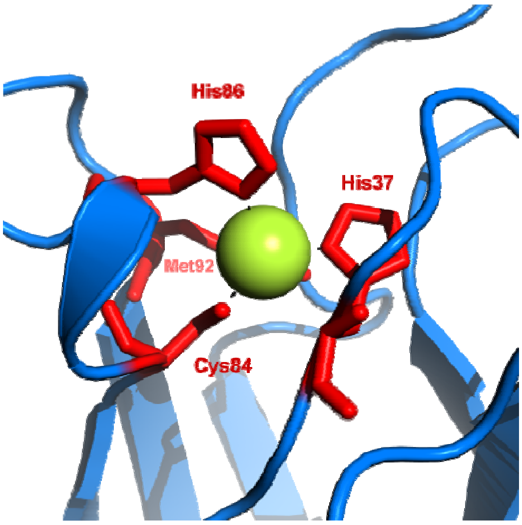

Figure A.3 Demonstration of copper site in plastocyanine with four amino acids bound to copper molecule

A.4 FERRODOXIN

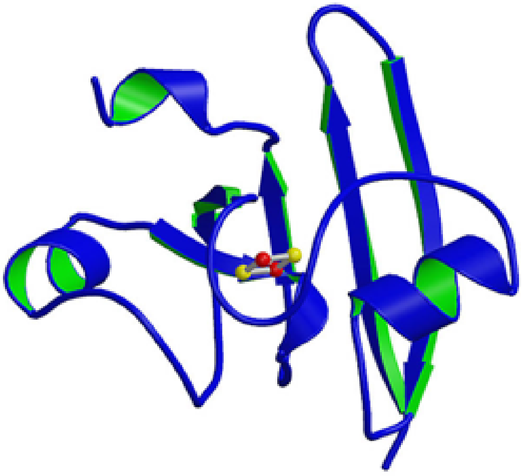

Figure A.4 Demonstration of Fe_2S_2 ferrodoxin

A.5 CHLOROPHYLL A AND CHLOROPHYLL B

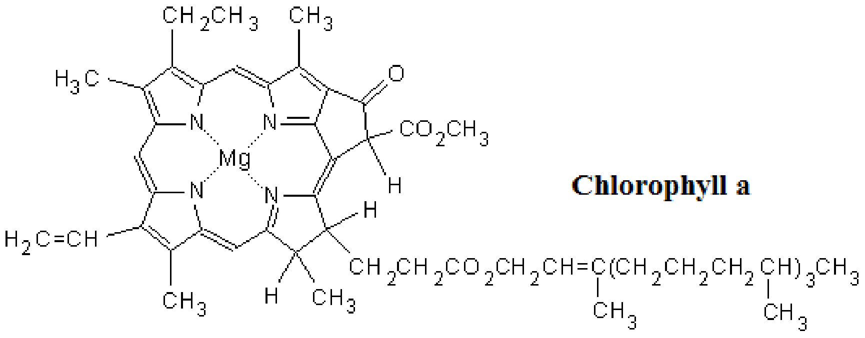

Chlorophyll a

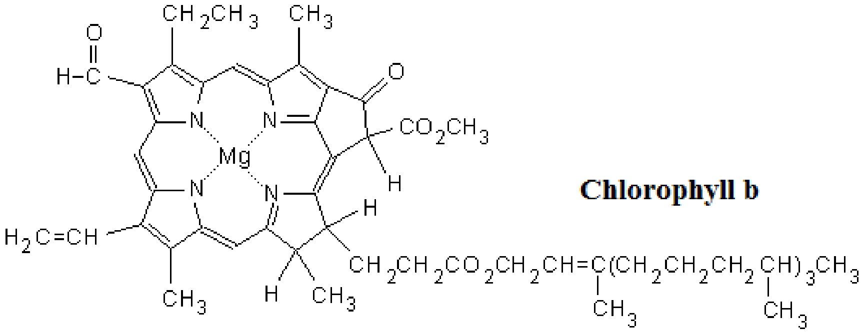

Chlorophyll b

Figure A.5 Structural formulas of Chloropyhll a and Chlorophyl b

APPENDIX B

PHOTOCATALYTIC TEST RESULT CALCULATIONS

B.1 MASS TRANSFER LIMITATION EXPERIMENTS

In the mass transfer limitations, pressure and temperature of the system were recorded for each sample withdrawn. The calibration curve for hydrogen in GC/TCD is given in Equation (B.1).

$$\% \text{ concentration of } H_2 = 5.8*10^{-4} * H_2 \text{ peak area in GC} \qquad \text{(B.1)}$$

Table B.1 Raw data obtained from stirring rate experiments, a. 900 rpm, b. 350 rpm

a. 900 rpm						
Time (h)	**Peak Area (H_2)**	**%conc H_2**	**Pressure (Pa)**	**T (K)**	**Micromole of H_2**	**Micromole of H_2/gcat**
0	0	0	101521.2	298	0	0
0.25	1051.3	0.61	103188.9	302	26.813	107.25
0.5	3259.4	1.89	104660.4	306	83.214	332.86
0.75	5790.3	3.36	105837.6	308	148.52	594.09
1	7975.9	4.63	105935.7	308	204.77	819.09
1.25	10596.3	6.15	106328.1	309	272.17	1088.70
1.5	12845.3	7.45	106818.6	311	329.33	1317.32
1.75	14893.6	8.64	107897.7	313	383.23	1532.95
2	17427.1	10.11	108584.4	313	451.28	1805.13

Table B.1 (Continued)

b. 350 rpm						
Time (h)	**Peak Area (H_2)**	**%conc H_2**	**Pressure (Pa)**	**T (K)**	**Micromole of H_2**	**Micromole of H_2/gcat**
0	0	0.00	101619.3	296	0	0.00
0.25	294.6	0.17	102698.4	302	7.48	29.91
0.5	1070.9	0.62	103483.2	307	26.95	107.78
0.75	2195.6	1.27	103581.3	310	54.76	219.05
1	4654.1	2.70	104856.6	312	116.76	467.02
1.25	6977.2	4.05	106033.8	313	176.43	705.74
1.5	9685.1	5.62	107799.6	315	247.41	989.63
1.75	11414.3	6.62	108878.7	315	294.50	1177.99
2	13486.8	7.82	109467.3	315	349.85	1399.41

During the calculations, gas volume of the reactor is taken constant at 104 ml. Micromoles of hydrogen is calculated from ideal gas law with found % concentrations in the gas volume.

Table B.2 Raw data for effect of gas hold-up time experiments with 0.5 wt % Pt/TiO$_2$, a. 62.5 ml, b. 125 ml, c. 187.5 ml, d. 250 ml

a. 62.5 ml

Time (h)	Peak Area (H_2)	%conc H_2	Pressure (Pa)	T (K)	Micromole of H_2	Micromole of H_2/gcat
0	0	0.00	101521.2	297	0.00	0.00
0.25	484.4	0.28	103973.7	302	34.26	548.21
0.5	1018.6	0.59	105150.9	308	71.44	1143.11
0.75	1471.6	0.85	106131.9	310	103.51	1656.14
1	1798.6	1.04	106916.7	310	127.44	2039.11
1.25	2228.6	1.29	107211	312	157.33	2517.33
1.5	2762.4	1.60	107603.4	313	195.11	3121.70
1.75	3062.6	1.78	107897.7	313	216.90	3470.41
2	4095.2	2.38	108093.9	313	290.56	4648.95

b. 125 ml

Time (h)	Peak Area (H_2)	%conc H_2	Pressure (Pa)	T (K)	Micromole of H_2	Micromole of H_2/gcat
0	0	0.00	101619.3	297	0.00	0.00
0.25	406.2	0.24	102796.5	302	22.38	179.02
0.5	998	0.58	104366.1	305	55.27	442.17
0.75	1948.8	1.13	105837.6	308	108.38	867.07
1	2527.6	1.47	106720.5	310	140.83	1126.65
1.25	4158.7	2.41	107995.8	312	232.98	1863.83
1.5	5088	2.95	109467.3	313	288.00	2304.00
1.75	6195.2	3.59	109859.7	313	351.93	2815.43
2	7174.5	4.16	111135	313	412.29	3298.33

Table B.2 (Continued)

c. 187.5 ml						
Time (h)	**Peak Area (H_2)**	**%conc H_2**	**Pressure (Pa)**	**T (K)**	**Micromole of H_2**	**Micromole of H_2/gcat**
0	0	0.00	101521.2	298	0.00	0.00
0.25	1026.7	0.60	102992.7	302	41.40	220.82
0.5	2170.8	1.26	104464.2	306	87.63	467.36
0.75	3702.1	2.15	104954.7	309	148.69	793.01
1	5169.4	3.00	105739.5	311	207.83	1108.42
1.25	6241.4	3.62	106622.4	312	252.21	1345.12
1.5	7516.7	4.36	107211	313	304.45	1623.71
1.75	8621.2	5.00	108388.2	313	353.01	1882.75
2	10045.8	5.83	109173	313	414.33	2209.74
d. 250 ml						
Time (h)	**Peak Area (H_2)**	**%conc H_2**	**Pressure (Pa)**	**T (K)**	**Micromole of H_2**	**Micromole of H_2/gcat**
0	0	0	101521.2	298	0	0
0.25	1051.3	0.61	103188.9	302	26.813	107.25
0.5	3259.4	1.89	104660.4	306	83.214	332.86
0.75	5790.3	3.36	105837.6	308	148.52	594.09
1	7975.9	4.63	105935.7	308	204.77	819.09
1.25	10596.3	6.15	106328.1	309	272.17	1088.70
1.5	12845.3	7.45	106818.6	311	329.33	1317.32
1.75	14893.6	8.64	107897.7	313	383.23	1532.95
2	17427.1	10.11	108584.4	313	451.28	1805.13

Table B.3 Raw data for effect of temperature experiments with 1 wt % Pt/TiO_2, a. 32 °C, b. 65 °C, c. 77 °C, d. 85 °C

a. 32 ° C

Time (h)	**Peak Area (H_2)**	**%conc H_2**	**Pressure (Pa)**	**T (K)**	**Micromole of H_2**	**Micromole of H_2/gcat**
0	0	0.00	101325	296	0	0.00
0.25	1342.7	0.88	101717.4	298	21.59	86.35
0.5	4457.4	2.91	102109.8	300	71.46	285.85
0.75	9079.4	5.93	102306	300	145.85	583.38
1	12231.7	7.98	102502.2	301	196.20	784.82
1.25	16127.1	10.53	103483.2	302	260.30	1041.20
1.5	18882.4	12.32	104954.7	304	307.07	1228.29
1.75	22383	14.61	105150.9	304	364.68	1458.72
2	25283.6	16.50	105935.7	304	415.01	1660.06

b. 65 ° C

Time (h)	**Peak Area (H_2)**	**%conc H_2**	**Pressure (Pa)**	**T (K)**	**Micromole of H_2**	**Micromole of H_2/gcat**
0	0	0.00	101325	338	0.00	0.00
0.25	1444.5	0.84	103581.3	338	32.12	128.47
0.5	4666	2.71	105543.3	338	105.71	422.83
0.75	7855.7	4.56	107309.1	338	180.95	723.80
1	11967.1	6.94	108878.7	338	279.68	1118.73
1.25	14599.7	8.47	110546.4	338	346.44	1385.74
1.5	18641.7	10.81	112017.9	338	448.24	1792.95
1.75	21499.3	12.47	113195.1	338	522.38	2089.52
2	26397.8	15.31	114470.4	338	648.63	2594.51

Table B.3 (Continued)

c. 77 ° C

Time (h)	Peak Area (H_2)	%conc H_2	Pressure (Pa)	T (K)	Micromole of H_2	Micromole of H_2/gcat
0	0	0.00	101423.1	350	0.00	0.00
0.25	1084.8	0.63	102992.7	350	23.16	92.64
0.5	4732.2	2.74	104169.9	350	102.19	408.74
0.75	9541.7	5.53	105935.7	350	209.53	838.13
1	14651.8	8.50	107505.3	350	326.52	1306.06
1.25	18543.1	10.75	109467.3	350	420.78	1683.10
1.5	24047.4	13.95	110644.5	350	551.55	2206.18
1.75	27837.3	16.15	112116	350	646.96	2587.84
2	34792.5	20.18	113587.5	350	819.22	3276.87

d. 85 ° C

Time (h)	Peak Area (H_2)	%conc H_2	Pressure (Pa)	T (K)	Micromole of H_2	Micromole of H_2/gcat
0	0	0.00	103188.9	358	0.00	0.00
0.25	767.5	0.45	104758.5	358	16.29	65.18
0.5	5367.2	3.11	106524.3	358	115.87	463.47
0.75	11721	6.80	107995.8	358	256.53	1026.12
1	18149.3	10.53	109369.2	358	402.28	1609.10
1.25	24531.5	14.23	110448.3	358	549.10	2196.40
1.5	32467.8	18.83	112704.6	358	741.59	2966.35
1.75	39641.7	22.99	113685.6	358	913.33	3653.31
2	49864	28.92	114568.5	358	1157.77	4631.06

Table B.4 Raw data for effect of temperature experiments with 1 wt % Cu/TiO_2, a. 44 °C, b. 75 °C

a. 44 ° C						
Time (h)	**Peak Area (H_2)**	**%conc H_2**	**Pressure (Pa)**	**T (K)**	**Micromole of H_2**	**Micromole of H_2/gcat**
0	0	0.00	101423.1	300	0.00	0.00
0.25	52.6	0.03	102796.5	305	1.33	5.31
0.5	496	0.30	103777.5	310	12.44	49.74
0.75	1239.5	0.74	104758.5	314	30.97	123.88
1	2052.2	1.23	106033.8	316	51.57	206.29
1.25	2708.6	1.62	107014.8	316	68.70	274.79
1.5	4142.6	2.48	107505.3	317	105.21	420.86
1.75	5785.3	3.46	108192	317	147.87	591.50
2	6976.5	4.18	108780.6	317	179.29	717.17

b. 75 ° C						
Time (h)	**Peak Area (H_2)**	**%conc H_2**	**Pressure (Pa)**	**T (K)**	**Micromole of H_2**	**Micromole of H_2/gcat**
0	0	0.00	101325	348	0.00	0.00
0.25	81.3	0.05	103287	348	1.81	7.23
0.5	1021.4	0.61	106524.3	348	23.42	93.66
0.75	3297	1.97	108486.3	348	76.97	307.90
1	5202.8	3.11	109467.3	348	122.57	490.27
1.25	6417.6	3.84	110448.3	348	152.54	610.16
1.5	8285.9	4.96	111919.8	348	199.57	798.29
1.75	10649	6.38	117315.3	348	268.85	1075.42
2	13182.8	7.89	118590.6	348	336.44	1345.77

B.2 PHOTOCATALYTIC CO_2 REDUCTION EXPERIMENTS

In CO_2 reduction experiments, the moles of methanol in 300 ml water were calculated from the raw % volume concentration data obtained from GC FID analysis. The calibration curve found for methanol/water mixture is given in Equation (B.2).

% concentration of MeOH= $3.99*10^{-8}*$ peak area of MeOH (B.2)

During the calculations of micromoles of methanol in 300 ml water, density and molecular mass of methanol is taken as 0.7918 g/cm^3 and 32.04 g/mole respectively.

Table B.5 Raw data obtained from photocatalytic CO_2 reduction experiment performed with first set of catalysts a. 1 wt % Cu/ TiO_2 (Degussa P25), b. 2 wt % Cu/ TiO_2 (Degussa P25), c. 3 wt % Cu/ TiO_2 (Degussa P25)

a. 1 wt % Cu/TiO_2 (Degussa P25)					
Time (h)	**Peak Area of MeOH**	**%conc MeOH in liquid**	**Volume of MeOH (ml) in 300 ml water**	**Micromole of MeOH**	**Micromole of MeOH/gcat**
0	0	0	0	0.00	0.00
1	0	0	0	0.00	0.00
2	618.6	$2.47*10^{-5}$	$7.40*10^{-5}$	1.83	6.10
3	1125.2	$4.49*10^{-5}$	$1.35*10^{-4}$	3.33	11.09
4	1334	$5.32*10^{-5}$	$1.60*10^{-4}$	3.95	13.15
5	1608	$6.42*10^{-5}$	$1.92*10^{-4}$	4.76	15.86
6	1426.2	$5.69*10^{-5}$	$1.71*10^{-4}$	4.22	14.06
7	838	$3.34*10^{-5}$	$1.00*10^{-4}$	2.48	8.26

Table B.5 (Continued)

b. 2 wt % Cu/TiO$_2$ (Degussa P25)

Time (h)	Peak Area of MeOH	%conc MeOH in liquid	Volume of MeOH (ml) in 300 ml water	Micromole of MeOH	Micromole of MeOH/gcat
0	0	0	0	0.00	0.00
1	0	0	0	0.00	0.00
2	0	0	0	0.00	0.00
3	130	$5.19*10^{-6}$	$1.56*10^{-5}$	0.38	1.28
4	258	$1.03*10^{-5}$	$3.09*10^{-5}$	0.76	2.54
5	773	$3.08*10^{-5}$	$9.25*10^{-5}$	2.29	7.62
6	757.8	$3.02*10^{-5}$	$9.07*10^{-5}$	2.24	7.47
7	435	$1.74*10^{-5}$	$5.21*10^{-5}$	1.29	4.29

c. 3 wt % Cu/TiO$_2$ (Degussa P25)

Time (h)	Peak Area of MeOH	%conc MeOH in liquid	Volume of MeOH (ml) in 300 ml water	Micromole of MeOH	Micromole of MeOH/gcat
0	0	0	0	0	0.00
1	229.2	$9.1*10^{-6}$	$2.74*10^{-5}$	0.68	2.26
2	1660.6	$6.6*10^{-5}$	$1.99*10^{-4}$	4.91	16.37
3	2283.5	$9.1*10^{-5}$	$2.73*10^{-4}$	6.75	22.52
4	1668	$6.7*10^{-5}$	$2.00*10^{-4}$	4.93	16.45
5	2652.2	$1.1*10^{-4}$	$3.17*10^{-4}$	7.85	26.15
6	1807.3	$7.2*10^{-5}$	$2.16*10^{-4}$	5.35	17.82
7	1815.7	$7.2*10^{-5}$	$2.17*10^{-4}$	5.37	17.90

Table B.6 Raw data obtained from photocatalytic CO_2 reduction experiment performed with second set of catalysts a. 1 wt % Cu/ TiO_2 b. 2 wt % Cu/ TiO_2

a. 1 wt % Cu/TiO_2					
Time (h)	**Peak Area of MeOH**	**%conc MeOH in liquid**	**Volume of MeOH (ml) in 300 ml water**	**Micromole of MeOH**	**Micromole of MeOH/gcat**
0	0	0	0	0.00	0.00
1	0	0	0	0	0
2	112.1	$3.92*10^{-6}$	$1.18*10^{-5}$	0.29	0.97
3	35	$1.23*10^{-6}$	$3.68*10^{-6}$	0.09	0.30
4	0	0	0	0	0
5	0	0	0	0	0
6	0	0	0	0	0
b. 2 wt % Cu/TiO_2					
Time (h)	**Peak Area of MeOH**	**%conc MeOH in liquid**	**Volume of MeOH (ml) in 300 ml water**	**Micromole of MeOH**	**Micromole of MeOH/gcat**
0	0	0	0	0	0
1	0	0	0	0	0
2	772.38	$3.08*10^{-5}$	$9.24*10^{-5}$	2.28	7.62
3	48.28	$1.92*10^{-6}$	$5.78*10^{-6}$	0.14	0.48
4	0	0	0	0	0
5	0	0	0	0	0
6	0	0	0	0	0

Table B.7 Raw data obtained from photocatalytic CO_2 reduction experiment performed with fourth set of catalyst (3 wt % Cu/ TiO_2)

Time (h)	**Peak Area of MeOH**	**%conc MeOH in liquid**	**Volume of MeOH (ml) in 300 ml water**	**Micromole of MeOH**	**Micromole of MeOH/gcat**
0	0	0	0	0	0
1	0	0	0	0	0
2	0	0	0	0	0
3	2376.2	$9.48*10^{-5}$	$2.84*10^{-4}$	7.03	23.43
4	1335.4	$5.33*10^{-5}$	$1.60*10^{-4}$	3.95	13.17
5	2799.1	$1.12*10^{-4}$	$3.35*10^{-4}$	8.28	27.60
6	1704.1	$6.80*10^{-5}$	$2.04*10^{-4}$	5.04	16.80
7	339.1	$1.35*10^{-5}$	$4.06*10^{-5}$	1.00	3.34

APPENDIX C

XPS MEASUREMENTS OF Cu/ TiO_2 CATALYSTS

XPS measurements were performed for 1, 2 and 3 wt % Cu/ Degussa P25 (First Set), 2 wt % Cu/ TiO_2 (Second Set), 1wt % Cu/ TiO_2 (Third Set) and 3 wt % Cu/ TiO_2 (Fourth Set) catalysts in order to reveal probable oxidation states of copper on titanium dioxide and also to be able to comment on surface concentration of the catalysts.

The element molar ratio of copper to titanium calculated from preparation weight ratios and from XPS measurements can be seen in Table B.1.

Table C.1 The element molar ratio of catalysts found by XPS

Catalysts	**Cu/Ti**	
	Bulk	**XPS**
1 wt % Cu/ Degussa P25	0.013	0
2 wt % Cu/ Degussa P25	0.025	0.014
3 wt % Cu/ Degussa P25	0.038	0.440
2 wt % Cu/ TiO_2 (Second Set)	0.025	1.161
1 wt % Cu/ TiO_2 (Third Set)	0.013	0.504
3 wt % Cu/ TiO_2 (Fourth Set)	0.038	0.652

Observed higher Cu/Ti ratios from XPS measurements indicate that most of the copper elements were located on TiO_2 surface. Very high Cu/ Ti ratios like

1.161 for 2 wt % Cu/ TiO_2 catalyst suggest excess copper coverage of TiO_2 surface which could result in inefficient light activation of the semiconductor.

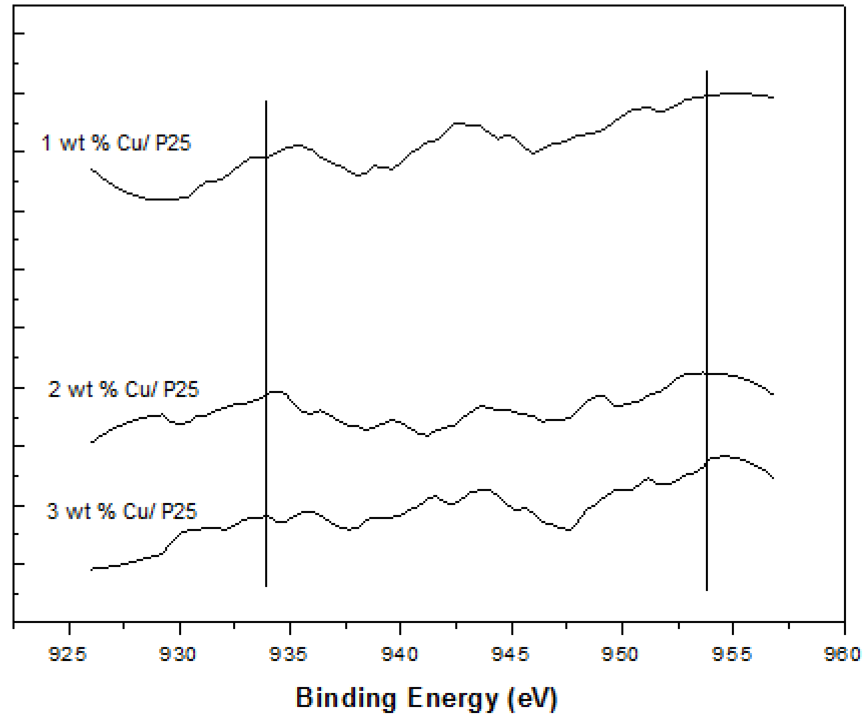

Figure C.1 XPS spectra of Cu/ Degussa P25 catalysts prepared by incipient wetness method

Figure C.1 shows XPS spectra of 1, 2 and 3 wt % Cu/ Degussa P25 catalysts prepared with incipient wetness method. The binding energies of Cu $2p_{3/2}$ and Cu $2p_{1/2}$, 933.8 and 953.6 eV respectively reveal the presence of CuO species on catalyst surfaces.